



IAF
International
Aeronautical Federation

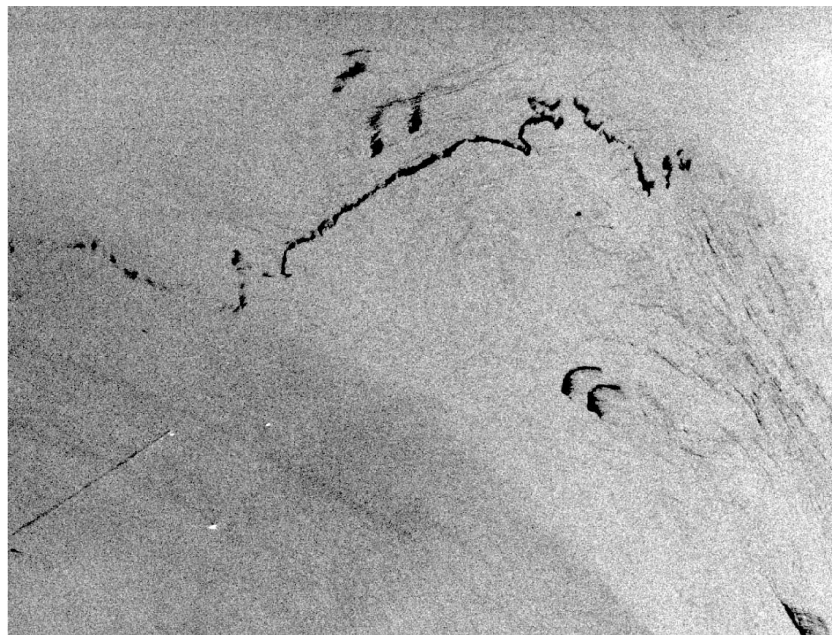
OSCSAR

Marine Oil Spill Control: SAR Monitoring and Model Prediction

Final Report

Contribution by

S. Sandven, V. N. Kudryavtsev, D. Akimov, T. Hamre, L. Bobylev,
V. Lavrenov, V. Stanovoy, S. A. Ermakov, A. Feoktissoy,
P.V. Lyushvin, V. V. Malinovsky, A. V. Agarkov, S. Matvienko



*Example of ERS SAR image showing several oil slicks in
the Black Sea. Copyright ESA 2004*

**IAF-BEAR project
GMES Networking with Russian and Ukraine 2004 – 2005**

Coordinated by

*Nansen Environmental and Remote Sensing Center
20 March 2006*

Nansen Environmental and Remote Sensing Center Technical Report no. 271

			
<p>Nansen Environmental and Remote Sensing Center (NERSC) Thormøhlensgt. 47, N 5006 Bergen, Norway Tel: +47 55205800, Fax: +47 55205801 http://www.nersc.no Stein Sandven (coordinator) e-mail: stein@nersc.no</p>	<p>Nansen International Environmental and Remote Sensing Center (NIERSC) Bolshaya Monetnaya str. 26/28 197101 St. Petersburg, Russia Tel. + 7 (812) 234 3865 Fax + 7 (812) 234 3865 http://www.niersc.spb.ru/ Vladimir N. Kudryavtsev e-mail: Vladimir.Kudryavtsev@niersc.spb.ru</p>	<p>Arctic and Antarctic Research Institute (AARI) Av. Bering 38 199397 St. Petersburg, Russia Tel. + 7 (812) 352 3604 Fax. + 7 (812) 352 2688 http://www.aari.nw.ru Igor. V. Lavrenov e-mail: lavren@aari.nw.ru</p>	<p>Institute of Applied Physics Russian Academy of Sciences (IAP) Uljanova str. 46 603950 Nizhny Novgorod, Russia Tel. + 7 (8312) 164935 Fax: + 7 (8312) 365976 Stanislav A. Ermakov e-mail: stas@hydro.appl.sci-nnov.ru</p>
			
<p>Institutes Français de Recherche pour l'Exploitation de la mer (IFREMER) Technopole Brest Iriose BP 70 29280 Plouzane, France Tel. + 33 2 98224312 Fax: + 33 2 98224533 http://www.ifremer.fr Bertrand Chapron, E-mail: Bertrand.Chapron@ifremer.fr</p>	<p>Marine Hydrophysical Institute of the Ukrainian National Academy of Sciences (MHI) Kapitanskaya str. 2 99011 Sevastopol, Ukraine Tel. + 38 0692 545065 Fax: + 38 0692 554253 Vladimir V. Malinovsky e-mail: dsv@alpha.mhi.iuf.net</p>	<p>State Design Office "Yuzhnoye" (DOYu) Krivorozhskaya Str., 3 49008 Dnepropetrovsk, Ukraine Tel. + 38 0562 420022 Fax: + 38 0562 7700125 Anatoly V. Agarkov E-mail: info@yuzhnoye.com</p>	<p>Research Center for Earth Operative Monitoring (NTs OMZ) Dekabristov str. 51, building 25 127490 Moscow, Russia Tel. + 7 (095) 105 0413 Fax: + 7 (095) 404 7745 Alexey Feoktisov E-mail: f.eoktistov@ntsomz.ru</p>

<p>TITLE: Marine oil spill control: SAR monitoring and model prediction (OSCSAR)</p>	<p>REPORT IDENTIFICATION OSCSAR Final report NERSC Technical Report no. 271</p>
<p>CLIENT IAF: International Aeronautical Federation http://www.iafastro.com</p>	<p>CONTRACT Contract Number:</p>
<p>CLIENT REFERENCE Goneri LeCozannet E-mail: Goneri.Le_Cozannet@esa.int</p>	<p>AVAILABILITY Open</p>
<p>INVESTIGATORS S. Sandven, T. Hamre (NERSC) V. N. Kudryavtsev, D. Akimov, L. Bobilev (NIERSC) I. V. Lavrenov, V. Stanovoy (AARI) S. A. Ermakov (IAP), A. Feoktisov P.V. Lyushvin, (NTs OMZ) V. V. Malinovsky (MHI), A., V. Agarkov, S. Matvienko (DOYu)</p>	<p>AUTHORISATION Bergen, 20 March 2006 Stein Sandven</p>

Contents

PROJECT SUMMARY	3
PART A: DETAILED PROJECTS RESULTS	7
TASK 1: WAVE MODELING INCLUDING EFFECT OF DAMPING BY OIL FILMS.....	7
1.1 METHODOLOGY	7
1.2 RESULTS	7
1.3 RETRIEVAL OF FILM CHARACTERISTICS	10
<i>The surface tension coefficient.....</i>	<i>10</i>
<i>The elasticity of CO/OD films</i>	<i>11</i>
1.4 SPECTRUM CONTRAST IN CO/OD SPILLS	14
1.5 CONCLUSIONS.....	15
TASK 2: RADAR SCATTERING MODEL.....	16
2.1 MODEL APPROACH	16
2.2 VALIDATION OF THE BACKGROUND MODEL	20
2.3. VALIDATION OF THE MODEL AGAINST AVAILABLE PUBLISHED DATA	22
2.4. SURFACTANT FILMS IN PRESENCE ON SURFACE CURRENTS	26
2.5. C-BAND RADAR SENSITIVITY STUDY	27
2.6 CONCLUSIONS.....	29
TASK 3.1: SATELLITE IMAGE ANALYSIS IN CASPIAN AND KARA SEAS	30
3.1.1 <i>Description of work performed.....</i>	<i>30</i>
3.1.2 <i>Problems related to the use of remote sensing images</i>	<i>34</i>
3.1.3 <i>Main achievements</i>	<i>35</i>
TASK 3.2 SATELLTE IMAGE ANALYSIS FOR THE BLACK SEA.....	41
3.2.1 <i>Introduction to oil spill monitoring in the Black Sea</i>	<i>41</i>
3.2.2 <i>Compilation data sets for the Black Sea</i>	<i>42</i>
3.2.3 <i>Analysis of SAR images in the Black Sea</i>	<i>45</i>
3.2.4 <i>Assessment of oil spill detection in the Black Sea</i>	<i>50</i>
3.2.5 <i>Features of radar backscattering from sea surface covered with film.....</i>	<i>52</i>
3.2.6 <i>Results of the Black Sea studies.....</i>	<i>53</i>
3.2.7 <i>Discussion</i>	<i>56</i>
3.3 DEDICATED ASAR FIELD EXPERIMENT IN THE BLACK SEA	57
3.3.1 <i>Introduction and objectives.....</i>	<i>57</i>
3.3.2 <i>Meteorological and wave measurements</i>	<i>59</i>
3.3.3 <i>Measurements of wind fluctuations</i>	<i>62</i>
3.3.4 <i>Autonomous buoy measurements.....</i>	<i>64</i>
3.3.5 <i>ASAR ENVISAT images.....</i>	<i>64</i>
3.3.6 <i>Preliminary conclusions from the field experiment.....</i>	<i>70</i>
TASK 4: OIL DRIFT MODELING IN COLD ICE-COVERED WATERS	70
TASK 5: DISSEMINATION AND PROMOTION	77
<i>List of publications, reports and abstracts where OSCSAR is acknowledged.....</i>	<i>80</i>
TASK 6: NETWORKING AND COORDINATION WITH OTHER GMES PROJECTS	83
ACKNOWLEDGEMENT	83
REFERENCES.....	84
PART B: FINANCIAL REPORT	85

Project summary

Objective

The overall objective has been to develop and demonstrate marine oil spill detection and prediction systems based on satellite Synthetic Aperture Radar (SAR) and other space data in combination with models for monitoring and assessment of environmental stress in Russian and Ukrainian seas.

Tasks

The project has been implemented through the following tasks:

- **TASK 1: Wave modeling and studies of wave damping by oil films.** The physical properties of crude oil and oil derivatives (CO/OD) films have been studied in laboratory experiments in order to develop an improved model of short wind wave damping under various oil film conditions.
- **TASK 2: Radar scattering modeling.** An improved model of radar scattering from the sea surface covered by oil and biogenic films has been developed. This model is used as input to an advanced algorithm of SAR/RAR detection of oil spills and their properties. The radar scattering model has been compared with radar experiment observations.
- **TASK 3: Satellite image analysis.** Spaceborne SAR and RAR images have been collected and analyzed for the the Black Sea the Caspian Sea and the Kara Sea. A specific field experiment was conducted in the Black Sea for validation of ASAR data in an area of experimental oil spill. The statistics of oil spills and their visibility/detectability in SAR images under wind conditions has been studied based on archived SAR data in the Black Sea.
- **TASK 4: Oil drift modeling.** An oil spill drift model for cold waters in the Northern Sea Route has been developed and tested. This model can be used to forecast the drift of an oil spill under different wind, wave, current and ice conditions.
- **TASK 5: Dissemination and promotion.** The results of the satellite observation and modeling work developed in Task 1 – 4 have been disseminated via publication, reports and presentations at conferences.
- **TASK 6: Networking.** The research and development work in OSCSAR has been used to establish a network between institutions in Russia, Ukraine and western European countries.

Main results

Institute of Applied Physics (IAF)

The impact of different oil films on gravity-capillary waves (GCW) has been studied in laboratory experiments using a method developed at the Institute of Applied Physics. The method has previously been used in modelling “biogenic” slicks on the sea surface. The experiments were used to study how the surface/interfacial tension coefficient depends on different crude oil/oil derivatives films. Furthermore, the relative damping coefficient has been determined for different thickness for oil, diesel fuel and kerosene films for temperatures between 1°C and 24°C. The damping coefficient is shown to increase weakly with growing film thickness from about 0.01mm to 1mm. The relative damping coefficient is nearly independent of water temperature. Furthermore, the experiments show that the coefficient is 1.5-2 times larger for crude oil films than for diesel fuel films.

The elasticity of CO/OD films has been determined by fitting the experimental data to a theory of wave damping by viscous films. Empirical relations between surface tension and thickness were derived. When the surface elasticity was determined, the interfacial tension and elasticity were neglected for films with thickness less than 0.3 mm. The surface elasticities for thin crude oil and

diesel fuel films were estimated to be about 3-4 mN/m. The CO/OD viscosity, normalized by water viscosity was measured to about 20 for crude oil, 8 for diesel fuel, and 1/3 for kerosene.

The retrieved values of the film parameters were used to estimate the damping degree (contrast) using a local balance model. The results of our field experiments similar studies by radar/optical probing of oil and organic (biogenic) films, although the model is very sensitive to the wind velocity.

Nansen International Environmental and Remote Sensing Center (NIERSC)

A model of short wind wave spectrum and radiowave scattering from the sea surface covered by natural or artificial films has proposed. This model extends recently developed semi-empirical model of the normalized radar cross-section (NRCS) and radar imaging model (Kudryavtsev et al. 2003; Kudryavtsev et al. 2005) by means of modification of viscous dissipation due to accounting for the physical/chemical properties of the sea surface films. These properties may be known from either a model (e.g. Levich, 1962,- monomolecular films; Jenkins and Jakobs, 1997- surface films of a finite thickness) or experiments (e.g. experiments by IAP Team, OSCSAR project). Important new element of the spectrum model is that it takes into account non-linear energy transfer from longer waves to shorter one. This mechanism explains important observed feature of surface slicks, - non-vanishing of wave spectral density inside the slick. Wave models which normally used for such kind study, are based on a local in k-space energy balance that presumes vanishing of the wave spectral density if viscous dissipation exceeds the wind energy input.

Wave spectrum (affected by a surface film) defines any statistical characteristics of the sea surface needed to calculate the NRCS. A composite scattering model supplied with scattering from breaking waves is adopted in the Project study. The NRCS model was extensively verified on C-band dual polarization radar measurements obtained by CETP (France) in the field aircraft experiments. Developed model was further verified against lab and well controlled field experiments on radar scattering from the surface covered by artificial films (Gade et al. 1998a; Gade et al. 1998b; IAP Team lab and field experiments). Model simulation showed that the NRCS model is consistent with experimental data on quantitative level, and can be further used to study radar scattering properties of the oil spills.

A sensitivity model study of effect of surface films on radar scattering for geometry of observations typical for operating ENVISAT ASAR was performed. It was shown, in particular, that at small incidence angles (< 15 deg.) radar scattering does not "feel" the films. The reason is that the specular reflections responsible for most of the radar return are formed by relatively large surface waves which are not affected by the films. At moderate incidence (where Bragg scattering is the dominating mechanism), radar sensitivity enhances with increasing incidence angle. Suppression of Bragg waves by the films results in increasing contrasts of polarization ratio (ratio of VV to HH NRCS). At high wind speed radar contrasts are significantly reduced, that is explained by increased role of wind forcing in respect to the film damping.

Developed model approach (Radar Imaging Model, RIModel) allows to map radar signatures of surface contaminations redistributed by surface current of arbitrary origin. Surfactants are accumulated in the convergent zones, therefore frequently observed linear radar signatures are their tracers. RIModel also provides an effective tool to study discriminative radar features of surface films and their look-alikes. However this problem is out of the scope of the project.

Research Center for Earth Operative Monitoring (NTsOMZ)

Data from satellites obtained at NTsOMZ (AVHRR/NOAA, SLR, SAR/ERS-2, ASAR/ENVISAT, MERIS/ENVISAT) have been analyzed to identify potential oil slicks and other surface phenomena in the Caspian Sea and the Kara Sea. An expert appraisal method in a GIS environment has been used as basis for oil spill identification. The decision on a probable slick has been made by an expert interpreter. The main characteristics for determination of a probable slicks has been shape, size, texture, boundary definition, and brightness properties of the object

identified in the image. Available data on surface current, winds, and probable pollution sources have been used in the analysis. The results showed that the synergetic analysis of SAR and optical/IR images is the most efficient method for finding surface slick features. The analysis of available data shows that extremely adverse weather and cloud conditions were a major obstacle to use of optical data in the Kara Sea. Besides, the complicated interactions between tidal current, wind and bathymetry generated many natural slicks which made it difficult for an expert interpreter to decide if a slick could be a man-made oil spill.

Software for marine oil pollution identification in SAR images is under development. A training data set for a thematic class of natural oil slicks was generated. To generate training set for man-made slicks data from the Black Sea and the Caspian Sea should be used, because oil pollution is more easy to detect in these regions. The algorithms are based on analysis of two-dimensional scattering plots, with emphasis on analysis of slick boundary area. The procedures under development may function when a limited volume of training data is used.

Marine Hydrophysical Institute (MHI)

Oil spill detection in the Black Sea was based on SAR images, meteorological data and sea surface temperature from NOAA AVHRR images. The spatial distribution of oil spills was estimated using pre-selected SAR images with slick signatures. A significant accumulation of slicks was found along the sailing route between Bosphorus and Novorossiisk. A second accumulation area was north of Bosphorus coinciding with ship routes. Two other areas of concentrated slicks were the north-eastern part of the Novorossiisk coast and in the western part close to oil platform and ports. Six cases of spills from ship were identified in the SAR images.

In September 2005 a field experiment was carried out on the south coast of Crimea to study oil spill signature in SAR images. ESA provided five ASAR Alternating Polarisation scenes in the study area where an offshore platform was used to perform atmospheric boundary layer and sea surface measurements. The experiment was carried out under moderate and weak wind conditions. The results showed that the radar contrast between the observed slicks and clean water was higher at vertical polarization than at horizontal polarization. The modulation of radar backscattering by long wind waves is about 3 times higher at vertical and 1.5-2 times higher at horizontal polarization for the slicks compared to clean water. The results will be used to develop and improve models to classify slicks and oil spills in SAR images. The field experiment was also supported by the National Space Agency of Ukraine as background for the development of a Ukrainian space programme for monitoring ocean pollution. The experiment provided useful experience for planning future international projects in the Black Sea.

Arctic and Antarctic Research Institute (AARI)

An oil spill drift model has been developed and applied for the Northern Sea Route region. The model can be used to simulate the oil spill evolution under influence of the wind, waves, current and ice. The oil spill model system consists of several modules: 1) a 3-D dynamic-thermodynamic model of ocean circulation for simulation of synoptic, seasonal and interannual variability of currents and water masses in the Arctic Ocean; 2) a wind-wave model which has been tested and verified by measurements in the Barents Sea and adapted to the Kara Sea; 3) an oil spill transport and evolution model (OilMARS v.2). The model represents an oil spill by a given number of spilletts released from a specific point at variable release rate. Under influence of the wind, currents including tidal and Stokes drift the spilletts propagate away from the release point. The oil spill models take into account spreading, horizontal diffusion, evaporation, photo- and biooxidation, emulsification (water-in-oil) and natural dispersion (oil-in-water). Each spillett is described by a set of parameters: coordinates, density, viscosity, oil mass remained in the water surface, oil mass lost due to evolution. The variations of the oil density and viscosity depend on the water

temperature, evaporation of the light oil fractions and emulsification. The model takes into account the ice concentration and ice drift. The ice cover slows down the oil evolution processes and has significant effect on the trajectories and velocities of the spilllets. Numerical experiments were carried out showing that the model is able to function under different environmental conditions.

State Design Office, Yuzhnoye (DOYu)

Sich-1M spacecraft (SC) was launched on December 24, 2004, carrying a side-looking radar onboard. It was planned to receive SLR images of the sea surface to monitor the oil spillages on the sea surface, but the spacecraft did not reach the calculated orbit. Therefore, only one image of the Black Sea were obtained, and this image contained no useful information about the sea surface. The main effort of Yuzhnoye has therefore been on promotional activities. In particular, the 5th Ukrainian conference on space research held on September 4-11, 2005 in Crimea was used for promotion of oil spill monitoring by SAR. More than 100 representatives from Ukraine, Russia and Georgia took part in the conference. A meeting of the Space Research Council of the National Academy of sciences of Ukraine was held during the conference to plan future SAR satellites to be launched in Ukraine. Yuzhnoye has prepared a report "Results of OSC SAR project of GMES program and configuration of Sich-3 spacecraft for continuous radar sensing". Furthermore, Yuzhnoye has started to develop a high resolution space SAR-based system Sich-3 for Earth radar sensing. The space system Sich-3 can be used in long-term GMES projects for sea medium monitoring, for finding the oil spillage on the sea surface.

Conclusions

The objectives of OSCSAR are ambitious and not all the planned work was realistic to complete within a period of 18 months. However, several significant results have been obtained regarding impact of slicks on gravity-capillary waves, modelling of wave damping by slicks, development and testing of oil drift model, and analysis of many SAR images in the three study areas, the Black Sea, the Caspian Sea, and the Kara Sea. Also a field experiment was conducted providing useful data for validation of SAR signatures of slicks. Further work is needed in all of the tasks in order to develop operational monitoring, classification, modelling and forecasting of oil spills.

Part A: Detailed projects results

Task 1: Wave modeling including effect of damping by oil films

Leader: Institute of Applied Physics

1.1 Methodology

The action of oil films on characteristics of gravity-capillary waves (GCW) has been studied in laboratory experiment using an original methodology developed at the Institute of Applied Physics, Russian Academy of Sciences [1, 2]. GCW were excited parametrically in a small container, and the surface tension coefficient values were retrieved from the measured GCW wavelengths, the damping coefficient due to films was estimated when studying regimes of the parametric wave excitation. This method was used previously when investigating monomolecular films (e.g., oleic acid and oleyl alcohol), modelling “biogenic” slicks on the sea surface.

The measurements were carried out in a small rectangular laboratory container filled with distilled water. Given amounts of oil were spread on the water surface and the surface waves were parametrically excited. The image of the waves was registered using a digital camera and the GCW wavelengths were measured. From the dispersion relation for GCW

$$\omega^2 = \left(gk + \frac{\sigma k^3}{\rho} \right) \tanh(kh),$$

where ω and k – the frequency and the wavenumber of the surface waves, σ is a sum of the surface and interfacial tension coefficients (for films with thickness much smaller than wavelength), ρ - the water density, h – the water depth in the tank the surface tension could be retrieved.

The total wave damping coefficient measured as a threshold of wave generation is equal to the damping due to film and damping due to walls and bottom of the tank. Corresponding formulas for calculations the different parts of the damping coefficient are presented in [1].

Surface tension and damping coefficient values for crude oil films and for diesel fuel films have been studied as functions of film thickness in the ranges of 0.1mm – 3 mm and 0.01mm – 3 mm, respectively, for various temperatures and at two wave frequencies.

1.2 Results

Surface/interface tension.

The dependencies of the surface/interfacial tension coefficient for different CO/OD films are presented in Fig.1-3. The surface tension coefficient values obtained at different frequencies for films at the same thickness are in good agreement. When the thickness achieves 2-3 mm the surface tension corresponds practically to the surface tension of crude oil or diesel fuel – the values are presented in the right part of the figures. One should mention that the occurrence of the peak in the dependencies in Fig. 1 is not the result of errors of the experiment.

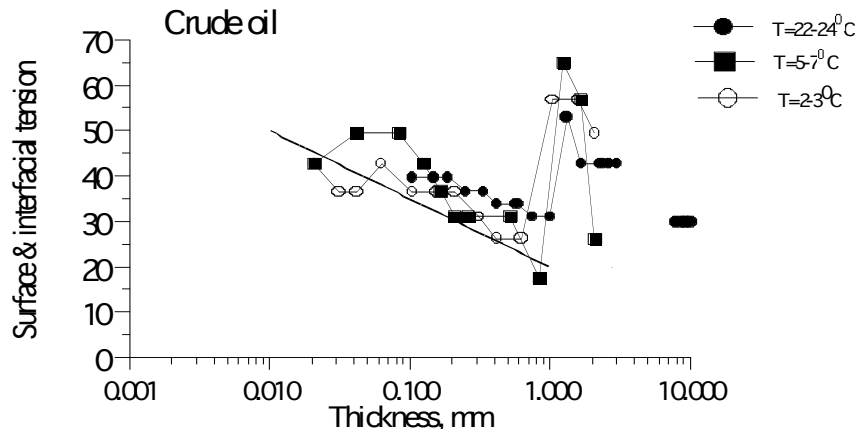


Figure 1. Surface/interfacial tension vs. thickness for a crude oil film at a frequency of 15 Hz and at different temperatures. The data at thickness values of about 10 mm correspond to the surface tension of crude oil.

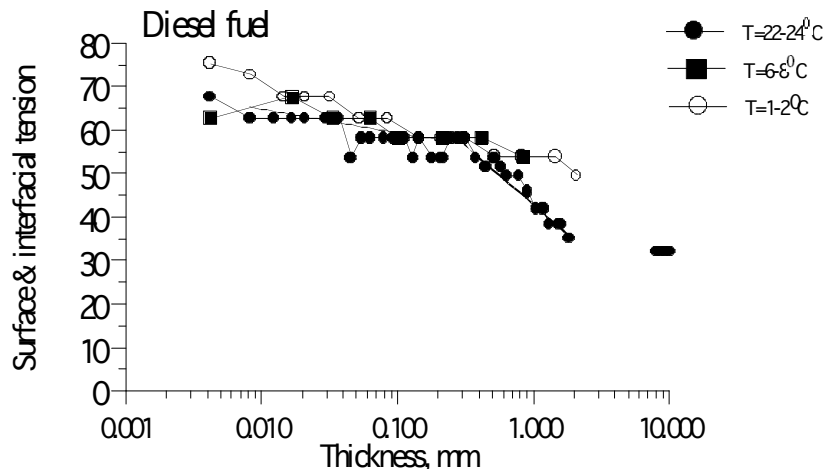


Figure 2. Surface/interfacial tension vs. thickness for a diesel fuel at a frequency of 27.5 Hz and different temperatures. The data at thickness about 10 mm correspond to the surface tension of diesel fuel.

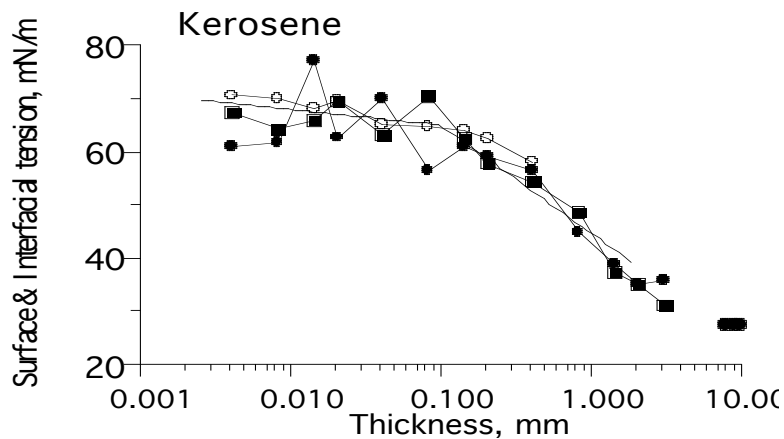


Figure 3. Surface/interfacial tension vs. thickness for a kerosene film at a frequency of 15 Hz and at different temperatures. The data at thickness values of about 10 mm correspond to the surface tension of crude oil.

The relative damping coefficient (the ratio of damping coefficients of GCW on the contaminated water and on clean water) as a function of thickness for oil and diesel fuel films are presented in fig. 4-7. The relative damping values are shown to have a maximum at a film thickness of about 1 mm; the values of the relative damping coefficient for crude oil films are typically 1.5-2 times larger than for diesel fuel films. Note, that the surface tension and the damping coefficient practically do not depend on the water temperature. Although the viscosities of the crude oil and the diesel fuel films increase when the temperature decreases, the relative damping is not changed significantly because the water viscosity increases when temperature decreases, too.

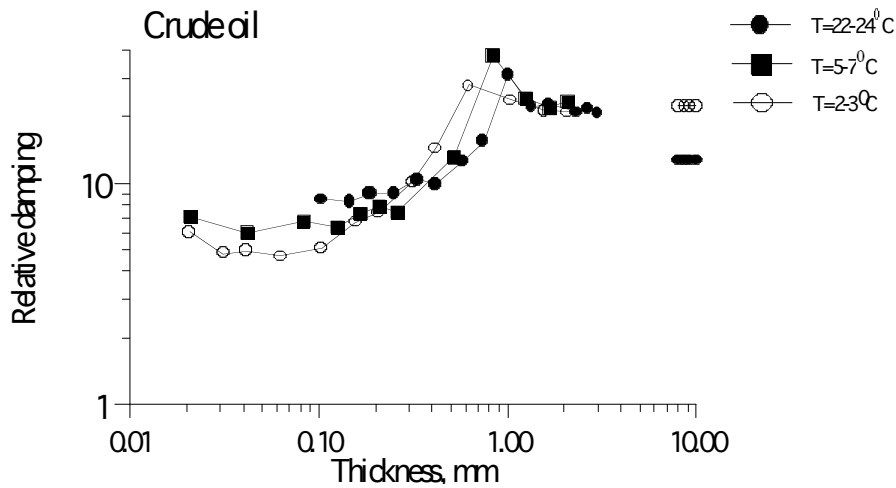


Figure 4. Relative damping vs. thickness for a crude oil at different temperatures and a frequency of 15 Hz. The data at the thickness about 10 mm correspond to the relative damping of crude oil.

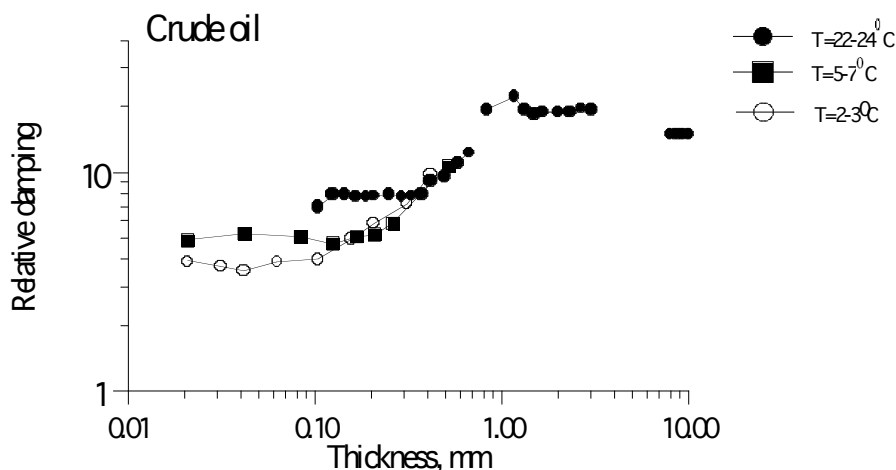


Figure 5. Relative damping vs. thickness for a diesel fuel at different temperatures and a frequency of 27.5 Hz. The data at the thickness about 10 mm correspond to the relative wave damping for crude oil.

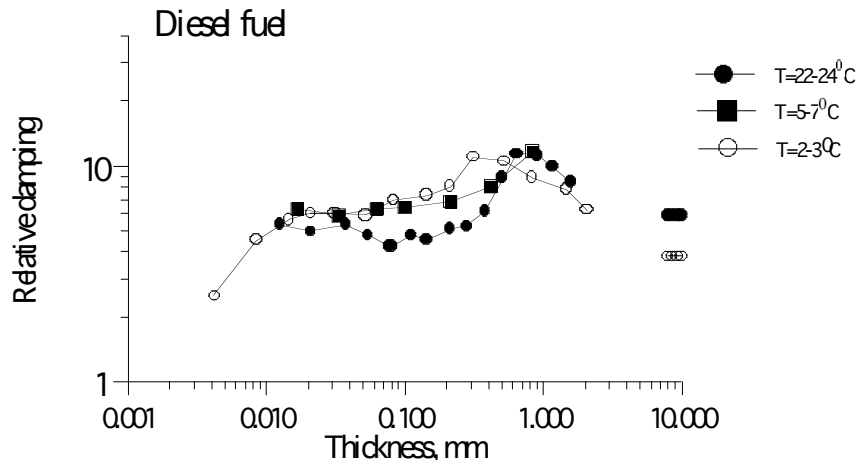


Figure 6. Relative damping vs. thickness for a diesel fuel at different temperatures and a frequency of 15 Hz. The data at the thickness about 10 mm correspond to the relative damping of diesel fuel.

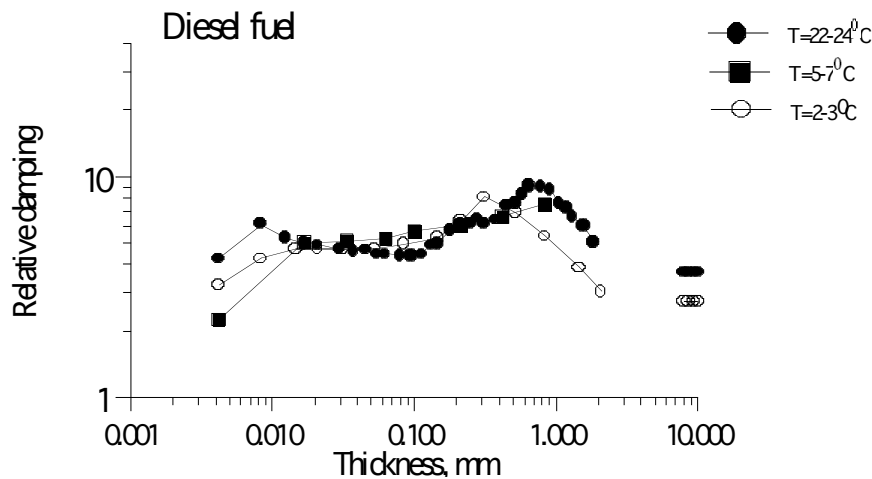


Figure 7. Relative damping vs. thickness for a diesel fuel at different temperatures and a frequency of 27.5 Hz. The data at the thickness about 10 mm correspond to the relative damping of diesel fuel.

1.3 Retrieval of film characteristics

The surface tension coefficient

The interfacial elasticity was assumed to be 0, and the interfacial tension was taken as 10 mN/m, although the influence of these values on the retrieved surface elasticity (for the considered range of film thicknesses) is negligible. When retrieving the surface elasticity the surface tension was taken as measured in the experiments. In the thickness range of 0.001 mm - 0.3 mm the surface tension as a function of film thickness h can be described by the following empirical dependencies

Crude oil films $\sigma = \sigma_0 - 40 - 5.3 * \ln(h)$

$$\text{Diesel fuel films } \sigma = \begin{cases} \sigma_0, h < 0.01\text{mm} \\ \sigma_0 - 15 - 3.2 * \ln(h), h > 0.001\text{mm} \end{cases}$$

$$\text{Kerosene films } \sigma = \begin{cases} \sigma_0 - 6 - 1.3 * \ln(h), h < 0.1 \text{ mm} \\ \sigma_0 - 23 - 8.8 * \ln(h) \end{cases}$$

Where $\sigma_0 = 68 \text{ mN/m}$ - the surface tension of clean water.

The elasticity of CO/OD films

The elasticity of CO/OD films was retrieved when fitting the experimental data and the theory by [3].

According to the model the damping depends on the following parameters of the viscoelastic film and lower fluid: ρ_- , ν - density & kinematic viscosity of a lower fluid; ρ_+ , ν_+ - density & kinematic viscosity of a viscoelastic film; E_+ , E_- - the surface and interfacial elasticity; ν_{s+} , ν_{s-} - the surface and interfacial viscosity; σ_+ , σ_- - the surface and interfacial tension. The obtained expression of wave damping is

$$\delta \approx$$

$$\left\{ 2\nu^* + \frac{1}{2}\nu_T + i\Gamma^{-1/2} [\sigma^* (1 - \rho_+) - \sigma_-] d^* + \frac{1}{2} i^{-1/2} \rho_+^* d^* \Gamma^{1/4} \nu_T / \sqrt{\nu^*} + \frac{1}{2} i^{-1/2} (\rho_+^* d^*)^2 \Gamma^{3/4} / \sqrt{\nu^*} [(R^2 - 1)] \right\} \\ \left[1 + i^{1/2} \Gamma^{-1/4} \nu_T / \sqrt{\nu^*} + i^{-1/2} \Gamma^{1/4} \rho_+^* d^* / \sqrt{\nu^*} \right]^{-1}$$

$$\text{where } \nu^* = k^{3/2} g^{-1/2} \nu,$$

$$\nu_T = \nu_{E+} + \nu_{E-} + 4\rho_+^* \nu_+^* d^* + \nu_{E+} \cdot \nu_{E-} d^* / (\rho_+^* \nu_+^*)$$

$$\nu_{E+} = E_+^* / n^* + \nu_{S+}^*$$

$$\nu_{E-} = E_-^* / n^* + \nu_{S-}^*$$

$$\Gamma = 1 + \sigma_+^* + \sigma_-^*$$

$$R = (\rho_+^* + \sigma_+^*) / (\rho_+^* \Gamma)$$

$$n^* = -iw^* = \sqrt{gk} \cdot n$$

$$\rho_{\pm}^* = \frac{\rho_{\pm}}{\rho_-}$$

$$(\nu_{\pm}^*, E_{\pm}^*) = k^2 \rho_-^{-1} g^{-1} (\nu_{\pm}, E_{\pm})$$

$$\nu_{s\pm}^* = k^{5/2} g^{-1/2} \rho_-^{-1} \nu_{s\pm}$$

The expression for wave damping is valid for the film thickness

$$d \ll d^* = \sqrt{\frac{\nu_+}{w}},$$

where w is the frequency of the surface waves.

Fig. 8 - 13 show comparison between theory and experiment for the relative damping coefficient as a function of thickness for CO/OD films. The experimental data are obtained in different experiments at a temperature of 20-22 C.

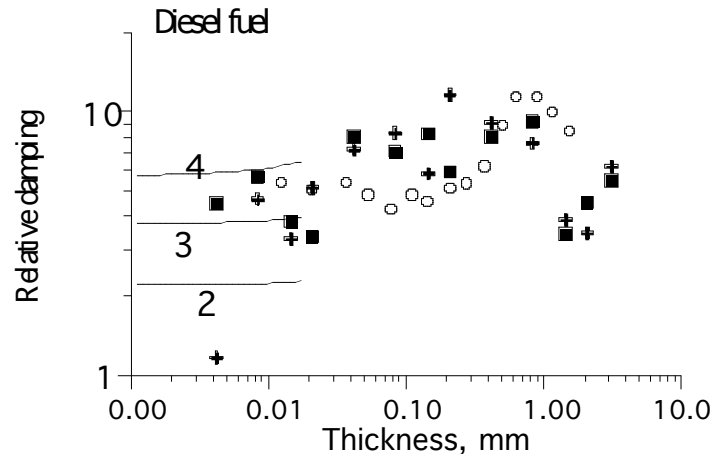


Figure 8. The relative damping vs. film fickness for diesel fuel film for a frequency of 15 Hz. The solid curves are theoretical calculations according to Jenkins's model. The numbers near the curves correspond to the film elasticities.

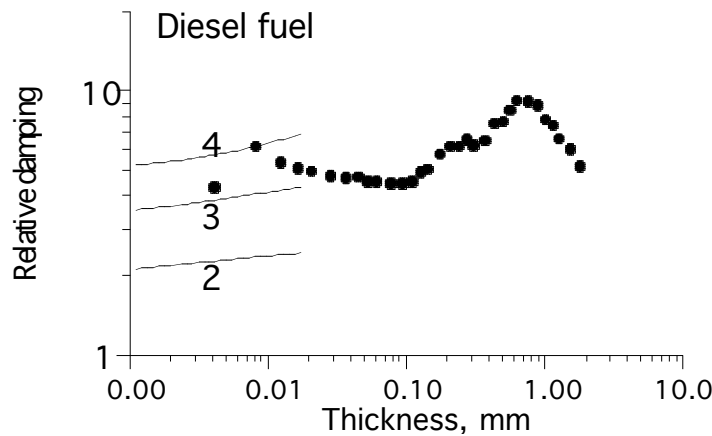


Figure 9. Same as in Fig.3 for a frequency of 27.5 Hz

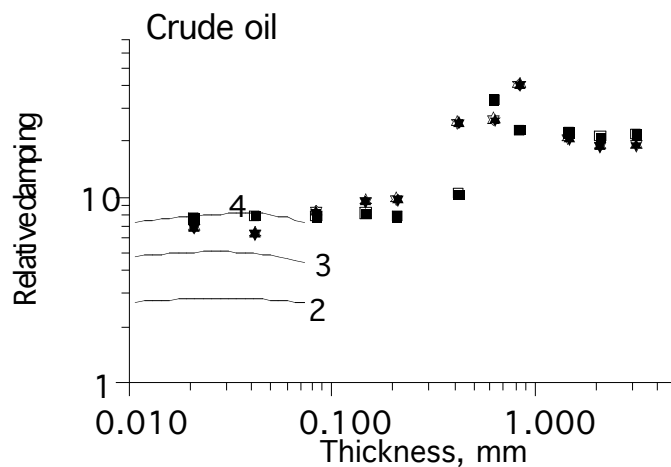


Figure 10. The relative damping vs. film fickness for crude oil film for a frequency of 15 Hz. The solid curves are theoretical calculations according to Jenkins's model. The numbers near the curves correspond to the film elasticities.

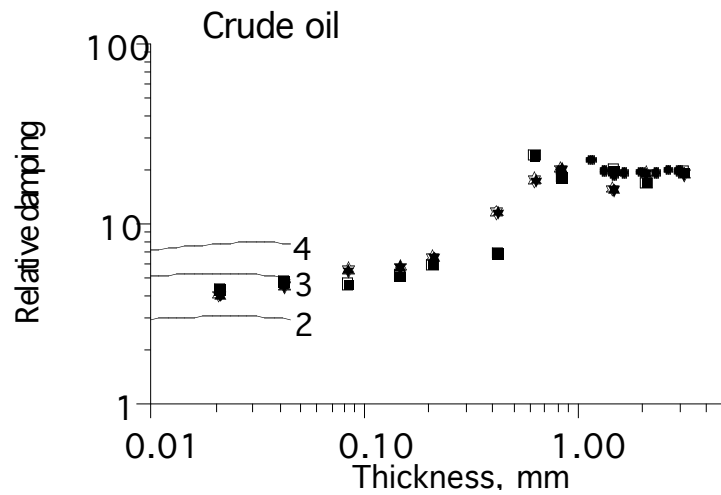


Figure 11. Same as in Fig.6 for frequency of 27.5 Hz

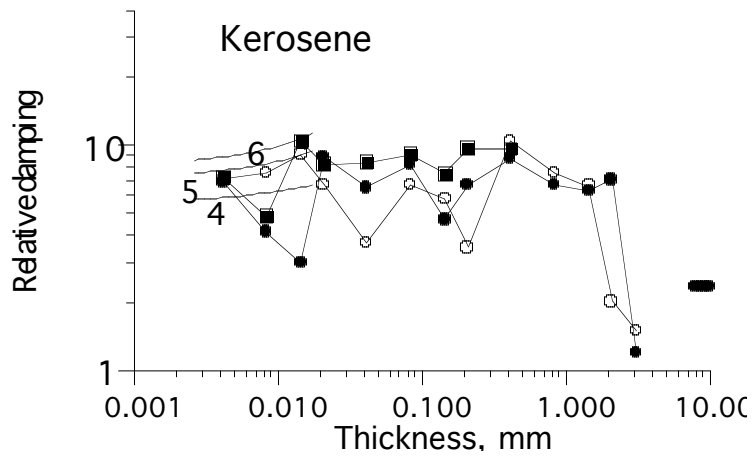


Figure 12. The relative damping vs. film fickness for kerosene film for a frequency of 15 Hz. The solid curves are theoretical calculations according to Jenkins's model. The numbers near the curves correspond to the film elasticities.

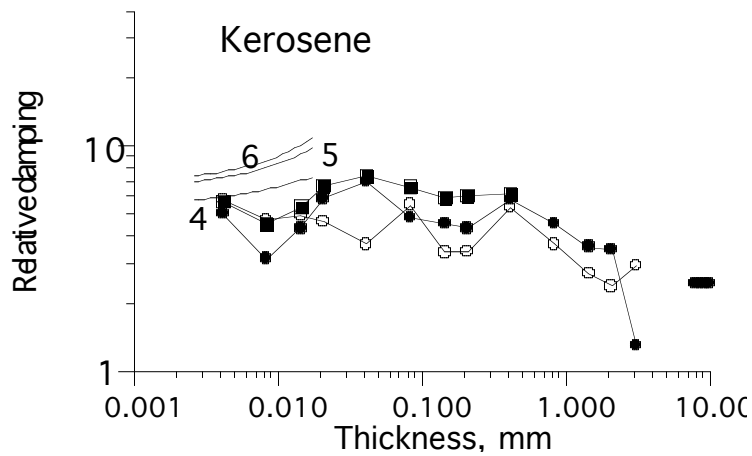


Figure 13. Same as in Fig.8 for frequency of 27,5 Hz

The CO/OD viscosity was estimated from special measurements of wave damping in a container filled in crude oil or diesel fuel. The retrieved film elasticity/viscosities are presented in Table 1.

Table 1. Retrieved CO/OD film viscoelasticity.

Film material	Surface & Interfacial tension	Interfacial tension mN/m	Relative viscosity	Surface Elasticity mN/m
Crude oil	As measured	0-10	22	3-4
Diesel fuel	-//-/-	0-10	8	3-4
Kerosene	-//-/-	0-10	1.3	4-6

1.4 Spectrum contrast in CO/OD spills

The retrieved values of CO/OD films were used to estimate the damping degree (contrast) in the frame of a local balance model [4]. According to the model the wavenumber spectrum of short wind waves is determined by local (in the wavenumber space) balance between the wind wave excitation, the linear wave damping due to films and phenomenological nonlinear (quadratic) spectrum limitation terms in the kinetic equation for the spectrum of wind waves when neglecting weak nonlinear wave-wave interactions. Then the contrast is described by the following formula

$$K(k) = \left[\frac{\beta(u_{*nsl}, k) - \gamma(0, \sigma_{nsl}, k)}{\beta(u_{*sl}, k) - \gamma(E, \sigma_{sl}, k)} \right]^n, \quad \beta > \gamma \quad n=1; \quad \beta < \gamma \quad n=-1 \quad (3)$$

where u_* the friction velocity, and the wind wave growth rate β is taken as $0.04(u_*k)^2/\omega$. One should stress that wind waves in this model are considered as quasilinear (free) waves, i.e. obeying the linear dispersion relationship. Comparison with results of our field experiments on radar/optical probing of oil and organic (biogenic) films is demonstrated in Fig. 14. In Fig. 14 the spectrum contrasts obtained in experiments with a monomolecular film of vegetable oil (elasticity 15 mN/m) and a film of diesel fuel (elasticity is 4 mN/m) are shown. The model (at wind 6 m/s) shows satisfactory agreement with observations, although, one should stress that the model is very sensitive to the wind velocity.

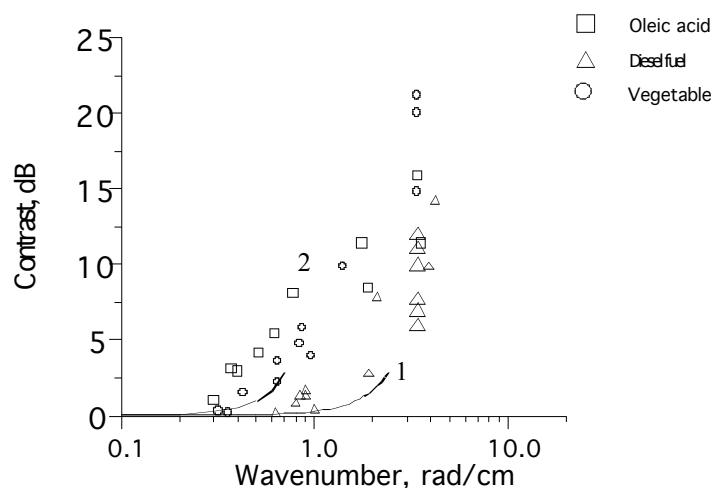


Figure 14. Contrast vs. wavenumber for different surfactants in field experiments with slicks. Data obtained with Optical spectrum analyzers and X-band radar. Wind velocity 4-6 m/s.

The solid curves are theoretical calculations according to the local balance model (wind velocity - 6 m/s): 2 - vegetable oil, 1 - diesel fuel.

1.5 Conclusions

The main results of Task 1 are the following:

- Experimental dependencies of the surface/interfacial tension coefficient and the damping coefficient for gravity-capillary waves on film thickness are obtained for CO/OD films.
- The damping is found to be slowly growing with film thickness in a wide thickness range from about 0.01mm to 1mm
- The relative damping coefficient practically does not depend on water temperature.
- The damping of wind waves in CO/OD spills can be roughly described by a local balance model taking into account the measured characteristics of CO/OD films.

Task 2: Radar scattering model

Task leader: Nansen International Environmental and Remote Sensing Center

During the project the NIERSC Team has developed the radar scattering model which takes into account effect of surface film (with known elasticity properties) on the sea surface and radar scattering. It is suggested that the model can be applied for analysis of radar data obtained at arbitrary geometry of radar observations, in particular corresponding to the ENVISAT ASAR.

2.1 Model approach

Proposed model is an extension of the recent Radar Imaging Model (RIM) by Kudryavtsev et al. (2005a) and Johannessen et al. (2005b) on a case of the sea surface covered by surface films of the different origin. The main elements of the model are the normalized radar cross section (NRCS) and wave spectrum modules as shown in Fig.15.

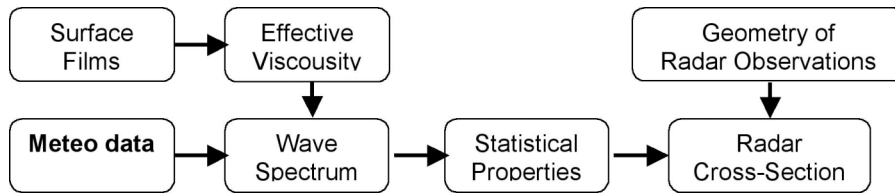


Figure 15. Diagram of the developed radar scattering model.

Following the background NRCS model by Kudryavtsev et al. (2005a), the sea surface is represented as a "regular" (non-breaking) wavy surface combined with a number of breaking zones, and the NRCS of the sea surface is presented as a sum

$$\sigma_0^p = \sigma_{0R}^p (1 - q) + \sigma_{0b} q \tag{1}$$

where σ_{0R}^p and σ_{0b} are the NRCS of the regular surface and a wave breaking zone correspondingly, and q is fraction of the sea surface covered by breaking zones.

Radar scattering from the regular surface is described within the frame of the composite model combining specular reflection and resonant (Bragg) scattering mechanisms, and reads:

$$\sigma_{0R}^p(\theta) = \pi R^2 \sec^4 \theta \cdot P(\eta_i, \eta_n) \Big|_{\eta_n=0}^{\eta_n=\tan\theta} + \int_{\Gamma} \sigma_{0br}^p(\theta - \eta_i) P(\eta_i) d\eta_i \tag{2}$$

where θ is the incidence angle; R^2 is an effective Fresnel reflection coefficient; $P(\eta_i)$ and $P(\eta_i, \eta_n)$ are one- and two-dimensional probability density functions (they are assumed near Gaussian) of the sea surface slope in the direction of the incidence plane (η_i) and in the orthogonal direction (η_n); σ_{0br}^p is the Bragg scattering NRCS expressed as

$$\sigma_{0br}^p(\theta') = 16 \pi k_r^4 |G_p(\theta')|^2 S_r(k_b, \varphi) \tag{3}$$

where k_r is the radiowave wavenumber; $\theta' = \theta - \arctan(\eta_i)$ is the local incidence angle (which can be approximated by $\theta' = \theta - \eta_i$ for small slopes); φ is the azimuth (radar look direction) relative to the wind direction; $|G_p|^2$ is the geometric scattering coefficients (their expressions can be found in e.g. Plant, 1990); $k_b = 2k_r \sin \theta'$ is the local wavenumber of the Bragg waves; and $S_r(k_b, \varphi)$ is the wavenumber (folded) spectrum of the surface elevations. In composite models the wave spectrum is divided in two intervals; small scale waves $k > k_d$ (with elevation variance h_s^2) and large scale waves $k < k_d$. In the present study dividing wavenumber is $k_d = k_r / 4$.

The second term in eq. (1) describes contribution of wave breaking to the sea surface NRCS. As suggested in Kudryavtsev et al (2003a), the radar scattering from an individual breaking zone can be described as specular reflections from very rough wave breaking patterns, and only breaking of waves with wavenumbers much less (in 10 and more times) than k_r can contribute to the radio-wave scattering. Parameters of very rough breaking zones are universal constants, and were chosen in Kudryavtsev et al (2003) so as to fit observations.

To calculate the NRCS in eq. (1) with (2) and (3) one needs to know the spectrum of Bragg waves, the mean square slope and fraction of the sea surface covered by breaking areas. At a given spectrum the up- and cross-wind components of the mean square slope are

$$\begin{aligned} S_{up}^2 &= \int_{k < k_d} k_1^2 B(\mathbf{k}) d\mathbf{k} \\ S_{cr}^2 &= \int_{k < k_d} k_2^2 B(\mathbf{k}) d\mathbf{k} \end{aligned} \quad (4)$$

where $B(\mathbf{k})$ is the saturation spectrum. Fraction of the sea surface q covered with breaking waves is also related to this saturation spectrum. Thus to complete the model one needs to quantify the wave spectrum.

In the RIM model (see Kudryavtsev et al., 2005a for details) shape of wave spectrum results from solution of energy balance equation. When wind field is uniform and surface current are absent source and sinks of the wave energy are in balance, and in the equilibrium range of the spectrum (far from the spectral peak) shape of the spectrum is found as solution of the following equation.

$$\beta_v(\mathbf{k})B(\mathbf{k}) - B(\mathbf{k})\left(\frac{B(\mathbf{k})}{\alpha}\right)^n + I_{sw}(k) + I_{pc}(\mathbf{k}) = 0 \quad (5)$$

where ω and \mathbf{k} are the intrinsic frequency and wave number vector related by the dispersion relation:

$$\omega^2 = gk + \gamma k^3 \quad (6)$$

$k = |\mathbf{k}|$, g is the gravity acceleration, γ is the surface tension, $\beta_v(\mathbf{k}) = \beta(\mathbf{k}) - 4\nu k^2 / \omega$ is the effective growth rate, which is the difference between the wind growth rate $\beta(\mathbf{k})$ and the rate of viscous dissipation (ν is the viscosity coefficient, which may include effect of the surface film), $\beta(\mathbf{k}) = C_\beta (u_* / c)^2 \cos \varphi |\cos \varphi|$, φ is the angle between wind and wavenumber vectors; u_* is air friction velocity, c is the phase velocity; C_β is a parameter. The second term in (**Error! Reference source not found.**) parameterizes the non-linear energy losses due to wave breaking and three wave-interactions. Parameters α and n in (**Error! Reference source not found.**) are functions of k ; details of their definition can be found in (Kudryavtsev et al., 2003).

The source term $I_{pc}(\mathbf{k}) + I_{sw}(\mathbf{k})$ describes generation of short surface waves by wave breaking. Depending on the scale of a breaking wave, two mechanisms are specified. First, due to the effect of the surface tension, short breaking waves with $k > k_{wb}$ (where $k_{wb} \approx 2\pi/0.3$ rad/m) are not disrupted, but produce "regular" trains of parasitic capillaries (bound waves). The second mechanism states that crests of longer breaking waves with wavenumber $k < k_{wb}$ are disrupted that leads to mechanical perturbations of the sea surface (see Kudryavtsev and Johannessen (2004) for more details). Explicit forms of the wave breaking sources are

$$I_{sw}(k) = \frac{c_b}{2\alpha_g} \omega^{-1} \iint_{k < k_{mb}} \omega \beta(\mathbf{k}') B(\mathbf{k}') d \ln k' d\varphi \quad (7)$$

$$I_{pc}(\mathbf{k}) = \beta(k_\gamma^2/k) B(k_\gamma^2/k) \phi(k_\gamma/k) \quad (8)$$

where $k_\gamma = (g/\gamma)^{1/2}$. Equation (8) describes the wave energy balance which is non-local in the k-space. This fact leads to an important consequence for the surface slicks issue,- spectral contrast of short wind waves caused by a surface film depends on the energy transfer from longer surface waves.

Extension of the spectral model (8) on the case of surface films can be done by means of the introduction of the viscosity coefficient (included in term $\beta_v(\mathbf{k})$) and surface tension γ which now to be dependent on physical/chemical properties of the surface films. There are two approaches to specify effective viscosity (ν_{ef}) and γ , - to define them theoretically (e.g. Levich, 1962; Jenkins and Jakobs, 1997) or experimentally (see IAP RAS Contribution). Expression for the relative damping coefficient derived by Jenkins and Jakobs, 1997 for the surface film of arbitrary thickness is given in the Task 1 results description. The effective damping coefficient for the monomolecular films reads (Levich, 1962)

$$\nu_{ef} = \nu \frac{1 - \frac{E_f k^2}{\rho \sqrt{2\nu\omega^3}} + \frac{E_f^2 k^3}{4\rho^2 \sqrt{2\nu^3\omega^5}}}{1 - \frac{2E_f k^2}{\rho \sqrt{2\nu\omega^3}} + \frac{E_f^2 k^4}{\rho^2 \nu \omega^3}} \quad (9)$$

where ν_{ef} and ν are the molecular viscosity coefficient in the presence of film and for clean surface respectively; and E_f is a surface film elasticity module. An example of model ν_{ef} for monomolecular films of different elasticity is shown in Fig.16.

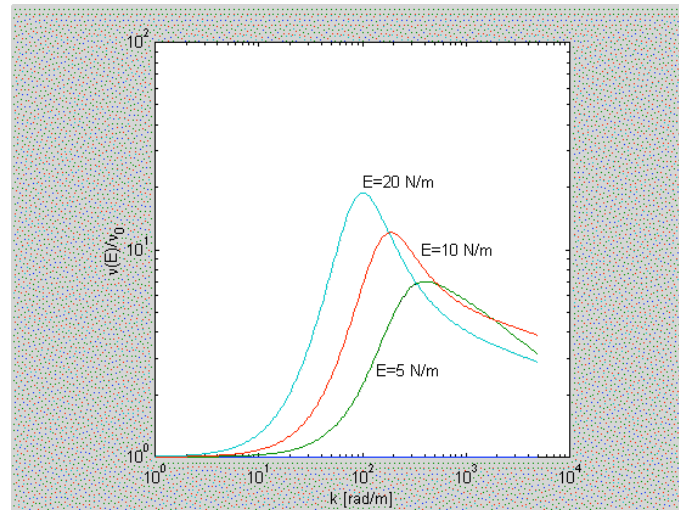


Figure 16. Effective viscosity coefficient (v) for the surface films of different elasticity.

Thus radar scattering model (1) with wave spectrum (5) supplemented with a model (e.g. (9)) or experimental effective damping coefficient describe NRCS of the sea surface covered by a film for given geometry of radar observation and wind speed (see Fig.15). Figure 17 a) and b) show model calculations of wavenumber spectra at wind speed 5 m/s on full model (5) and truncated model when wave breaking terms in (5) are ignored (so called a “local balance model”).

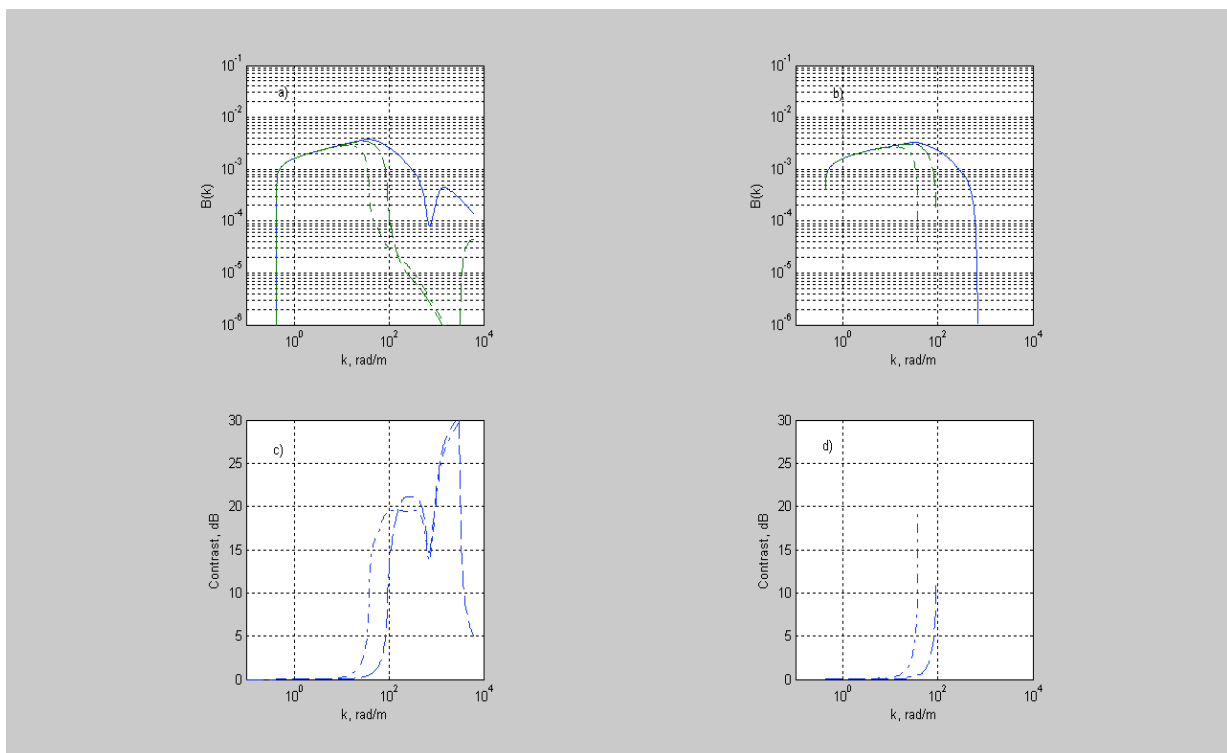


Figure 17. Wind wave spectra (upper plots) and spectral contrasts (lower plots) caused by monomolecular film with elasticity 10 mN/m (dash lines) and 30 mN/m (dash-dotted lines) at wind speed 5 m/s. Plots a) and c) show calculations on full model, and plots b) and d) show calculations on the “local balance model”. Spectra shown by solid lines are background spectra (no films)

It is clear that at background conditions (no films) "local balance model" underestimates energy level in high frequency range. In the full model the energy in this range is transported by the wavebreaking mechanism. In the presence of films the wave energy is significantly suppressed. According to the local balance model the energy at $k > 100$ rad/m is almost disappeared (spectral contrasts go to infinite). Unlike the full model (due to energy transfer from longer waves which are not affected by films) predicts some level of energy in the high frequency range. As shown below this important feature corresponds to the observations.

2.2 Validation of the background model

On the first stage the model has been verified against well-control observations, collected by CETP (France) with the airborne C-band radar called STORM [Hauser et al., 2003] during the VALPARESO experiment (see [Mouche et al., 2005a] and [Mouche et al., 2005b]). Some characteristics of this experiment are the following:

Aircraft Experiment (VALPARESO) :

- Region: Atlantic/British Chanel
- Radar: C-Band Real Aperture radar (5.35 GHz)
- Data (16 flights) : Normalized Radar Cross-Sections HH, VV,
Incidence from 10 to 45°,
Coincident buoy measurements (wind, temperature, waves,....).
Winds from 4 to 16 m/s,
Coincident ASAR/ENVISAT ASAR

The originality of this experiment is that this study is based on combinations of HH and VV radar cross-sections over a large range of incidence angles, and azimuth angles, in a variety of wind and wave conditions. These observations, compared to results from the NRCS model described above are used to identify the various mechanisms that can impact on the azimuth behavior of the radar backscatter, and to separate the different contributions to the total NRCS. These measurements were collected at conditions when no apparent surface contaminations were observed. In the context of the project, this part of study was focused on testing of ability of the model to reproduce background (no surface films) scattering properties of the sea surface.

Figure 18 shows example of extensive comparison of model predictions with radar data performed by Mouche et al. (2005b). As it follows from this figure the model is consistent with C-band radar scattering in the wide range of the incident angles and various radar look directions. More examples of the comparison can be found in Mouche et al. (2005b), and the main conclusion is that the NRCS model is quite adequate to the real data, and may further used for applications, - radar properties of natural and mineral surface films in our case.

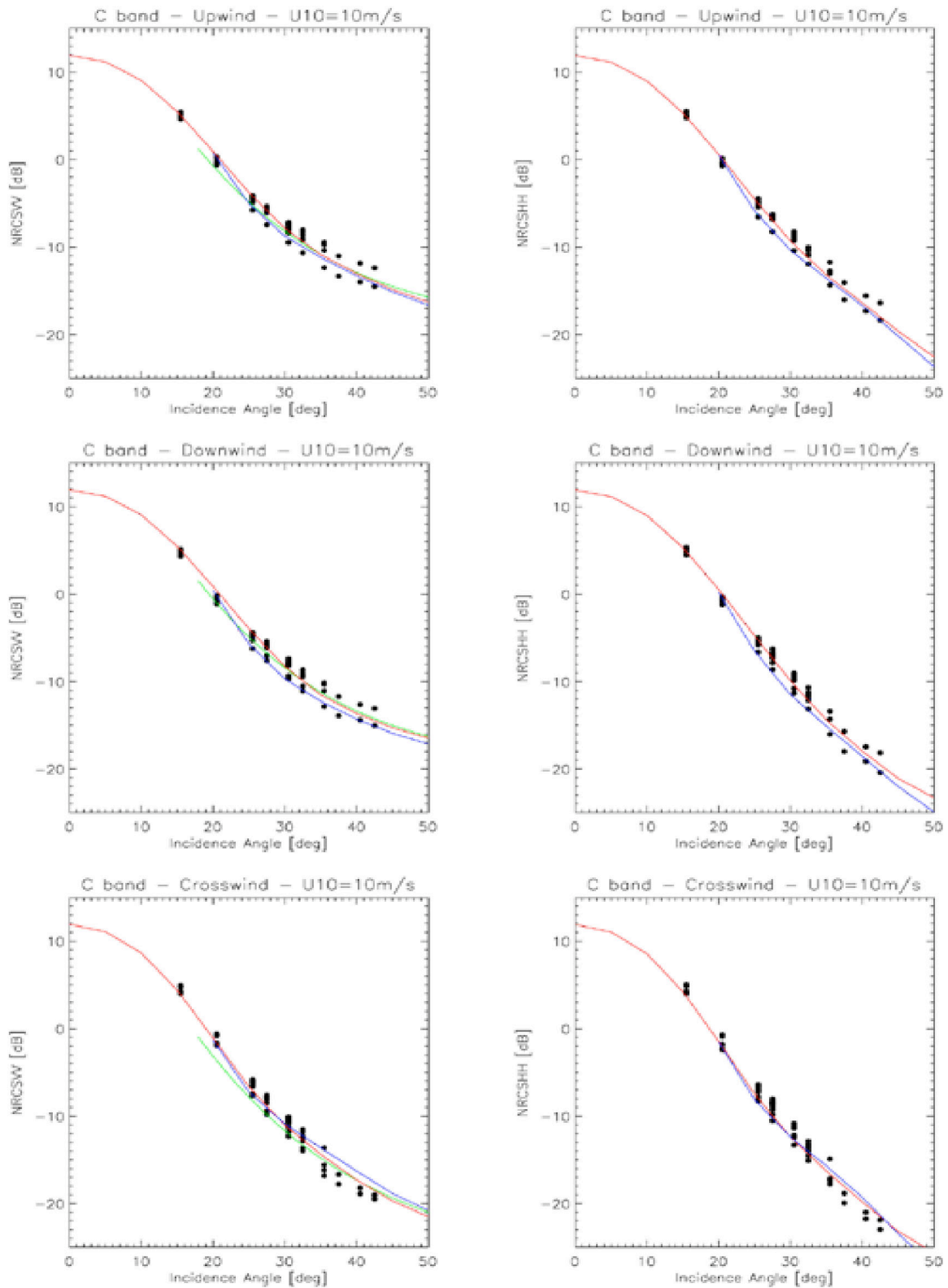


Figure 18. Comparison of measured (solid dots) and model (red lines) C-band NRCS at VV- (left column) and HH- (right column) polarizations vs. incident angles at wind speed 10 /s. Upper, mid and lower plots correspond to up-, down- and cross-wind radar look directions

2.3. Validation of the model against available published data.

Gade et al. (1998) presented an extensive laboratory experimental study of effect of surface films on radar scattering. Conditions of the experiment, equipment and characteristics of surface films are given below:

Radar:	X-band, VV and HH pol Ka- band, VV pol	
Fetch:	15m	
Wind speed range:	from 3 to 15 m/s	
Reference level:	0.65m	
Surfactants:		Concentration
• Hexadecanol		31.5 mN/m
• Hexadecyl amine		29.0 mN/m
• Hexadecyl trimethyl ammonium bromide		25.5 mN/m
• Oleyl alcohol		25.5 mN/m
• Hexadecanoic acid methyl ester		46.0 mN/m

Figure 19 shows example of the model wave spectra and spectral contrast corresponding to the conditions of the experiment. Remarkable feature of wave spectrum is a peak in the capillary range which corresponds to the parasitic capillaries generated by breaking of the dominant waves.

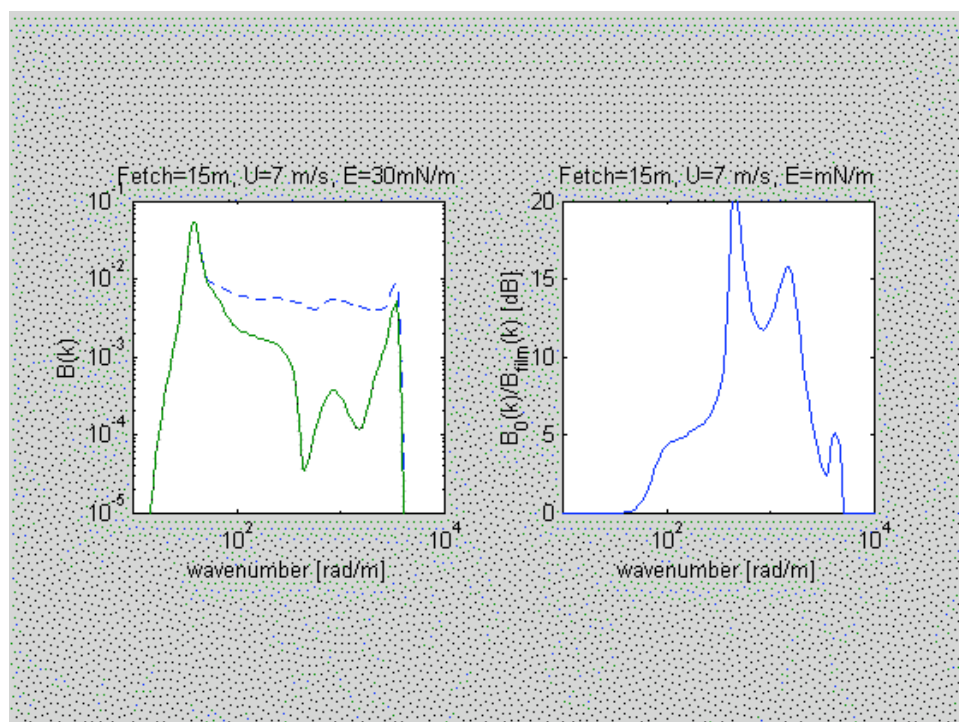


Figure 19. Wave spectra (left) and spectral contrast (right) for the conditions of the experiment by Gade et al. (1998). Parameters used for the calculations are listed in the header of the plots. Spectrum shown by dash line is background (no film) spectrum

Figure 20 shows results of model simulations of lab measurements of the NRCS of the clean water surface and covered by the films for two incidence angles and VV and HH polarizations. At low wind speed the model correctly reproduces suppression of radar scattering in the presence of the surface films, as well as recovery of backscatter at high (10 m/s) winds. However, at intermediate winds shape of the model curves (except for VV, 54 deg.) differs from observations. The reason of such discrepancy is not clear and will be investigated later.



Figure 20 Example of model simulation of X-band radar backscatter for VV and HH and incidence angles 36 and 54 deg. at different wind speeds where the blue line shows the backscatter for clean water and the green line for surface film. Observations from Gade et al., JGR, Oceans 103, C2, 1998) are included for comparison where blue dots indicate clean water and blue circles indicate surface film.

Figure 21 presents result of model comparison for Ka-band when radio-waves are scattered on capillary surface waves. As follows from Fig. 5 these waves are parasitic capillaries generated by micro-scale breaking of dominant waves. As measured, at low wind speeds radar scattering in Ka-band is significantly suppressed, on 20-25 dB, and is recovering at winds exceeding 10 m/s. These features are reproduced by the model.

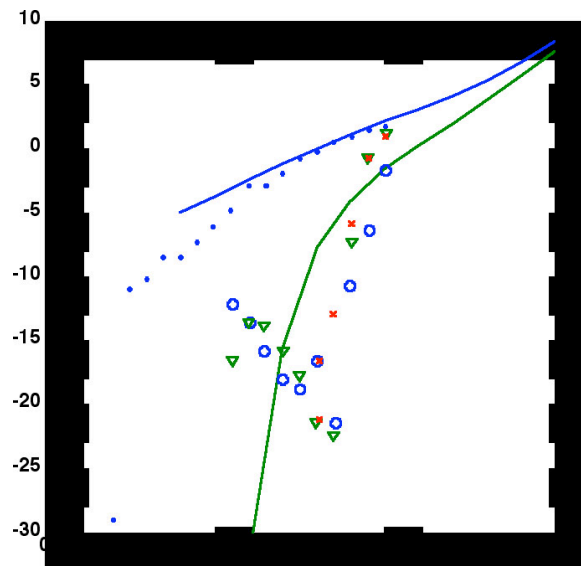


Figure 21. Example of model simulation of Ka-band radar backscatter for VV at different wind speeds where the blue line shows the backscatter for clean water and the green line for surface film. Observations from Gade et al., JGR, Oceans, 103, C2, 1998) are included for comparison where blue dots indicate clean water and blue circles and green triangles indicate surface covered by surface film.

The developed model was further verified against well controlled field experiments on radar scattering from the surface covered by artificial films. The experiment included measurements of NRCS of water covered by different types of films by multi-frequency radar. It is described in Gade et al. "Imaging of ocean surface films by SIR-C/X-SAR". J.Geophys. Res. 103. C9. 1998. Fig. 22 shows a slick of oleyl alcohol as seen by spaceborne SIR-C/X-SAR in different bands. The model was run for the parameters reproducing environmental conditions of the experiment and proved to be consistent with experimental data. The measured dumping ratios (i.e. the ratio between NRCS of clean water and NRCS of water with slick) are indicated on Fig. 23 as yellow areas. The modelled ratios in general are in good agreement with the observed ones, though they are somewhat lower for 5m/s situation, especially for X-band.

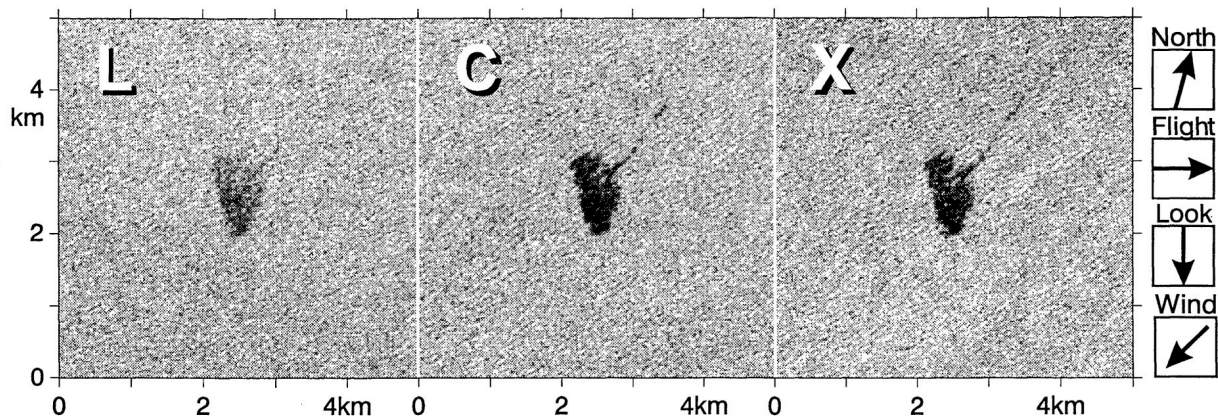


Figure 22. SIR-C/X-SAR images of artificial oleyl alcohol slick during the experiment in German Bight. The images are for VV polarization, L-, C- and X-bands. The illustration taken from Gade et al. Imaging of ocean surface films by SIR-C/X-SAR. J.Geophys. Res. 103. C9. 1998.

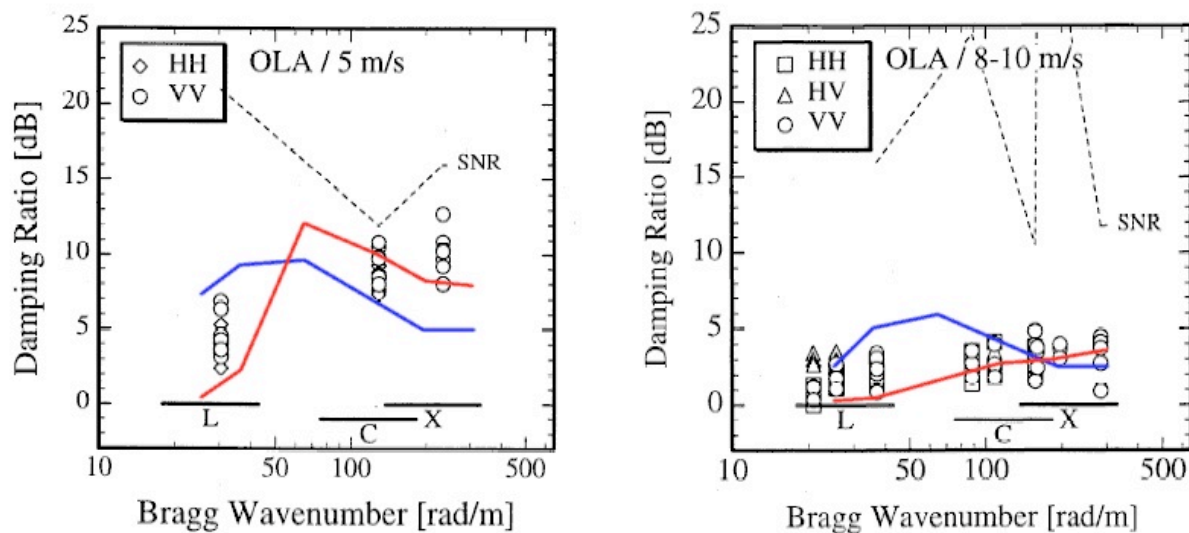


Figure 23. Comparison of measured and simulated dumping ratios for several radar frequency bands. Symbols are measurements by Gade et al., "Imaging of ocean surface films by SIR-C/X-SAR". J.Geophys. Res. 103. C9. 1998 (their Fig.4 and 7). Solid lines are model calculations for up-wind (red line) and cross-wind radar look directions, VV polarizations.

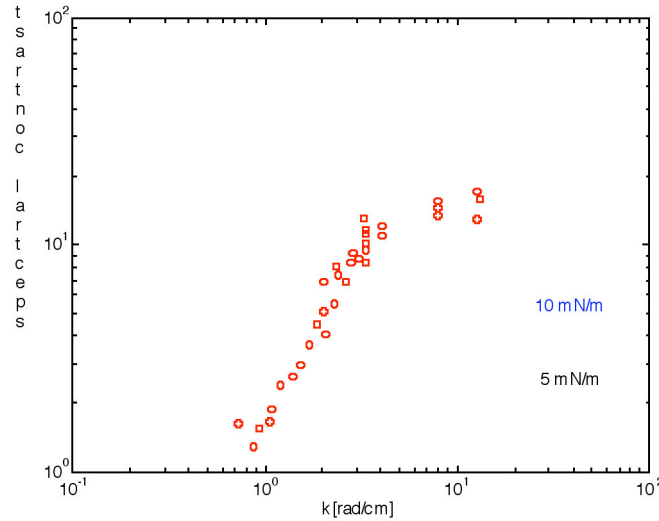


Figure 24. Wind wave spectral contrast in the slick of vegetable oil at wind speed 6-7 m/s. Red circles are field measurements by IAP Team (taken from PhD Thesis by I.Sergievskaya), lines are model simulations with monomolecular film damping coefficient (9) with two different elasticity.

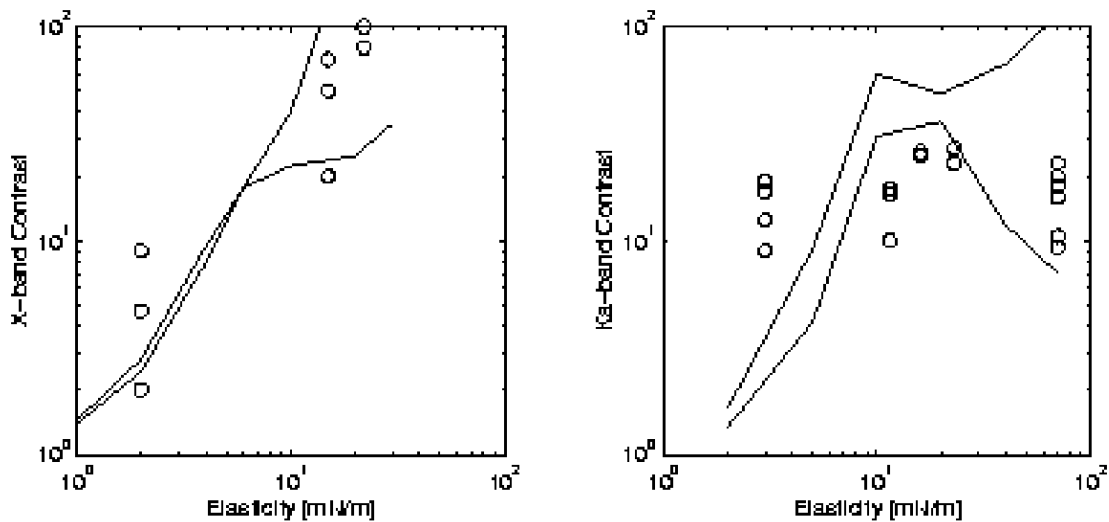


Figure 25. Dependence of radar contrasts on elasticity of the surface film. Left plot: X-band, wind speed 2-3 m/s; right plot: Ka-band, wind speed 6-8 m/s. Red circles are field measurements by IAP Team, Ermakov et al., Preprint No 668, 2004 (their Fig. 2a and 2b), lines are model simulations with damping coefficient (9).

Figures 24 and 25 illustrate results of model simulations of field measurements made by IAP Team. In the whole, model spectral contrasts shown in Fig. 24 are consistent with measurements, though overestimate of the data in the wavenumber range 4-8 rad/cm is apparent. In the X-band the model quite well reproduces the radar contrast vs. film elasticity. Unlike in Ka-band observed radar contrasts are almost independent on film elasticity while the model predicts pronounced trend with increasing E.

2.4. Surfactant films in presence on surface currents

In the ocean conditions spatial distribution of surface films (natural and mineral) is affected by surface currents. Surface films accumulate in the convergence zones and can often be seen on radar images as intricate pattern of low backscatter zones. The developed model can be used to simulate such a picture if elasticity of surface films is known. For the purpose of demonstration of this ability we used the 2-dimensional current field which is an output of high resolution hydrodynamic model (Eldevik, T., and K. B. Dysthe (2002), Spiral eddies, *J. Phys. Oceanogr.*, 32, 851–869), and related to a frontal eddy. It was assumed that surface areas where current convergence exceeds a given threshold level is covered by surface film with elasticity 5mN/m^2 . The model current field is shown on Fig. 26. Numerical lagrangian tracers (shown by dots) indicate location of convergence zones.

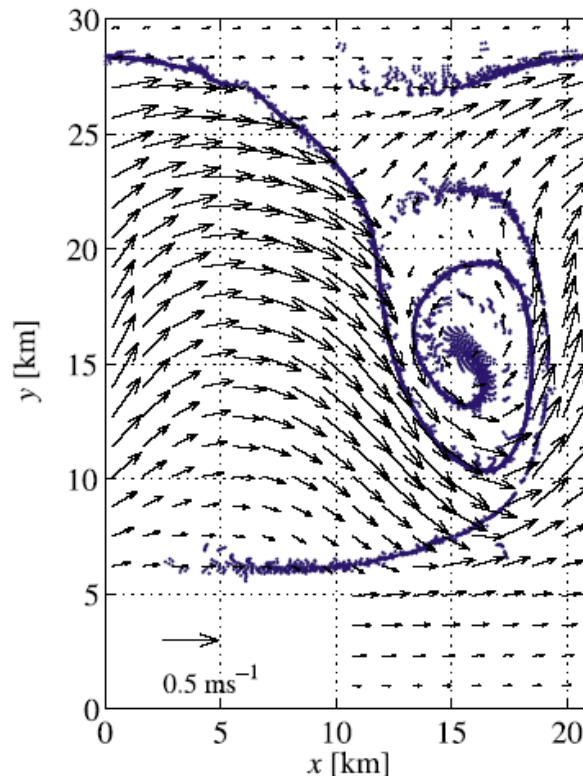


Figure 26. Modelled surface current field in a frontal eddy. Small blue dots are lagrangian tracers accumulated in the convergence zones. The illustration is taken from Eldevik, T., and K. B. Dysthe (2002), *Spiral eddies, J. Phys. Oceanogr.*, 32, 851–869.

The corresponding model calculations of the radar signature are shown in Fig.27 for winds of 5 m/s and 15 m/s. As expected, the surfactants significantly suppress the radar scattering. The 4-dB contrast of the dark features in Figure 27a which is related to the convergence zones attains a shape in very good agreement with the pattern in Figure 26. Consequently, “clean” surface convergence zones are bright, while the presence of surfactants will turn the NRSC of the convergence zones darker. At stronger wind conditions, the surfactant impacts gradually disappear (Figure 27 b). At this speed the impact of the wind forcing therefore overpowers the effect of surfactant damping. The magnitudes of the damping in these simulations are sensitive to the choice of elasticity.

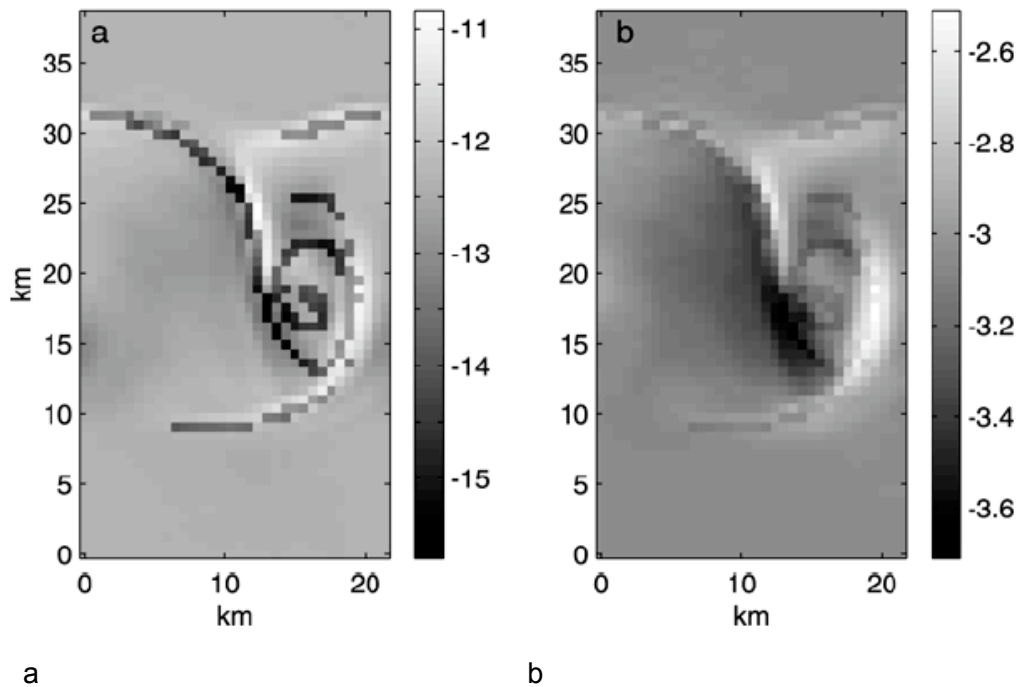


Figure 27. Simulated NRCS field (in dB) for the eddy current field in presence of surfactants. Wind speed (a) 5 m/s and (b) 15 m/s. Radar geometry is as for ERS SAR.

2.5. C-band radar sensitivity study

Preliminary results of the testing showed that the model is capable to reproduce the main features of wind waves and backscatter contrasts caused by surface films. Therefore we have adopted the model for the radar scattering sensitivity study.

Figure 28 shows some results of sensitivity of radar scattering (VV, HH and polarization ratio PR) to surface film at different incidence angles. At small incidence angles (< 15 deg.) radar scattering does not feel the films. The reason is that at these conditions the main contribution to the NRCS comes from the radio-wave specular reflections from waves with wavelength in 4-times exceeding radar wavelength (> 20 cm). Since these waves are long enough they are not affected by the films. At moderate incidence, radar sensitivity enhances with increasing incidence angle (see VV at 5 m/s in Fig. 28). For HH-contrast maximum of the sensitivity occurs at incidence angles around 30 deg., and then becomes weaker at larger incidence. The reason of such behavior is wave beaming which (on the one hand) significantly contributes to the NRCS at HH and their impact is an increasing function of incidence angle, and (on the other hand) do not affected by films. Suppression of Bragg waves by the films results in increasing contrasts of polarization ratio (PR). At high wind speed (lower plots, 10 m/s) radar contrasts are significantly reduced, that is explained by increased role of wind forcing in respect to the film damping.

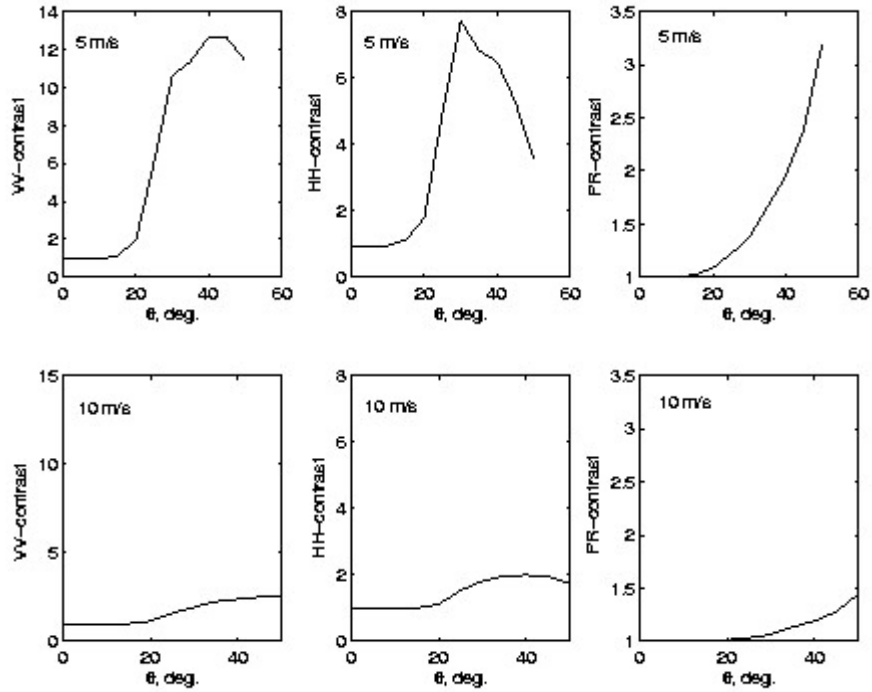


Figure 14. C-band Radar Contrasts vs. incidence angle for surface film with $E=20 \text{ mN/m}$ at wind speeds 5 m/s (upper plots) and 10 m/s (lower plots)

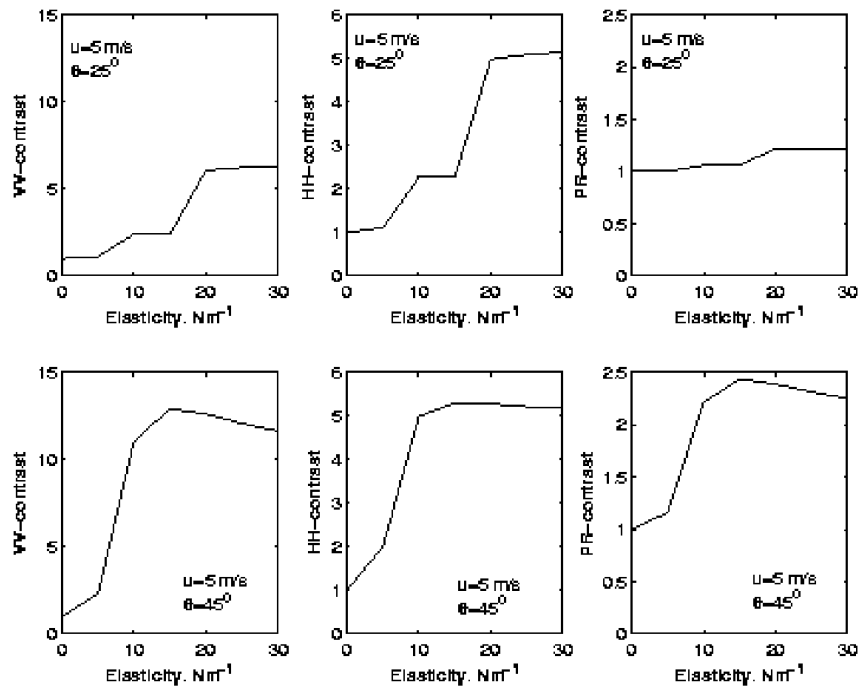


Figure 29. C-band Radar Contrasts vs. Film Elasticity at 25 and 45 degree incidence, 5 m/s wind speed

Figure 29 illustrates sensitivity of C-band radar scattering to the film elasticity at wind speed 5 m/s and two values of incidence angle. At small E radar contrasts increase with increasing film elasticity. However at $E > 15-20$ mN/m radar sensitivity is saturated.

2.6 Conclusions

The main results are the following:

- The model of short wind wave spectrum is extended on the case of surface film. The input parameter is the effective damping coefficient known from a theory or derived empirically (Task 1.2).
- The spectrum model is incorporated with radar scattering model. Thus, an improved model of radar scattering from the sea surface covered by natural/artificial films is completed (Task 2).
- The background radar scattering model (without impact of the films) is verified against extensive C-band dual polarization radar scattering measurements obtained by CETP (France) in aircraft experiments. It was found that the model consistently reproduces the radar scattering properties of the sea surface in wide range of incidence angles and wind speeds, and can be further used in oil spills applications.
- The model was compared with available lab and field measurements of radar contrast of artificial slicks in L- to Ka-bands. In overall, a reasonably good agreement is achieved (Task 1.2 and 2).
- A sensitivity study of dependence of dual-polarization C-band radar scattering on surface films parameters has performed (activity towards development of improved oil spills detection algorithm).
- The model was applied to assess the radar signatures of surface films redistributed the current (activity towards further discrimination of surface films and their look-alikes)

Task 3.1: Satellite image analysis in Caspian and Kara Seas

Task leader: Research Center for Earth Operative Monitoring (NTsOMZ)

3.1.1 Description of work performed

The automated techniques of sea surface oil pollution identification based on SAR data are still under development now. So at the first stage of the development of the system for marine oil pollution monitoring the NTs OMZ uses the expert appraisal in GIS environment as a base method for oil spill identification. The approach implies that a final decision on a probable genesis of each slick must be made by an experienced expert-interpreter. When interpreting there are used the following main characteristics of slicks: shape, size, texture, boundary definition, and brightness properties. Moreover, all available data on surface current fields, probable pollution source positions, and surface wind characteristics are analyzed. An expert-interpreter will use a probability value of the fact that the analyzed slick is of man-made genesis; this probability value is calculated by software tools including a radiometric correction of the SAR images using a polynomial approximation of brightness profile of homogeneous fragment of image (Fig. 30), speckle noise suppression, adaptive determination of optimal threshold values and slick contour boundary discrimination (Fig. 31).

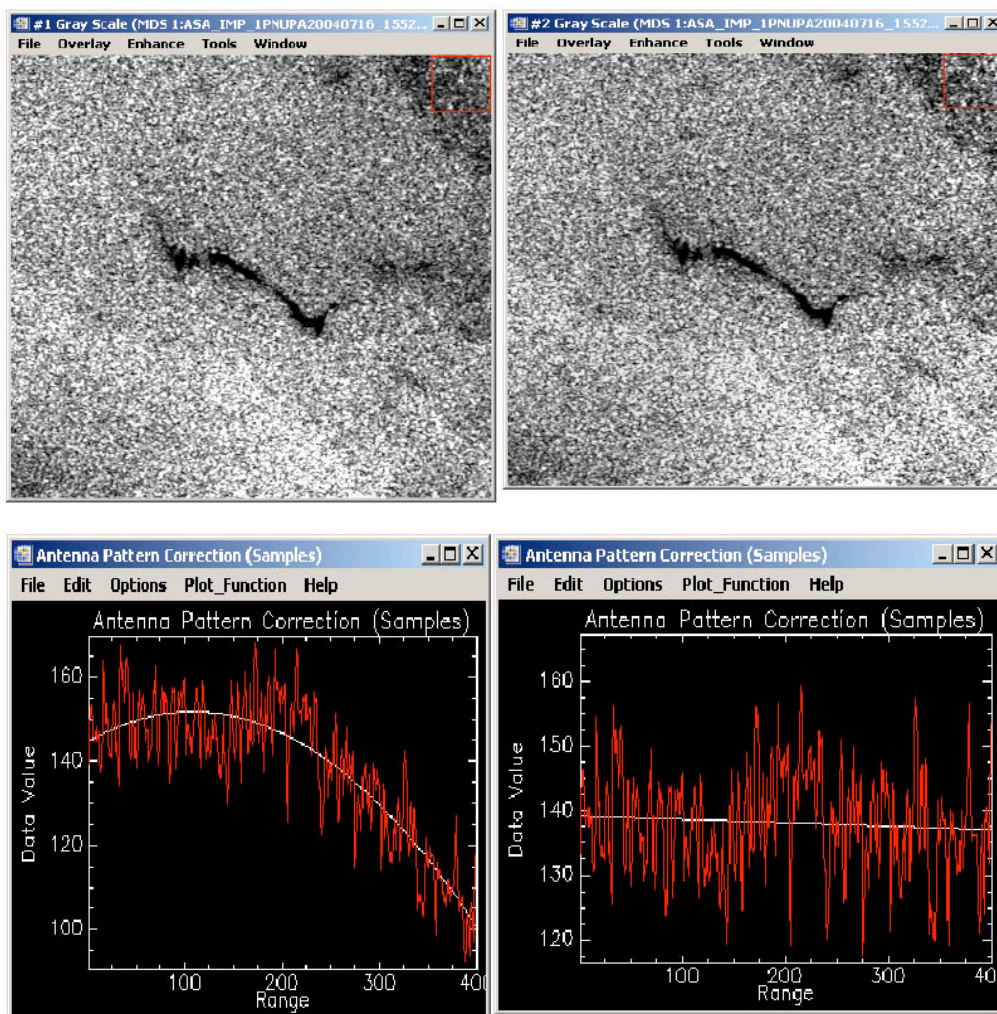


Figure 30: An example of radiometric correction of SAR image. The second degree polynomial approximation using brightness profile of an homogenous image fragment

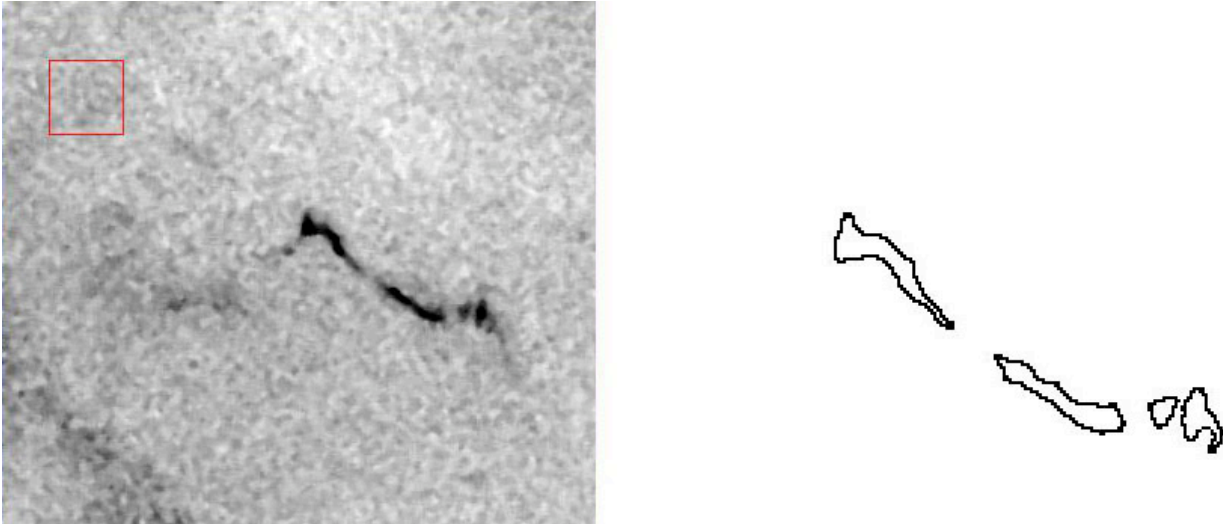


Figure 31: An example of speckle noise suppression and slick contour discrimination

Furthermore, statistical characteristics vector of a slick (area, perimeter, contour complexity, standard deviation for slick and background pixels in dB, etc.) is generated and a supervised classification using standard algorithms is made. For lack of sufficient volume of verified training data needed for classifiers training, NTs OMZ started the development of an approach based on simplified heuristic algorithms.

In the absence of verification of processing results using quasi-synchronous ground observations and with the purpose of a higher discrimination probability of man-made and natural genesis slicks, present investigations were focused on studying of the of SAR, visible and IR data synergetic analysis possibilities (using the signs of oil pollution in visible and IR bands).

The satellite images of the Caspian Sea waters close to the Apsheron (characterized by a high probability of necessary cloudlessness within the imaged area as well as by reasonably high probability of oil pollution) were used in pilot studies. Simultaneously there was analyzed a possible correlation between the Caspian Sea large oil pollution of more than 10 sq. km in area and the activation periods of lithosphere activity (earthquakes). The importance of this analysis is that if the correlation is determined it would enable to advance reliability of identifying slick genesis. The research on a possible correlation has been just started and performed in the context of the Russian VULKAN spacecraft launch preparation (its main mission is to acquire data on the earthquakes forerunners). It should be noted that the offshore oil-field region near the Apsheron is situated within a seismic zone where approximately ten earthquakes of more than grade 3 occur in a year.

A synergetic analysis of SAR, visible and IR data was carried out using both the ASAR/ENVISAT quick-looks available in the ESA's archive and the NOAA/AVHRR data available in the NTs OMZ's archive. A proximate analysis of the data acquired throughout 2004 was performed. A large size of the slicks analyzed allowed the use of the EOLISA quick-looks of the ASAR/ENVISAT images in GM mode (1km pixel size). The analysis carried out enabled two Events to be revealed. As an example below there are given the images (and results of their analysis) for Event 1 (27 May 2004).

Figure 32 a shows a segment of the ASAR/ENVISAT GM image of the south-western part of the Caspian Sea. Large slicks to the east from the Apsheron are clearly seen. The synergetic analysis used the AVHRR/NOAA data. Cloudiness was estimated by use of a standard albedo map at $0.8\mu\text{m}$ in %, shown in Figure 32 b. As may be seen the slick region (to the east from the Apsheron) is cloud free. The specific lined clouds observed along south-western coast marked the

lithospheric active fractures (see Fig.36). These clouds are forerunners of the earthquake that took place the next day on 28 May 2004. The epicenter of earthquake is marked by a red arrow in the right figure.

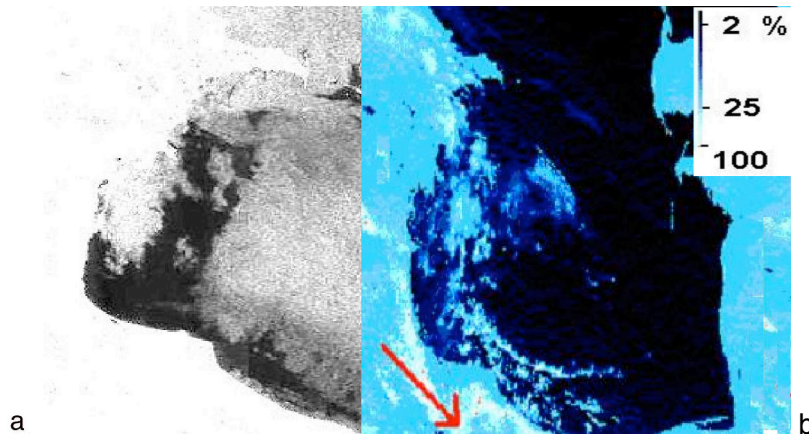


Figure 32: a) segment of ASAR/ENVISAT GM image of south-western part of the Caspian Sea; b) fragment of standard albedo map at $0.8\mu\text{m}$ in %; AVHRR/NOAA data were used.

While the synergetic analysis carrying out there were usually constructed the sea surface temperature (SST) maps (Fig. 33 a) based on the AVHRR/NOAA data. A considerable heating of sea surface in the slick field to the east from the Apsheron is not observed (marked by a red arrow). Fig. 33 b shows a precision map of solar radiation albedo at $0.8\mu\text{m}$ in % (atmospheric correction as well as correction of distortions caused by a variation of the Sun's and spacecraft zenith and azimuth angles were performed when generating this precision map). Position of a local minimum of albedo to the east from the Apsheron (marked by a red arrow) is nearly the same as that of the slick on the ASAR/ENVISAT image.

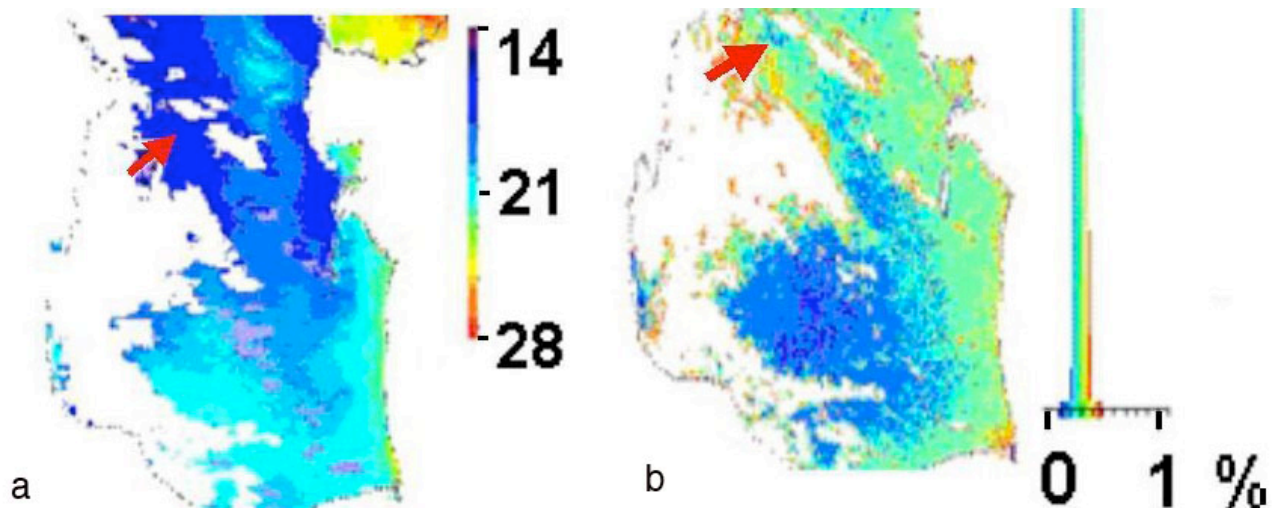


Figure 33. a) a fragment of SST map in $^{\circ}\text{C}$; b) precision map of backscattered solar radiation albedo at $0.8\mu\text{m}$ in %.

Examples of wind speed are shown in Fig. 34. Chlorophyll concentration maps based on SEAWIFS/SEASTAR data (left) and MODIS/AQUA/TERRA data (central), and a hydrosol albedo map at $0.6\mu\text{m}$ based on AVHRR/NOAA data (right) are shown in fig. 35.

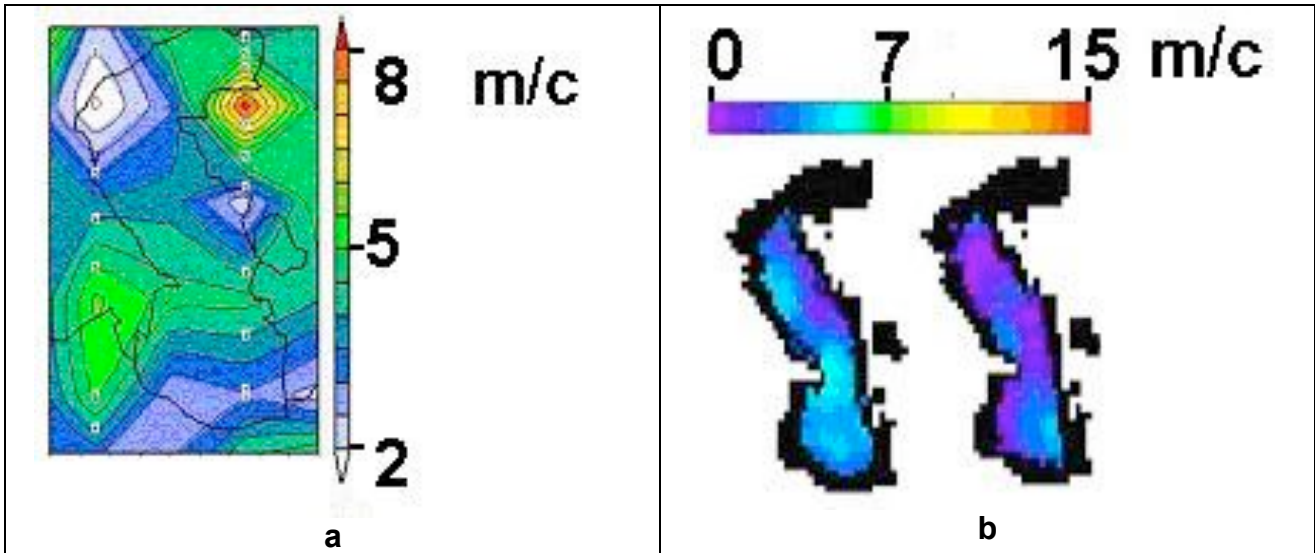


Figure 34: Examples of wind speed in the Caspian Sea from NCEP data

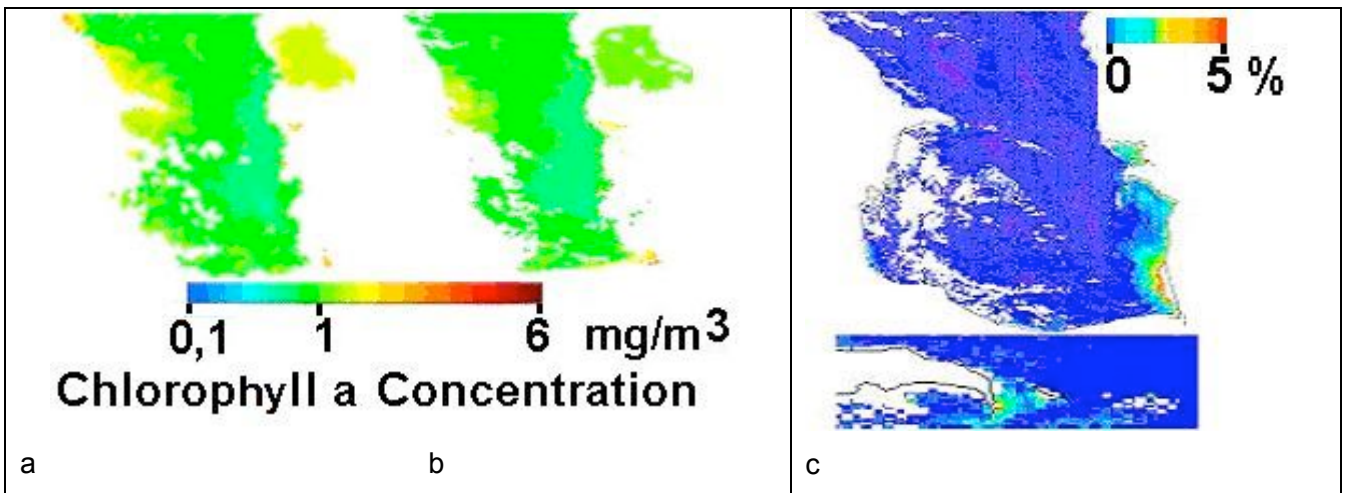


Figure 35: Chlorophyll concentration maps based on SEAWIFS/SEASTAR (a) and MODIS/AQUA/TERRA data (b). Hydrosol albedo map at 0.6µm in % based on AVHRR/NOAA data is shown in (c).

The results of the carried out synergetic analysis allowed to draw a conclusion that in both discussed above Events a large sea surface oil pollution had occurred near to the Apsheron. Moreover, in both events a lithospheric activation (caused by forthcoming earthquakes) had been already observed. Hence there is a tendency for higher probability of large oil slicks during the periods of lithospheric activation in the region. This may be due to breaking of oil pipelines built in the fracture area of the Apsheron.

Figure 36 (central) illustrates the map of lithosphere fractures and earthquakes zones in the Caspian Region and two AVHRR/NOAA images in which specific lined clouds (marking the lithospheric active fractures) are outlined for both discussed events, Fig. 36 (left and right). It should be noted that the specific lined clouds are largely composed of water-free aerosols. These clouds (and areas around of them) exhibit near-null differences in radiation temperatures at 11 and

12 μm wavelength. So a possibility of early earthquake signs detection and using this data for large sea surface oil pollution forecasting near to the Apsheron is offered.

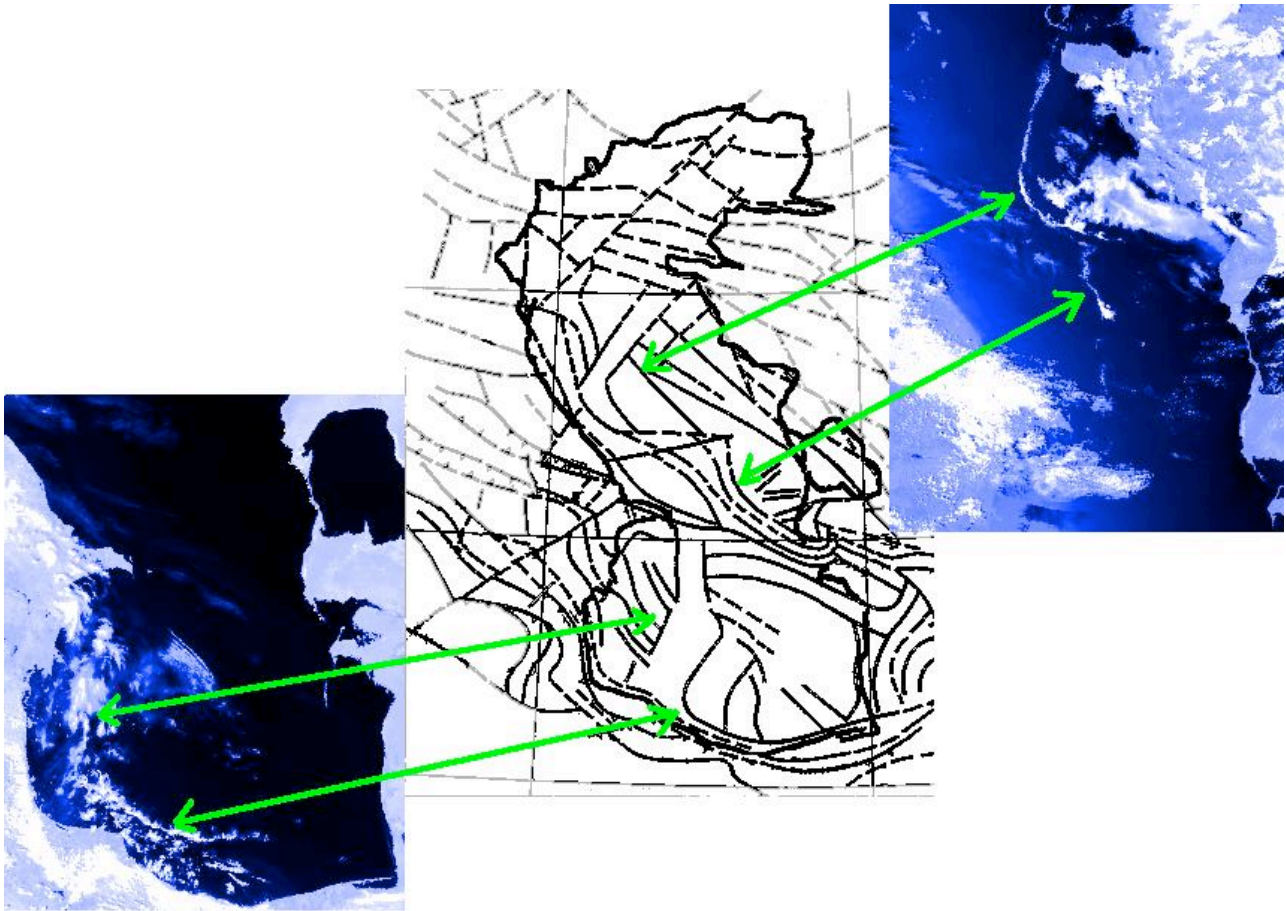


Figure 36. Central - map of lithosphere fractures and earthquakes zones in the Caspian Region. Left and right - AVHRR/NOAA images with specific lined clouds marking the lithospheric active fractures

It is not supposed that all large oil pollutions of sea surface near to the Apsheron result from lithospheric activation solely. Earlier the NTs OMZ mid-term report presented the analysis results of another event involving the detection of large oil pollution near to the Apsheron when apparent attributes of lithospheric activation were not observed.

3.1.2 Problems related to the use of remote sensing images

The main problems of the synergetic analysis were due to the following: (1) some observation time discrepancy since the data were from different spacecraft (SAR images from ENVISAT and ERS-2; visible and IR data from NOAA and TERRA), (2) low spatial resolution of IR and thermal data.

The ASAR/ENVISAT and MERIS/ENVISAT data were envisaged to process. With this purpose the detailed specifications for several MERIS/ENVISAT images were formed. However these ordered data were not delivered. The lack of the ordered data influenced essentially on the potentially available remote sensing data analysis results. Of course, it should be emphasized that the MERIS/ENVISAT equipment does not have the IR thermal bands being of fundamental importance for synergetic analysis.

On the basis of the carried out of Kara sea water area analysis the first thematic class (slicks of natural genesis) training samples were generated. A complicated natural slicks configuration has a profound masking effect restricting the capabilities of expert-interpreter when making a final decision on slicks of man-made genesis. Only four events of the Kara Sea surface oil pollution were identified. To generate training set for the second thematic class (slicks of man-made genesis) it is proposed that the data on the Russian southern seas (where oil pollution is easy to detect) should be used. To apply this training information to another natural-climatic region it is required an appropriate correction of signs values using model approximations.

By the example of Caspian sea the complex analysis of the major factors influencing sea surface monitoring is carried out.

Northern Caspian sea monitoring. During the period 1977-1999 an annual oil products inflow with wastewater from Volga to the Caspian Sea was about 70 thousand tons. The rate of the Volga water inflow into the Caspian Sea is governed by the Volgograd hydroelectric power station's operating mode that effects on the hydroecological conditions of the lower Volga and the Northern Caspian Sea. A drastic increase in flush at the end of quarters and after winter holidays results in "anthropogenic" floods when a change in water-level of the Volga delta may be as great as 50 cm. Discharge water tends to increase in evenings causing daily fluctuations of water-level of approximately 10 cm. Peak water discharge gives rise to specific wave structures forming enormous number of slicks that must be taken into account in SAR data analysis.

Winter peak flashes result to that Volga water gets into the sea (under ice) by tens of kilometers farther off the shore than in summer. Ice is formed from fresh Volga water faster than from saltish sea water. Under northern wind a formed ice is removed to those regions where it might never be formed (with no man-made factors) at given hydrometeorological conditions. The coming years will witness the appearance of the Russian LUKOIL oil company's oil derricks in the North Caspian Region. Ice transportation may lead to emergencies at these oil derricks.

Peculiarities of SST anomalies interpretation. At carrying out synergetic analysis SST data are played the important role. The correctness of received results directly depend on some key problems. One of them is satellite and contact SST maps satellite discrepancy which is caused, first of all, by information horizons discrepancy (water layers depth). It is shown, that after the correct account of insolation and wind-induced water hashing satellite SST maps become similar to contact SST maps.

At slicks genesis analysis carrying out the World ocean chlorophyll concentration spatial distribution information is used. This satellite information is placed on the NASA site for many years. The results of the carried out detailed analysis of a chlorophyll concentration composite map (for the period from 29.08.2001 on 05.09.2001) have shown, that the placed there information is not indisputable, and its use demands the certain care.

3.1.3 Main achievements

A synergetic analysis of data on the south-eastern part of Barents Sea was carried out where the Russian oil company LUKOIL drilling activity takes place. Because of a high cloudiness probability in the northern latitudes there were selected only 3 Events (Event 1 – the Pechora bay, Events 2 and 3 – a water area to south-west from Vaigach Island); the data from two SAR surveys of this region under cloudiness (synergetic analysis was not carried out) were analyzed in addition.

As an example below the images (and results of their processing) are given for the southern Vaigach Island and adjacent area (observation is carried out on August, 2; Event 2). The genesis of slicks to north and to south from Yugorskiy Shar Passage was analyzed (see ASAR/ENVISAT image and 2 fragments, Fig.37). The wind speed data are shown in Fig 38.

When analyzing general situation the MODIS/TERRA image (Fig.39 left) and the standard maps of solar radiation albedo at $0.8\mu\text{m}$ in % and of radiation temperature at $11\mu\text{m}$ in $^{\circ}\text{C}$ (based on AVHRR/NOAA data, Fig.39 central) were using as a rule. Vaigach Island is marked by red arrow.

At carrying out synergetic analysis based on the AVHRR/NOAA data there were generated usually cartographic products of three types, the examples of which are given in Fig.40, namely: a precision map of backscattered solar radiation albedo at $0.8\mu\text{m}$ in %, a SST map in $^{\circ}\text{C}$, and a hydrosol albedo map at $0.6\mu\text{m}$ in %.

Besides the chlorophyll concentration maps (based on the MODIS/AQUA/TERRA and SEAWIFS/SEASTAR data) were analyzed and a SST map (based on the MODIS/AQUA/TERRA data) was analyzed as well, Fig.41

On the basis of the carried out researches a natural genesis of the observed slicks (to north and to south from Yugorskiy Shar Passage) was shown.

Similar results were emerged from analyzing other Events. Signs of sea surface oil pollution were not detected. It may attest that ecological and technical safety of the Russian LUKOIL company's drilling works is rather efficient.

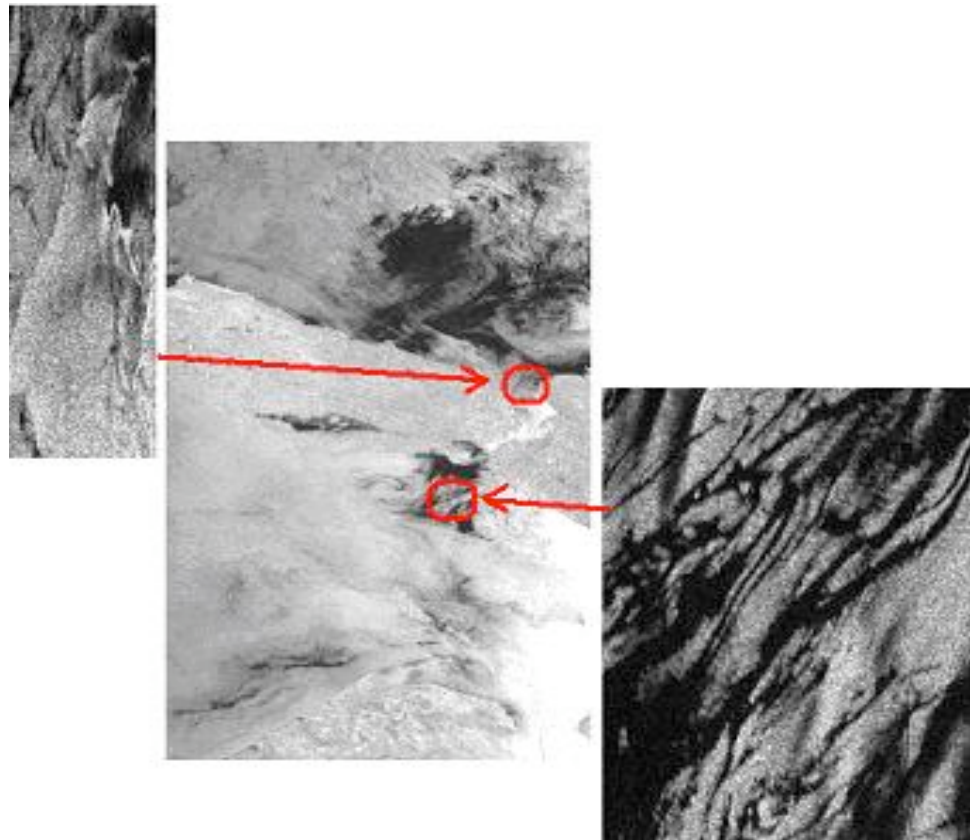


Figure 37: Middle: ASAR/ENVISAT image of the South Vaigach Island. Left and right – enlarged images of slicks to north and to south from Yugorskiy Shar Passage.

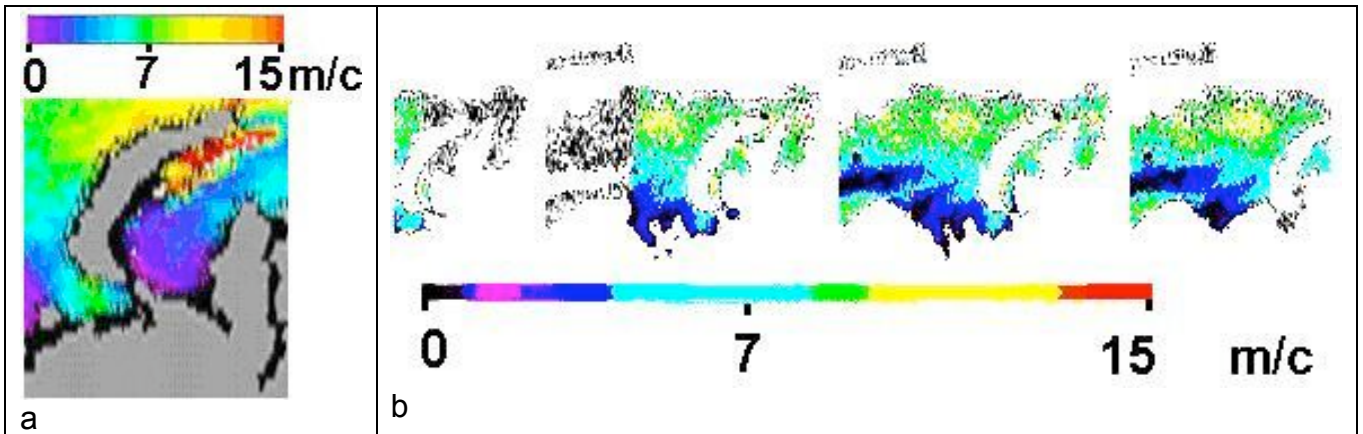


Figure 38: Wind speed data.

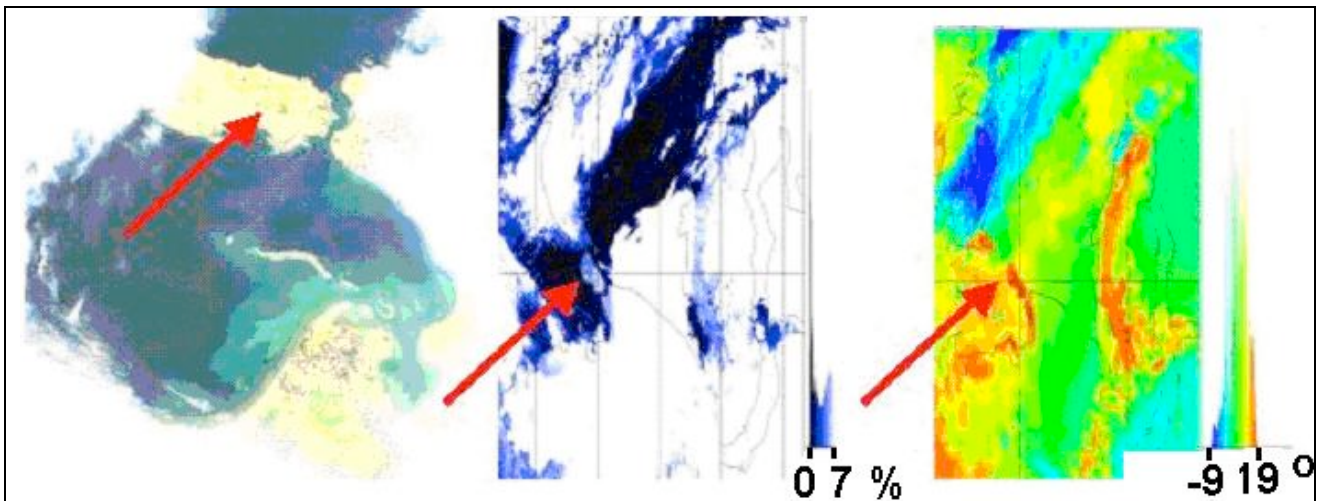


Figure 39: Left - MODIS/TERRA images. Central and right – standard maps of solar radiation albedo at 0.8µm in % and of radiation temperature at 11µm in °C (based on AVHRR/NOAA data).

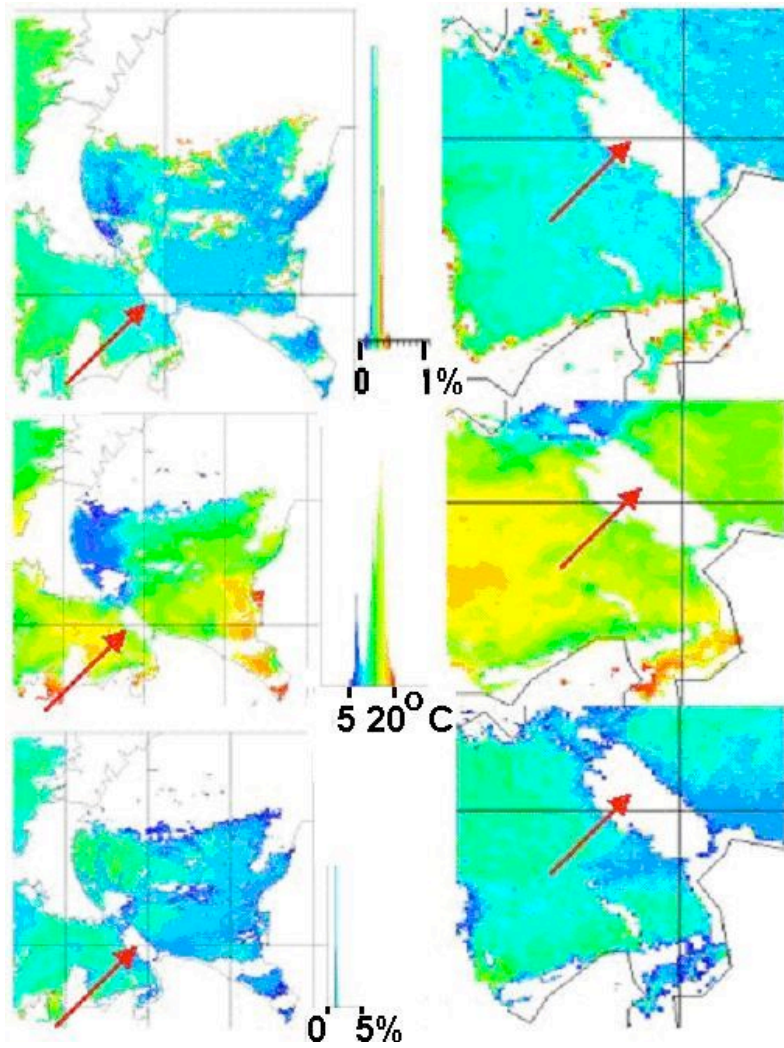


Figure 40. Upper row – a precision map of backscattered solar radiation albedo at 0.8 μm in %. Middle row – a SST map in °C. Lower row – a hydrosol albedo map at 0.6 μm in %. Right – Vaigach Island region enlarged fragments; Vaigach Island is marked by red arrow.

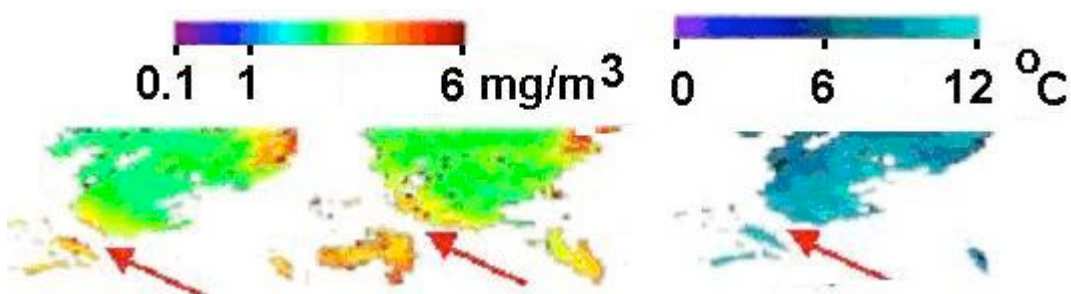


Figure 41: Chlorophyll concentration maps at the south-east part of Barents Sea based on the MODIS/AQUA/TERRA data (left) and SEAWIFS/SEASTAR data (central); right - SST map based on the MODIS/AQUA/TERRA data. Vaigach Island is outlined by red arrow.

The analysis of several events near to the navigational routes (Gulf of Ob, Baidaratskaya Gulf) connected to the complicated interactions between tidal, wind-induced and anemobaric waves was performed. The SAR data were acquired under continuous cloudiness; supplementary data were entirely unavailable (except for wind speed data).

Figure 42 illustrates the ASAR/ENVISAT images of Gulf of Ob; dates of observation are 12, 28 and 31 July 2004. Surface wind speed was 4-12 m/s that exceeds the threshold values (3 m/s) required for formation of calm slicks at water surface, nevertheless, slick on sea surface are observed everywhere.

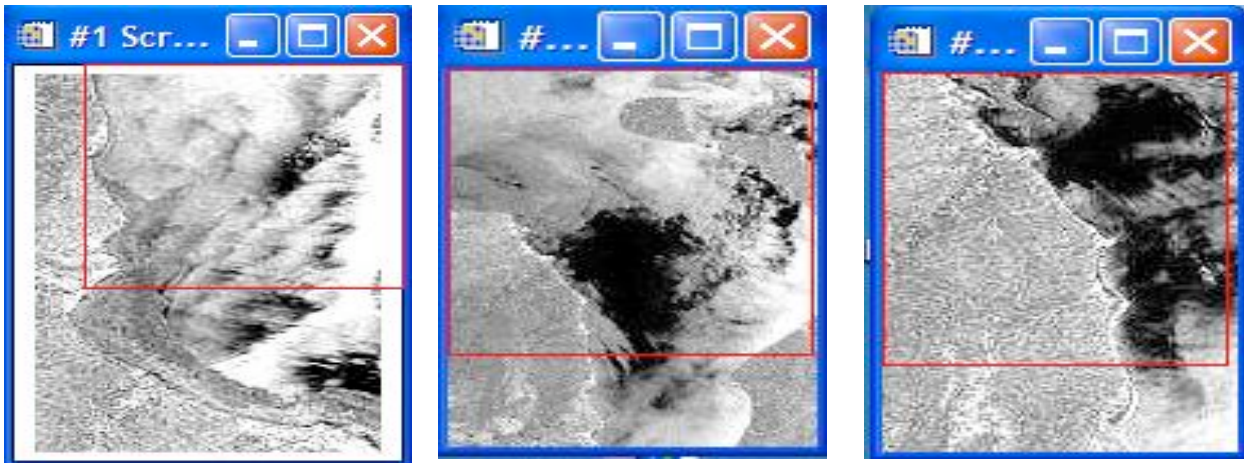


Figure 42: ASAR/ENVISAT images of the Gulf of Ob; dates of observation are 12, 28 and 31 July 2004

Other special features of sea surface image structure may be seen in the ASAR/ENVISAT images of Baidaratskaya Gulf; dates of observation are 21 and 24 July 2004, Fig.43.

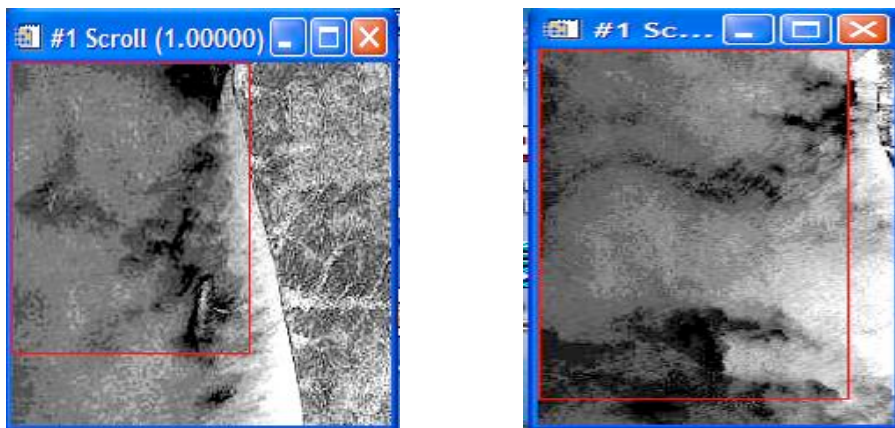


Figure 43: ASAR/ENVISAT images of Baidaratskaya Gulf; dates of observation are 21 and 24 July 2004

Notice once again that natural slicks of complicated configuration observed at sea surface have a profound masking effect that restricts drastically the capabilities of expert appraisal.

With the purpose of improving the efficiency of the Kara Sea oil pollution monitoring the NTs OMZ started to develop the approach based on simplified heuristic algorithms. These algorithms are based on the analysis of two-dimensional scattering plots with emphasis on analysis of slick boundary area. The advantage of this approach is the ability of the produced procedures functioning when using a limited volume of training data that is of especial importance for the Kara Sea region. Besides the two-dimensional scattering plots constructed by these procedures enable an expert-interpreter to interpret the obtained results in operation mode.

The classification results will be the important ancillary data to be used by an expert-interpreter when analyzing complicated events.

Three SLR images of the Kara Sea from the NTs OMZ's archive were analyzed (orbit 0425; date of observation is 9.11.94, orbit 8183; date of observation is 19.04.96, orbit 13517; date of observation is 1.01.97). These images contained areas of darkening. The signs of sea surface oil pollution have not been detected. Figure 44 exemplifies the SLR image (a fragment of orbit 0425; date of observation is 9.11.94) and SAR/ERS image (date of observation is 10.11.94). An ice field which was removed (drift) by wind to Novaya Zemlya over the period from 9 November to 10 November is marked by red arrows.

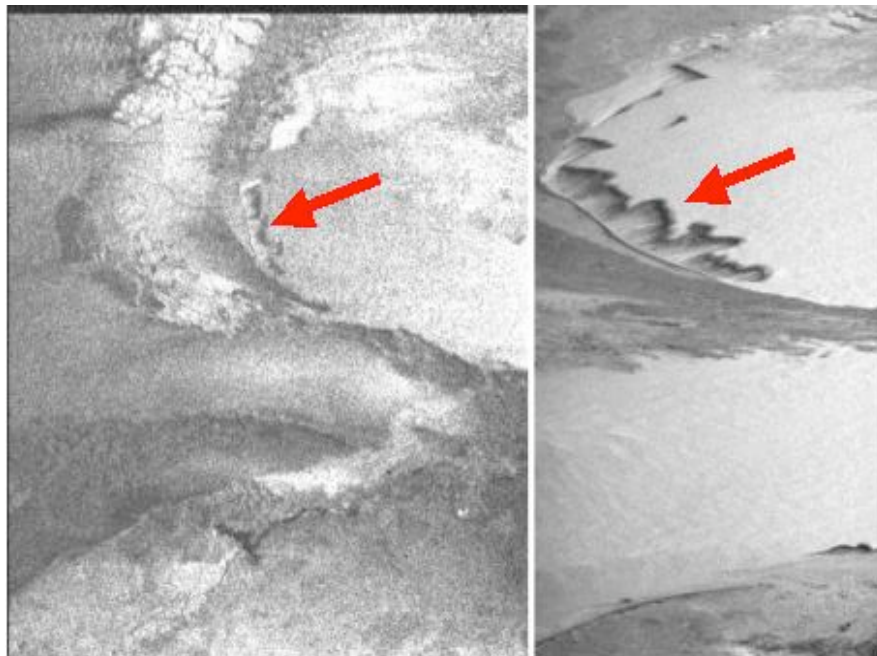


Figure 44: Left - SLR image; fragment of orbit 0425; date of observation is 9.11.94. Right - SAR/ERS-1 image; date of observation is 10.11.94

The software for SLR/SICH-1M data processing was upgraded. The following two procedures were created additionally: (1) the procedure of changing to absolute values of radar reflectance and (2) the procedure of geometric correction and changing to one of three projections. There was obtained only one SLR/SICH-1M image. Date of observation is 23 March 2004. This SLR/SICH-1M image was processed, Fig. 45.

A signal from sea surface (two fragments – at the beginning (2) and at the end (3) of scan line) was not distinguished from the SLR/SICH-1M receiver noise (fragment 1). The SICH-1M spacecraft ceased to be effective on 8 August 2005.

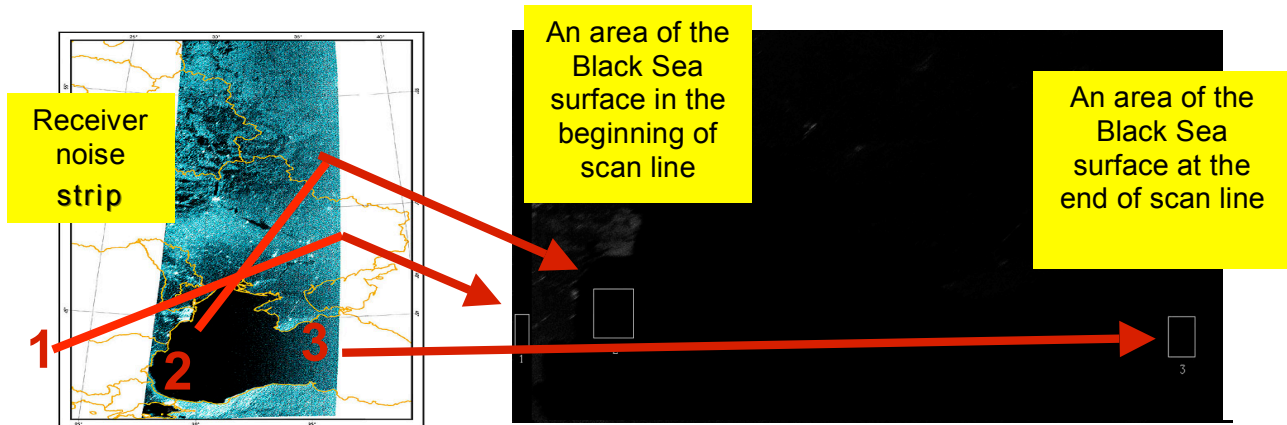


Figure 45: SLR/SICH-1M image processing results. Date of observation is 23 March 2004.

Task 3.2 Satellite image analysis for the Black Sea

Task leader: Marine Hydrophysical Institute

3.2.1 Introduction to oil spill monitoring in the Black Sea

Oil pollution risk in the Black sea is linked to intensive ship routes, large ports, oil platforms. The main problem of environmental control in this region is the absence of regular observing systems and lack of information about real pollution situation. Since 'look-alikes' expressed in SAR have the same sizes, shapes, radar contrasts [Calabresi *et al.* 1999] it makes difficulties to identify oil spills. At present time there are no reliable algorithms allowing to distinguish dark spots in SAR images due to surface films from radar contrasts caused by dynamic effects, e.g. convergent current [Johannessen *et al.*, 2005, Grodsky *et al.*, 1992], ocean temperature fronts [Beal *et al.*, 1997, Kudryavtsev *et al.*, 1999], wind heterogeneity. Using simultaneous observations of rain cells by the ERS SAR and weather radars Melsheimer *et al.*, [2001] found that rainfall might cause both decrease and increase backscattering and expresses in radar image as film slick. Radar contrast from slick and 'look-alike' lie in wide range 0.6-20.6 dB [Espedal, 1998a] and have close geometrical characteristics as such as area, perimeter length, shape [Calabresi, 1999; Frate, 2004].

The task of recognition of surface films in SAR images is not trivial now. For the purpose of oil spill identification auxiliary meteorological and hydrological data are analysed [Espedal, Wahl, 1999], the statistical methods of the image [Solberg, *et al.*, 1999] processing are used, the specific features of film imagination in radar signal are taken into account [Espedal *et al.* 1998b; Calabresi, 1999, Frate, 2004]. To raise reliability of detection oil pollution in SAR simultaneous multifrequency and multipolarization measurements can be applied [Gade *et al.*, 1988].

As follows from foregoing the problem of surface film identification in radar data is difficult enough and requires:

- using different additional information including sea surface temperature (SST), atmosphere temperature, wind;
- study of radar backscattering from sea surface covered with film

Within the OSCSAR Project these problems were solved to assess of oil spill pollution in the Black Sea using ERS and ENVISAT SAR images.

3.2.2 Compilation data sets for the Black Sea

The base information to find out surface films was 44 high resolution SAR images for period 2003 – 2004 and 24 Wide swath SAR images for 2005 placed at our disposal by European Space Agency within ESA-IAF GMES networking with Russia and Ukraine (Project OSCSAR). High resolution images include 25 SAR ERS-2 scenes and 19 ASAR ENVISAT scenes. Schemas of covering the Black sea with ASAR are shown in Fig. 46a and b.

In order to identify oil films it has been compiled obtained SAR/ASAR set and *in situ* data in the Black Sea region. The data set contains QuickScat wind speed on 0.25 x 0.25 deg. grid twice a day from 1999 to present, sea surface temperature obtained with NOAA satellites 4-5 times a day from 1996 to present, daily mean 2 m air temperature from 1996 to present, SICH-1 radar images.

Used available sources:

- <http://poet.jpl.nasa.gov/> (wind vectors);
- <http://www5.ncdc.noaa.gov/> (air temperature);
- MHI HRPT satellite receiving station (sea surface temperature);
- MHI archive (91 SICH-1 images of the Black sea during 1996)

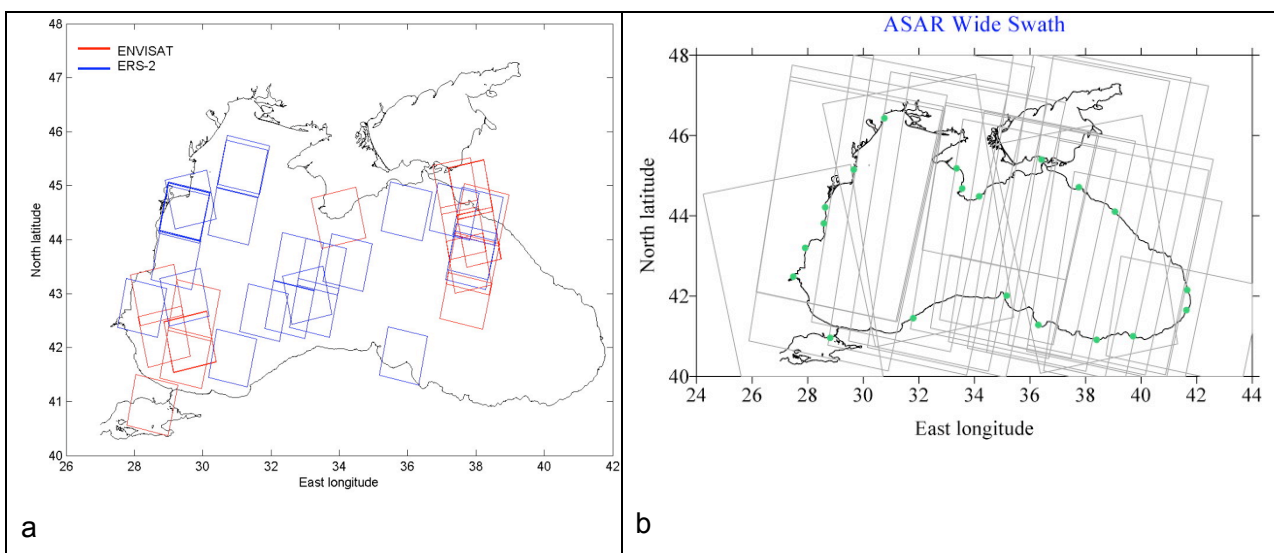


Figure 46. (a) High resolution ENVISAT ASAR scenes used to identify oil spills in the Black Sea, (b) Wide swath ENVISAT ASAR scenes used to identify oil spills in the Black Sea.

The Black Sea is characterised by complicated dynamic and essentially heterogeneous field of surface temperature (see e.g. *Ginzburg et al.*, 2000). Absolute temperature maps with spatial resolution 1x1 km² reduced with NOAA Advanced Very-High Resolution Radiometer (AVHRR) infrared images received on Marine hydrophysical institute station were used to analyse sea dynamic within SAR scenes. Sea surface temperature was calculated using NOAA standard method. Temporal differences between SAR observations and NOAA data did not exceed 1.5-2 hours. Example of SST map on 05 June 2005 is illustrated in Fig. 47. Black areas in the North and South-west of the Black Sea are the clouds.

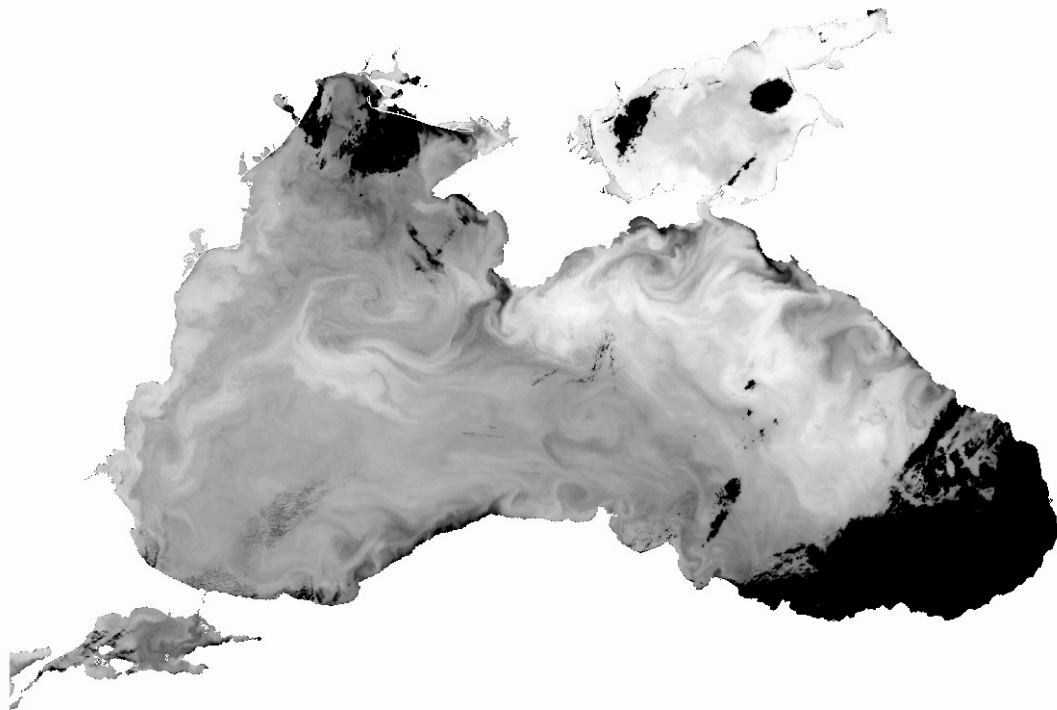


Figure 47. Example of SST map retrieval with NOAA AVHRR from 05 June 2005 (02:59:25 GMT). Black areas in the North and South-west of the Black Sea are the clouds.

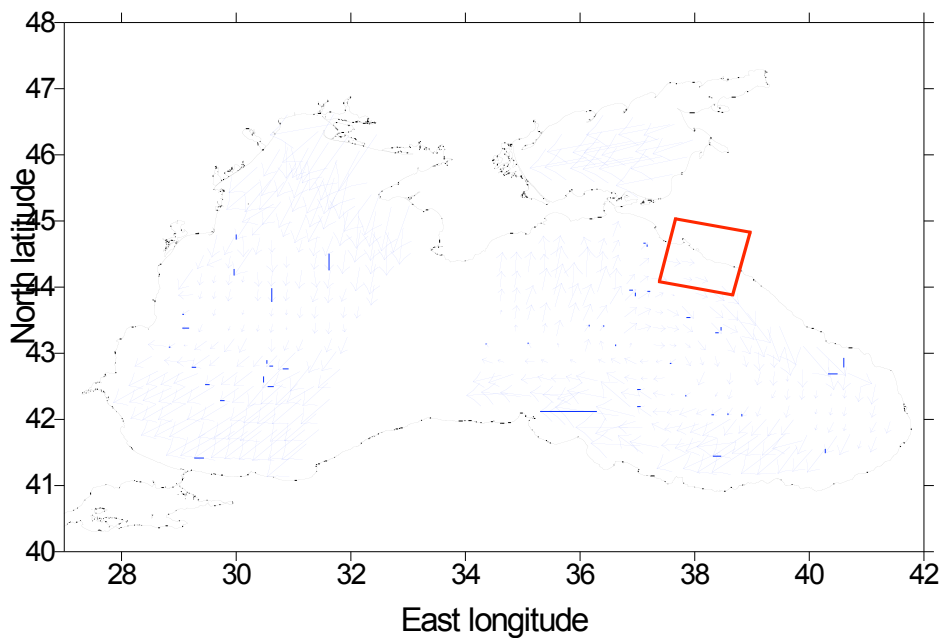


Figure 48. QuickScat wind speed from 01 Aug 2003. ASAR scene is marked by red

The wind situation at corresponding to SAR term was realised with QuickScat scatterometer data on grid $0.25^{\circ} \times 0.25^{\circ}$ obtained from PO.DAAC site (PODAAC Product #109 <http://podaac-esip.jpl.nasa.gov/poet/>). QuickScat wind speed on 01 Aug 2003 is shown in Fig. 48 where ASAR frame is marked by red.

Wind speed U over a period of 1999 – 2004 was analysed on purpose to estimate its statistic. Normalised histogram $p(U)$ of wind module U is shown in Fig. 49 where normalisation was done on total number of data (527597) with argument step 1 m/s. It let us to consider $p(U)$ as probability density of variation U . Dotted line in Fig. 49 corresponds to Weibull distribution

$$p(U) = \lambda \cdot a \cdot U^{a-1} \cdot \exp(-\lambda \cdot U^a)$$

where values of parameters $\lambda = 0.02741$ and $a = 1.884$ were obtained with the least squares method. As it follows from Fig. 49 percentage of wind lower 5 m/s is 49% and for $U \leq 7$ m/s this quantity is equal 71%. Therefore weak and moderate winds are typical for the Black Sea.

These conditions are appropriate to form surfactants films and their existence for a long time [Hühnerfuss et al., 1977].

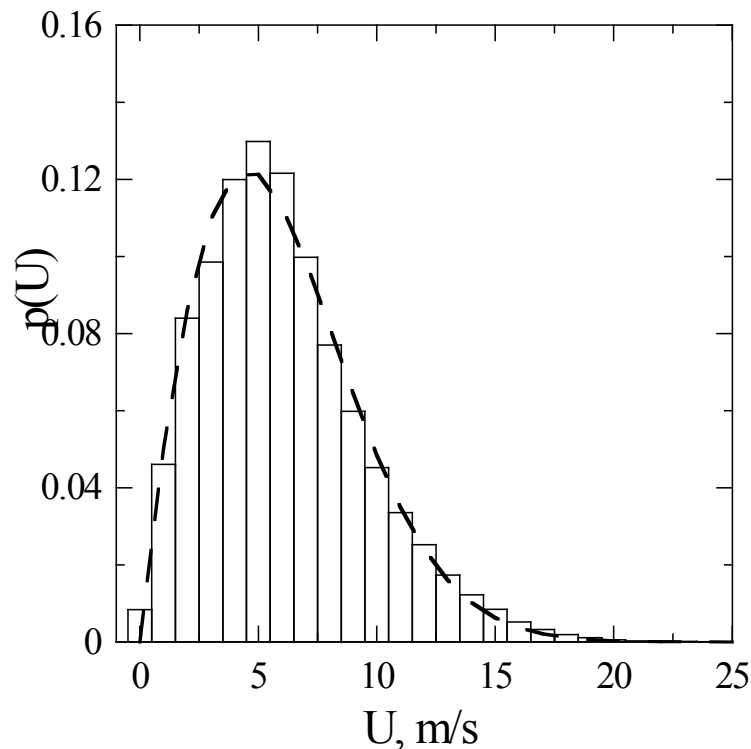


Figure 49. Normalised histogram $p(U)$ of wind module U in the Black Sea

Air temperature T_a at 2 m measured on WMO meteorological observing stations was obtained from National Climatic Data Center (NCDC) site. These data were used to interpolate temperature field over the Black Sea.

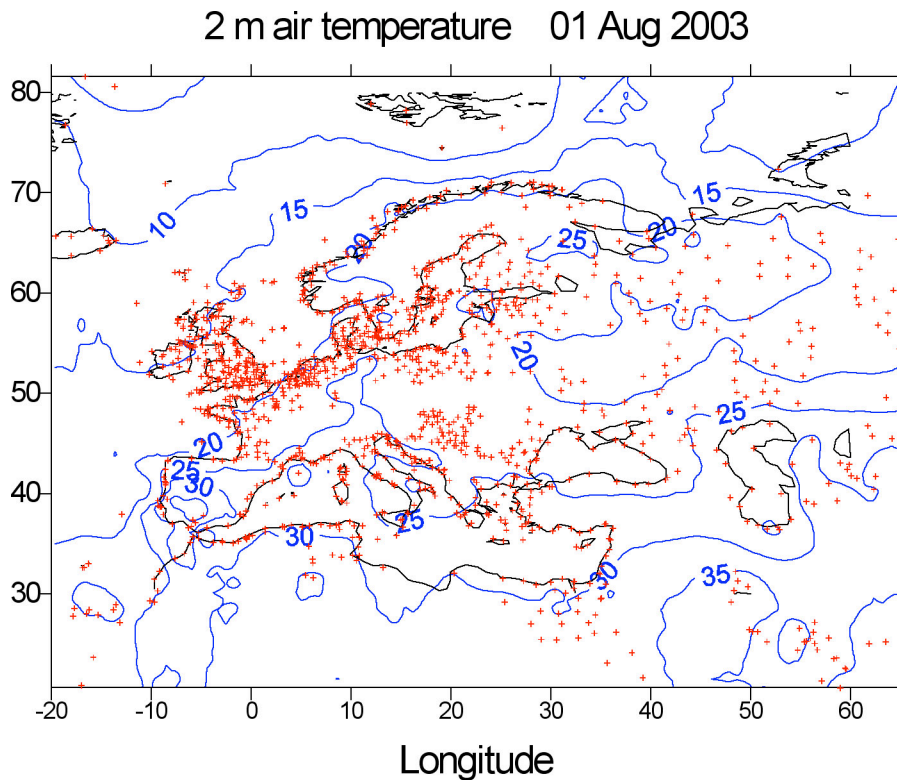


Figure 50. Air temperature at 2 m height. Blue curves are isotherms, red pluses – locations of meteorological observing stations.

Only stations with elevation below 150 m were picked out to calculate temperature fields. Example is illustrated in Fig. 50 where blue solid lines correspond isotherms and red pluses are station locations. Wind, SST, air temperature data set selected by MHI team supplementing ASAR ERS and ENVISAT is available via <http://www.niersc.spb.ru/oscsar>.

3.2.3 Analysis of SAR images in the Black Sea

In the broad sense both anthropogenic contamination and surfactant might be appreciate as 'pollution'. In the frame of this paper first of all we are interested in films most probably formed due to oil platform functioning, ship spills, industrial activity in coastal zones. During SAR image analysis algorithms indicated above were used to identify surface films. Example of imagination in radar image dynamic effects is illustrated in Fig. 51 where SAR ERS-2 fragment (5 Oct 2001, 08:15 GMT) of North-east part of Black sea is shown. Spatial distribution of normalized radar cross section (NRCS) σ^0 within image is essentially heterogeneous. In the east part of fragment frontier directed on north-west is clear observed. There is large area of depressed σ^0 to East of this frontier and zone of increased backscattering with numerous small-scale dark structures is watched in the west part of fragment.

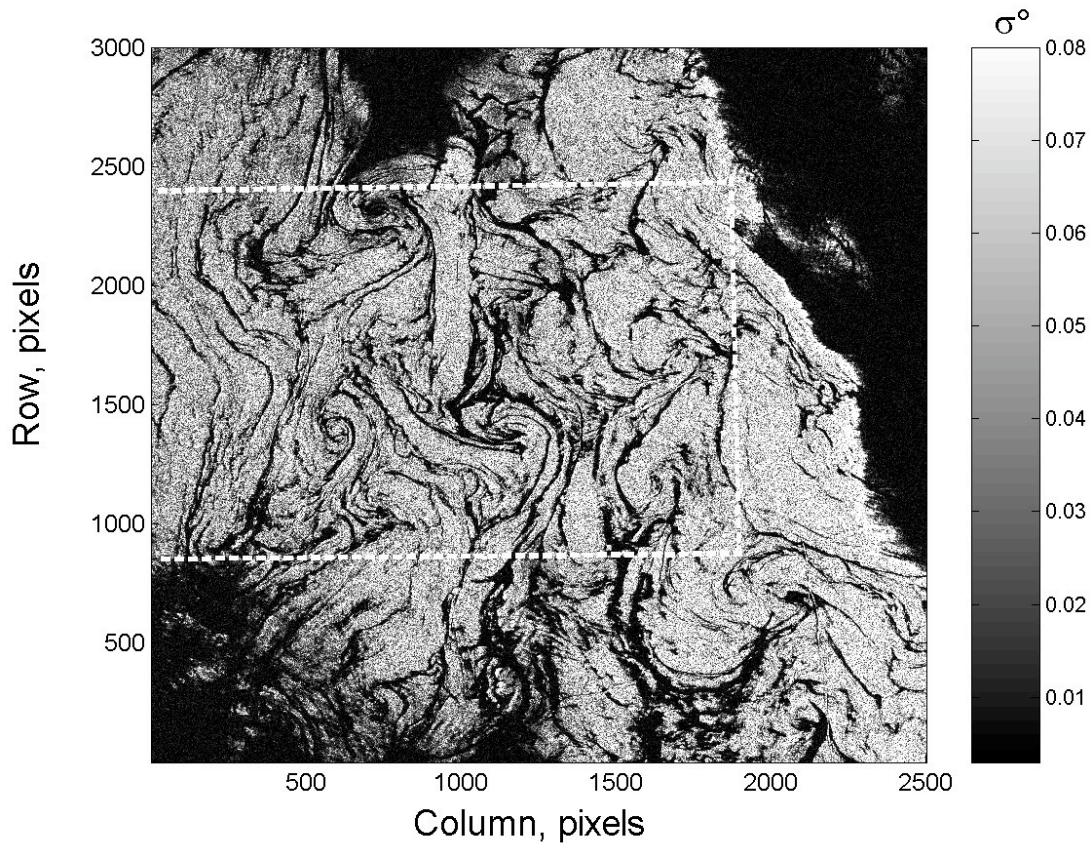


Figure 51. Example of current convergence imagination in fragment of SAR from 01 October 2001.

Wind in this region shown in Fig. 52 by arrows was North-western 330° with mean speed 4.9 m/s. Surface temperature obtained on 5 Oct 2001 at 08:21 GMT is illustrated in Fig. 53 where the scale of absolute temperature in $^\circ\text{C}$ is located on the right of image. Here and below on NOAA images and wind maps quadrangle indicates location of total SAR scene. As it follows from Fig.4 noted frontier in SAR corresponds to front with temperature difference $2^\circ\text{C} - 3^\circ\text{C}$.

Large dark area in SAR (Fig. 51) to the East of the front is concerned with decrease of σ^0 because of modification of atmosphere boundary layer above cold side of frontal zone [Kudryavtsev et al., 1996]. Narrow dark structures on the warm (west) part of the front might be interpret as imagination of current surface current convergence [Grotsky et al., 1992, Johannessen et al., 2005] where surfactant are concentrated. Let designate radar contrast as

$$K = 10 \cdot \log(\langle \sigma_{sl}^0 \rangle / \sigma_b^0)$$

where σ_{sl}^0 and σ_b^0 are NRCS in slick and clean water respectively, symbol $\langle \dots \rangle$ denote data averaging. In area in Fig. 51 limited by light dotted line value of K calculated for numbers of SAR pixels within slick $N_0 = 526294$ is 8.4 dB.

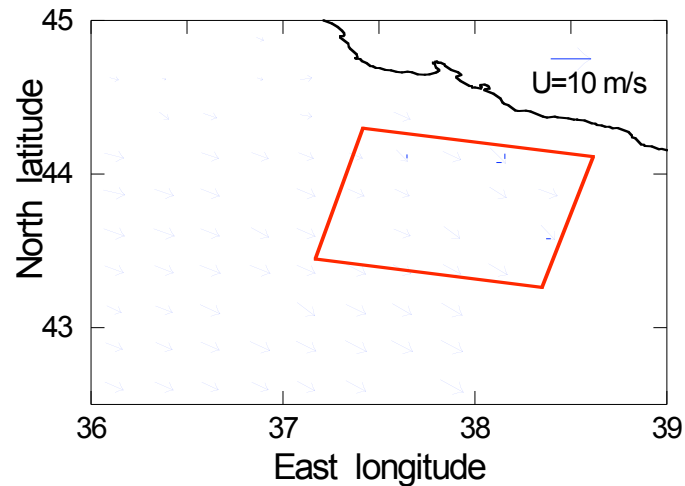


Figure 52. QuickScat wind from 01 October 2001. Red lines limit to SAR scene.

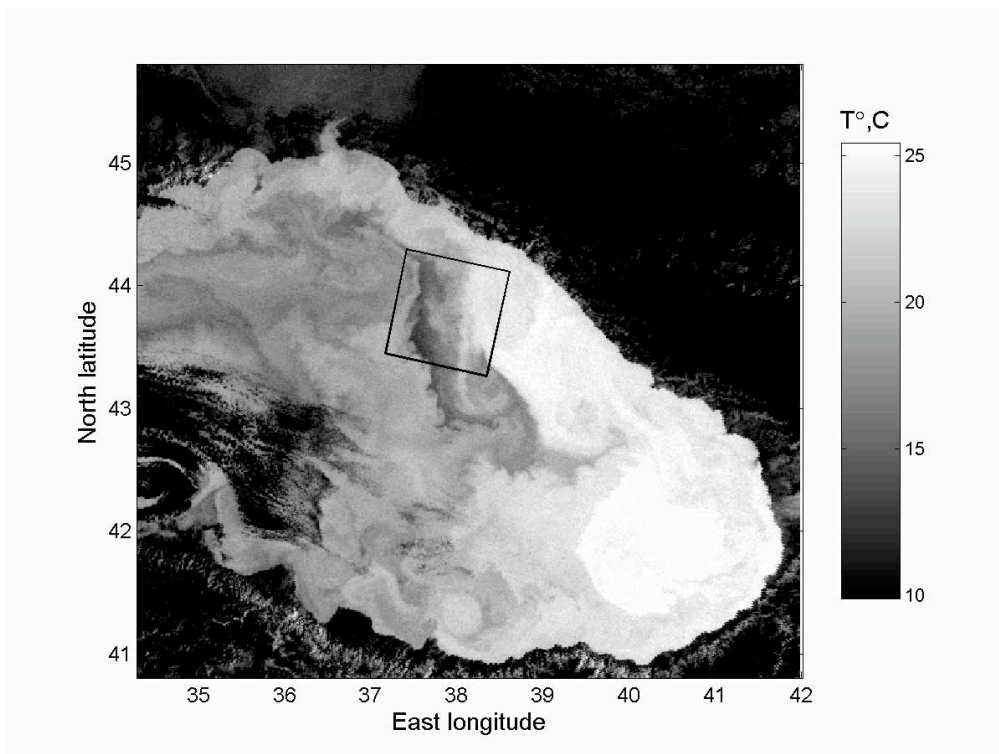


Figure 53. Sea surface temperature from 01 October 2001

Let examine some peculiarities of backscattering concerned with spills from ships. Fragment of ERS-2 SAR (03 Aug 2004, 08:49 GMT) is shown in Fig. 54 where the NRCS scale is cited on the right of image. The dark area with size about 3 km located behind the ship which is indicated as bright spot with coordinate in pixels $x = 3266$, $y = 3624$ (geographical coordinates are 44.569N/29.373E). Wind in this region was South-western with speed 7.6 m/s. Sea surface temperature was spatially homogeneous. Radar contrast calculated using 7461 pixels within dark area is 5.7 dB. Peculiarity of spatial distribution of σ_{sl}^0 is illustrated in Fig. 55 where axis of abscissas and ordinates agree with numbers of column and row of original SAR scene. Here

vertical axis corresponds to $1/\sigma_{sl}^0$ for better visualization. Close to ship values of $1/\sigma_{sl}^0$ are the largest (the smallest NRCS) and decrease (NRCS increase) with moving away from the ship. One of the reason of such effect might be spilling process when the surface concentration of pollution is larger near the source and diminish on distance due to spreading.

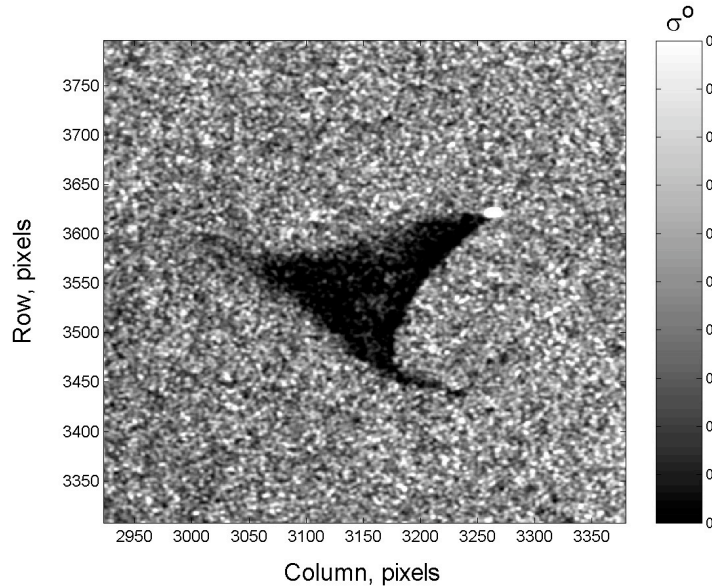


Figure 54. Fragment of ERS-2 SAR from 03 Aug 2004, 08:49 GMT

One of the most polluted area is placement of the oil platform in the West part of the Black Sea. Fragments of ERS-2 SAR scenes from 06 Jul 1999, 25 Jul 1999 and 13 Mar 2004 are demonstrated in Figure 56 a, b and c. The platforms are visible as bright spots and lengthy dark zones are probable contamination. Wind speed, its direction and radar contrast were 2.6 m/s, 10°, 7 dB; 4 m/s, 42°, 9 dB and 1.5-2 m/s, 345°, 8 dB for Figure 52 accordingly. Note that orientations of all shown cases practically agreed with wind directions.

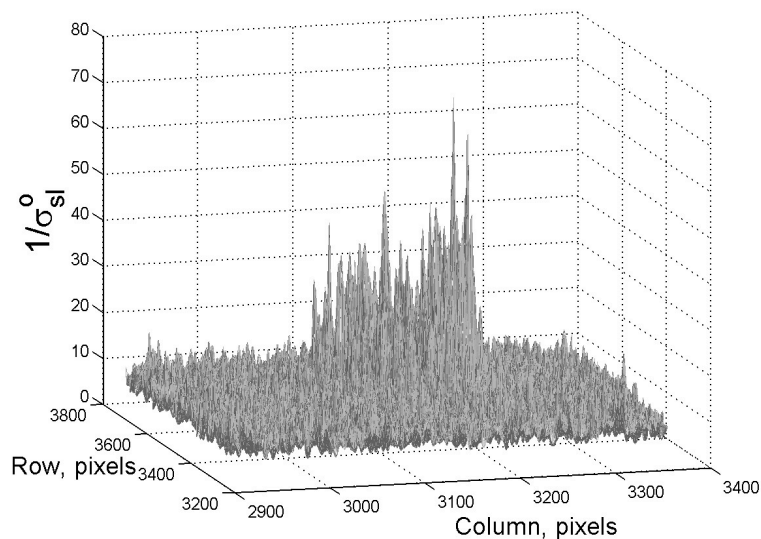


Figure 55. Spatial distribution of σ_{sl}^0 for SAR images shown in Fig.54.

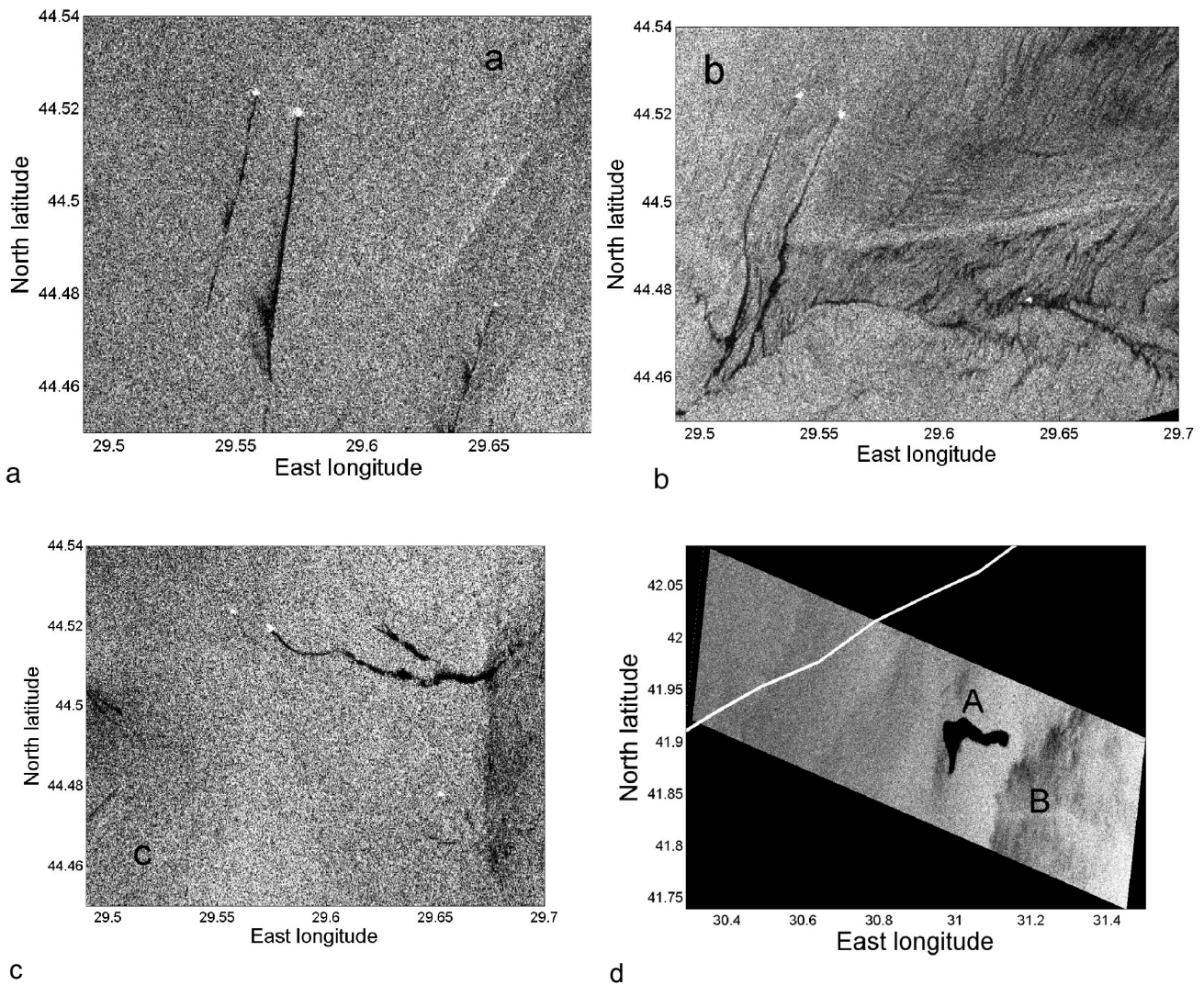


Figure 56. Examples of ERS-2 SAR images of oil spills from (a) 06 Jul 1999, (b) 25 Jul 1999, 13 Mar 2004 (c), and 29 March 2004.

The largest spill identified with ERS-2 SAR from 29 Mar 2004 is illustrated in Fig 56 d. Two features express in the image: dark 'curve' area *A* with 34.7 km² square and to East of it zone *B* with depressed values σ^0 having well observed frontier directed to North-East. There was not dynamic analyses for SAR image time because of continuous cloudiness (visible in NOAA at 08:12 GMT) which covered area to the south of boundary marked in Fig. 56 d by white line. Analysis of this region without clouds with NOAA image (29 Mar 2004 at 19:33 GMT) showed that sea surface temperature had not have spatial features. Wind within SAR scene is demonstrated in Fig. 57 where bold line marks frontier of area *B*. As the Fig. 57 indicates the wind was practically northern and its speed fell to south from 6.5 m/s to 3.1 m/s. Hence reason of depressed radar backscattering in area *B* is the decrease of U . Inside area *A* value of K is 15.7 dB ($N_0 = 192276$). Such great radar contrasts under wind speed more than 3 m/s are observed

apart from oil spills for grease ice and wind sheltering by land [Espedal, 1998a]. It is clear we can except these effects from examination. Radar contrasts appeared due to rain cells are less than in zone A and can vary from 3 dB [Melsheimer, 2001] to 6.7 dB [Espedal, 1998a]. Consequently the most probable reason of appearance area A is spill of oil products.

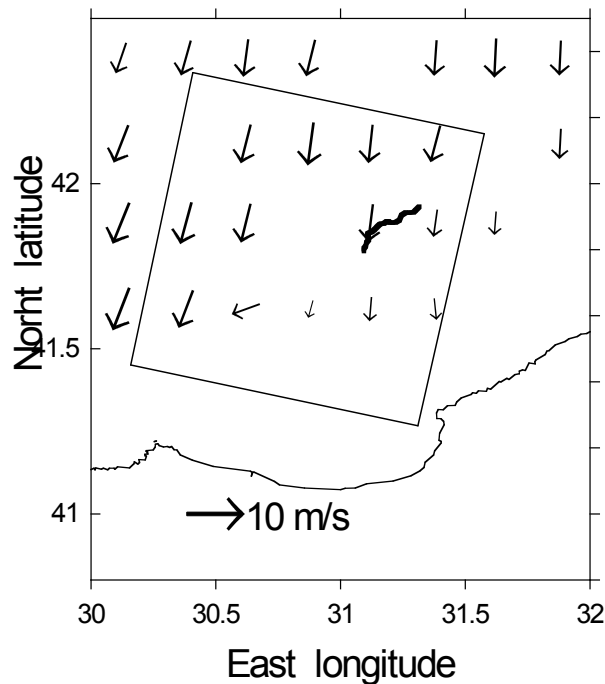


Figure 57. Wind within SAR scene shown in Fig. 56d.

3.2.4 Assessment of oil spill detection in the Black Sea

Examples of surface slick expressions in SAR images examined above demonstrate the problem to identify anthropogenic contaminations in the sea surface. The optimal conditions to analyses appear when there are both 'dark spots' and pollution sources (ships, oil platform, etc) in the image. Generally radar contrasts caused by films and 'look-alikes' are close. There not practically geometrical differences in SAR imagery between oil spills and 'look-alikes' [Calabresi 1999, Frate 2004]. To identify contamination it needs using and analysing of auxiliary hydrological and meteorological data allowing to estimate sea surface dynamic, wind field, rain cells and other.

Spatial heterogeneity of values σ_{sl}^0 demonstrated in Fig. 54 can be additional criterion to determine in SAR oil spill from ship. Moreover for this case histogram of radar backscattering shown in Fig. 58 has peculiarity included increase $N(\sigma_{sl}^0)$ with growth σ_{sl}^0 . Here $N(\sigma_{sl}^0)$ is number of points in selected interval. Such character of σ_{sl}^0 distribution can be explicated by simultaneous radar measurements and contamination spilling. In this case larger radar signal level corresponds to backscattering from surface covered with already spread film with smaller thickness and smaller damping. In the other slicks unrelated to ships distribution of σ_{sl}^0 were almost uniform or narrow. Last case is illustrated in Fig. 58 b where histogram of σ_{sl}^0 in area A in Fig. 51 is shown. Here 94% of total points lie in interval $0.004 \leq \sigma_{sl}^0 \leq 0.008$. In our SAR data six

not wake trails behind ships were found. Distributions of σ_{sl}^0 for these trails are re-united in Fig. 59. To compare data x and y axis correspond to normalised values $\sigma_{sl}^0 / \langle \sigma_{sl}^0 \rangle$ and N / N_0 . Symbols in Fig. 59 designate cases from 03 May 2003 (\diamond и \square), 23 Aug 2003 (\circ и ∇), 23 Sep 2003 ($*$) и 03 Aug 2004 (+). So monotonous growth of σ_{sl}^0 distribution can be one of criteria to identify pollution using SAR images.

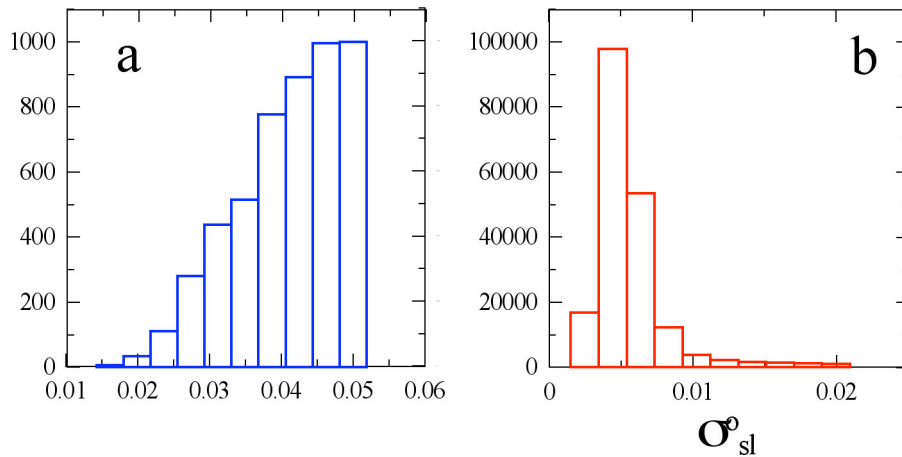


Figure 58. Histograms of radar backscattering for oil spill in Fig.56 (a) and σ_{sl}^0 in area A in Fig.51.

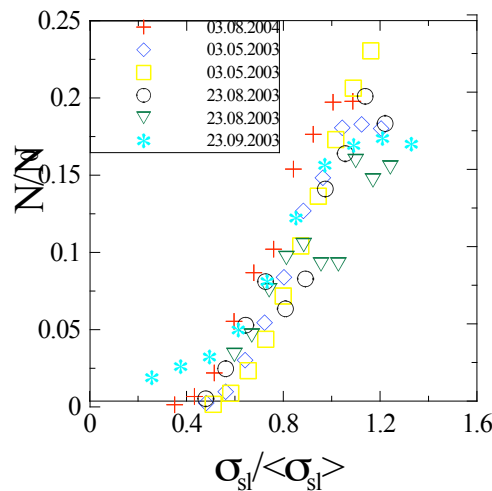


Figure 59. Distributions of σ_{sl}^0 for six cases of spilling from ships

Total number of recognised anthropogenic films with SAR were 92 and their squares S and geographic coordinates of centroids were determined. Distribution of S is essential narrow. Part of films with $S < 1.2 \text{ km}^2$ is 83% and 91% have squares smaller than 3.5 km^2 . Let use results obtained by other authors to provide qualitative analysis with our estimates. *Calabresi et al.* (1999) using SAR images showed that mean statistical ratio between oil spill length and its width lies in limits 4.2 – 11.39. If to accept this value as 10 spill with size 10 km will have square close to 3 km^2 . Analysis of oil pollution in South-East Asia seas carried out by *Lu et al.* (1999) shows that

part of slicks having size smaller than 10 km ($S \sim 3 \text{ km}^2$) is 87%. It in agreement to our results as a whole.

Spatial distribution of recognised film locations is shown in Fig. 60 by symbols (*). Dotted lines in the figure correspond to SAR scenes. Not large number of radar data does not provide statistically valid analysis of obtained results. In our case it may be discussed about main tendencies of pollution in the Black Sea. Nevertheless in Fig. 60 it can be selected next groups of points. First of them is situated in the conventional line Bosphorus – Novorossiisk and coincides with ship routes. Note that in spite of being insufficient SAR covers central part of the Black Sea to North-South direction wider than area of surface film locations. Second group of point lies to the North of Bosphorus and also coincides with ship routes. Two other areas with increased pollution concentration are in the North-Eastern part offshore Novorossiisk and Western part of sea close to oil platform and ports. It needs to take into account that Eastern part of the Black Sea is characterised with complicated dynamic so increased number of slicks can be caused by concentration of films in surface current convergence.

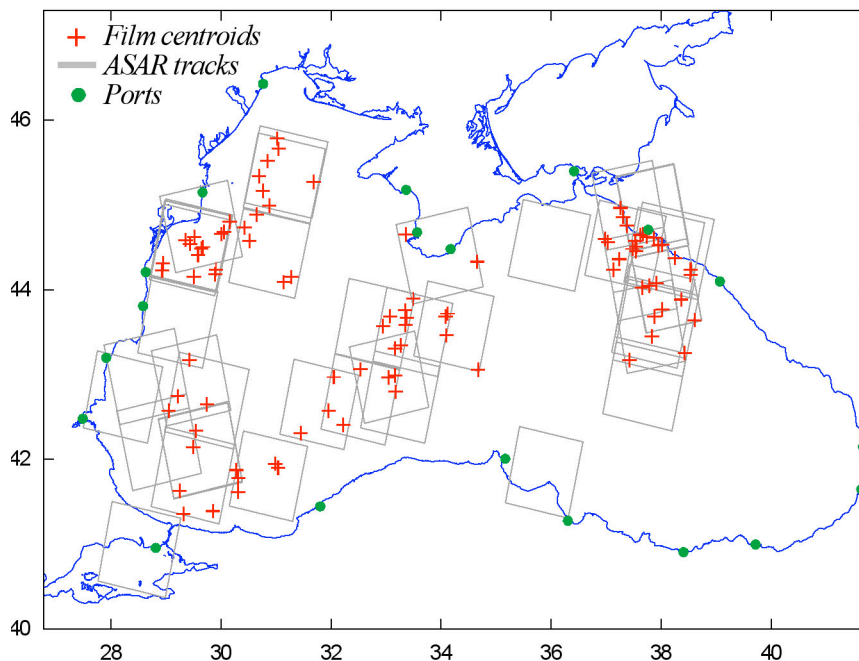


Figure 60. Spatial distribution of oil film manifestation in ASAR imagery for the Black Sea.

3.2.5 Features of radar backscattering from sea surface covered with film

Problems of separating oil spills and “look-alikes” in SAR images require to find additional testing. In frame of the Project the field experiment was carried out to investigate peculiarities of radar backscattering at Ka-band from sea surface covered with film. Take into account that damping of wind waves by films within spectra interval from capillary to gravity-capillary ripple has similar behaviour. In this case it could be expected that the features of backscattering will be also similar at both Ka and C bands but with different values of radar contrasts or some other characteristics.

Experiment was carried out in September 2005 on the MHI oceanographic platform. Wind velocity and sea/air temperatures were recorded in standard meteorological device. Wind waves were measured using wave gauge. Ka-band V and H polarized radar with wavelength $\lambda_r = 8 \cdot 10^{-3}$

(wave number $k_r = 2\pi / \lambda_r$) was used at Incidence angle was 45° . Area illuminated by radar which placed in 13.5 m above the sea surface was 1.5×2 m² and located close to wave gauge.

Vegetable oil was used to create film with size 5×5 m². Oil spill was moved by current through the backscattering area. So registration of radar signal realized in following consequence: clean water – film – clean water. All data were recorded synchronously.

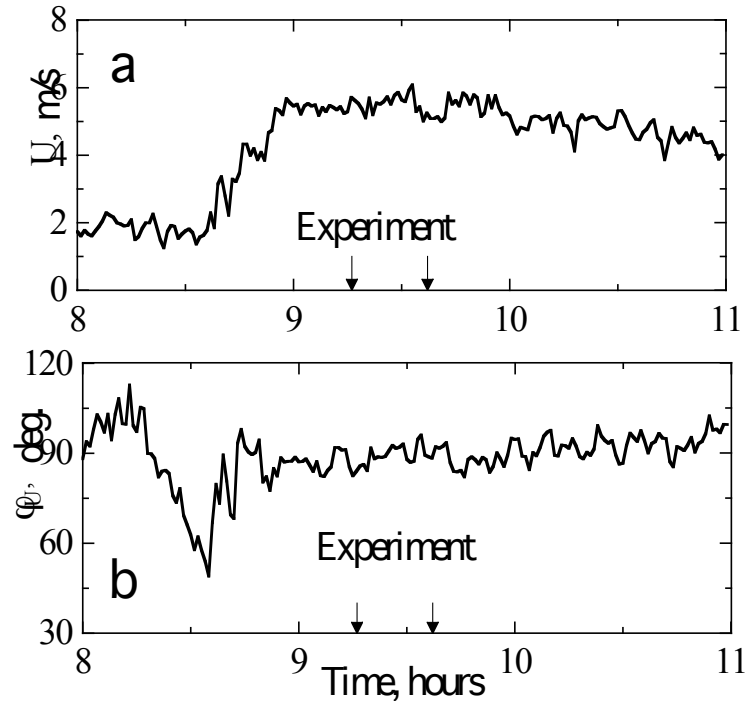


Figure 61. Temporal realization of U and φ_U during field experiment

Measurements were carried out under east wind with mean velocity $\bar{U} = 5.6$ m/s and direction $\varphi_U = 90^\circ$. Temporal realization of U and φ_U are shown in Fig.61. Note that wind speed and direction were practically steady during experiment. Mean square deviation were ± 0.3 m/s for U and $\pm 3^\circ$ for wind direction. Two swell systems with pick frequencies and directions 0.22 Hz, 0° and 0.4 Hz, 250° were observed. Significant wave height was $H_s = 0.35$ m. Temperatures of air and water were 23.5°C and 23.4°C accordingly.

3.2.6 Results of the Black Sea studies

Realization of backscattering at V and H polarizations are illustrated in Fig. 62. Assign radar contrast “clean water – slick” as

$$K^P = \sigma^P / \sigma_s^P$$

where σ^P and σ_s^P - normalized radar cross section (NRCS) for clean water and slick accordingly, P shows on polarization. Values of measured contrasts are $K^v = 2$ and $K^h = 1.5$, so film imagination is more effective at V polarization.

Fig. 63 demonstrates polarization ratio $P = \sigma^v / \sigma^h$. Radar signal realization was smoothed for better visualization. In clean water values of P are close to their model meaning 2.48 [Kudryavtsev et al., 2003] marked by dotted line. In slick P is smaller than in “background “ and equals about 1.8.

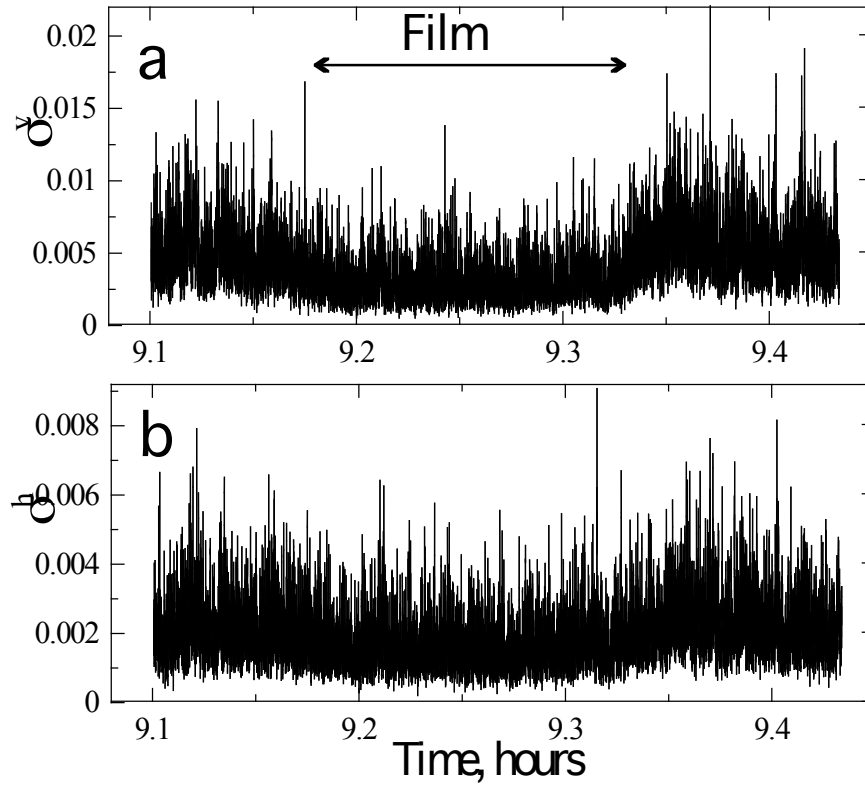


Figure 62. Realization of backscattering at V and H polarizations

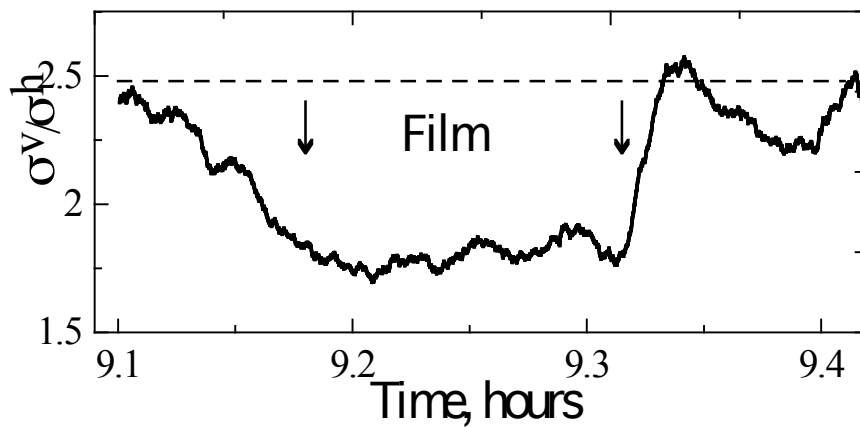


Figure 63. Polarization ratio

Association between amplitudes of long wind wave and variations of NRCS is described by modulation transfer function (MTF)

$$M^P(f) = \frac{S_{\sigma_{\xi\xi}}(f)}{k \cdot \sigma^P \cdot S_{\xi\xi}(f)}$$

where $S_{\sigma\xi}(f)$ - cross-spectrum NRCS and wave fluctuations, $S_{\xi\xi}(f)$ - wave spectrum, f - frequency, k - wave number.

Modules $|M^p(f)|$ and phases $F^p(f)$ of MTF and are shown in Fig. 64 where symbols (*) correspond to clean water conditions and symbols (□) to measurements in slick. Close to spectral picks (0.2 – 0.4 Hz) MTF are practically same. For spectral interval $f > 0.4$ Hz modulation of NRCS by wind waves in slick larger that in clean water in 3 times at V (Fig. 64 a) and in 1.5 times at H (Fig. 64b) polarization. Phase characteristics demonstrated in Fig. 64 c,d show that in clean water maximums of NRCS at $f < 0.6$ Hz located on front side of waves. In slick the same situation is observed at $f \leq 0.4$ Hz. In higher frequencies backscattering maximum shifts on wave crests ($f \approx 0.5$ Hz) and then on back side of wave. The same behavior of $F^v(f)$ was observed in field experiment [Ermakov et al., 2004].

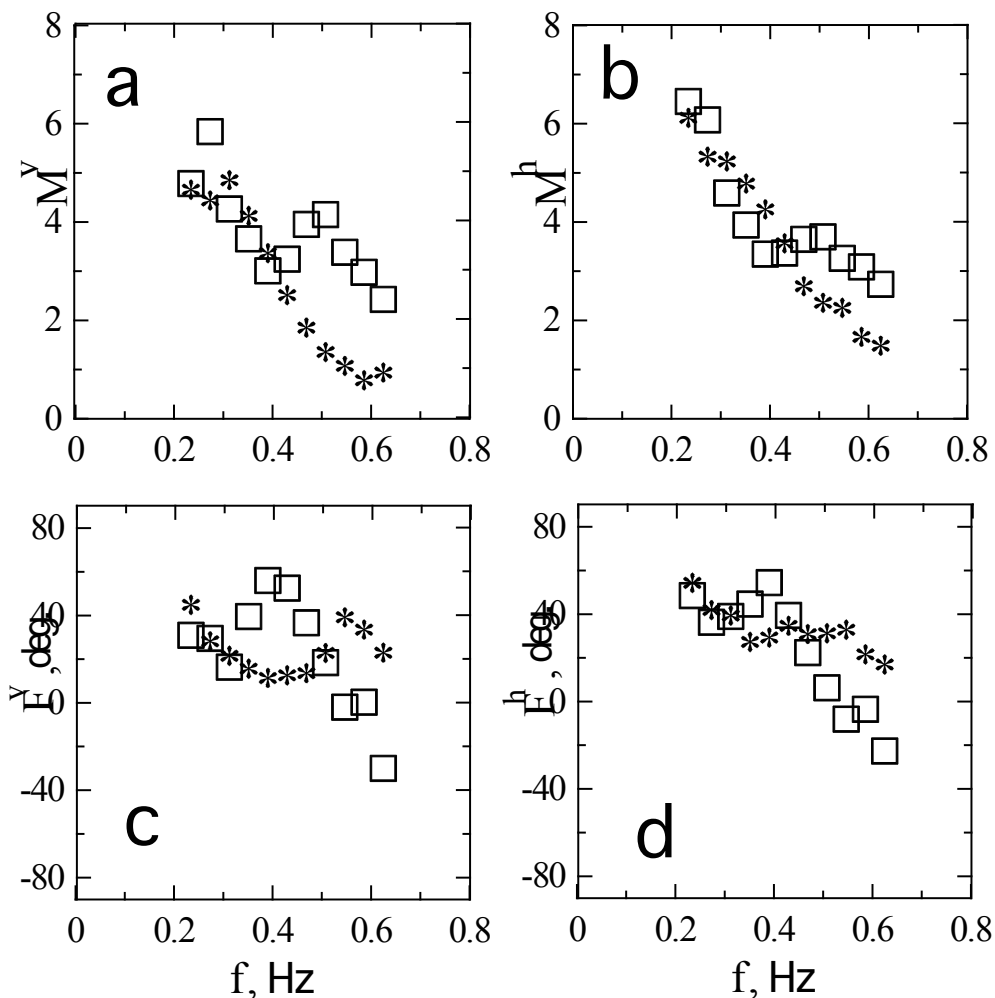


Figure 64. Modules $|M^p(f)|$ and phases $F^p(f)$ of MTF at V and H polarization

3.2.7 Discussion

Assign spectral contrast of wind wave as $K_B = B(k)/B_s(k)$, where $B_s(k)$, $B(k)$ - spectrum levels in slick and clean water. Model values of $1/K_B$ can be found in [Grodsky et al., 1999].

Within two-scale radar backscattering model NRCS can be written as sum of Bragg σ_b^p and non-Bragg σ_{nb} components

$$\sigma^p = \sigma_{0br}^p \cdot \left(1 + j^p \cdot \overline{\xi^2}\right) + \sigma_{nb} \quad (1)$$

$$\sigma_{0br}^p = \pi \cdot \sin^{-4} \theta \cdot G^p(\theta) \cdot B(k_b) \quad (1a)$$

where $k_b = 2 \cdot k_r \cdot \sin \theta$ Bragg wave number, $j^p = 1/(2 \cdot \sigma_{0br}) \cdot \partial^2 \sigma_{0br} / \partial \theta^2$ - geometrical coefficient, $\overline{\xi^2}$ - mean square slope of long waves modulated Bragg ripple, G^p - coefficient depending on incidence angle [Plant, 1986].

The main mechanism responsible for σ_{nb} forming is wave breaking. There we suppose that thin film does not change σ_{nb} i.e. under fixed wind conditions non-bragg component in (1) will be the same on clean water and slick. Taking into account that $\sigma_b^v > \sigma_b^h$ and $\sigma_{nb} = \sigma_{nb}^v = \sigma_{nb}^h$ does not depend from polarization relative contribution of non-bragg component in σ^p at V polarization is larger than at H one. Mean square slope of long wind waves $\overline{\xi^2}$ practically does not change in slick area [Grodsky et al., 1999]. Hence NRCS variations on film depend on variations of "pure Bragg" component (1a) only.

At the same time radar contrast depends on both variation $B(k)$ and ratio between Bragg and non-Bragg components. As it was shown in [Grodsky et al., 1999] contrast of σ_{0br}^p is $K_{0br}^v = K_{0br}^h \sim 5$ for $U = 5.6$ m/s and film elasticity 20 dyn/sm. According in [Grodsky et al., 1999] for background condition contributions of σ_b^p and σ_{nb} in σ^p (1) are

$$q^v = \sigma_{nb} / \sigma^v \approx 0.2, \\ q^h = \sigma_{nb} / \sigma^h \approx 0.5, \quad m^v = \sigma_{0br}^v / \sigma^v \approx 0.68, \quad m^h = \sigma_{0br}^h / \sigma^h \approx 0.37.$$

Using table of symbols describing above it can be written

$$K^v = \left[K_{0br}^v \cdot m^v \cdot \left(1 + j^v \cdot \overline{\xi^2}\right) + q^v \right]^{-1} \quad (2)$$

$$K^h = \left[K_{0br}^h \cdot m^h \cdot \left(1 + j^h \cdot \overline{\xi^2}\right) + q^h \right]^{-1}$$

So model estimations of K_{0br}^v , K_{0br}^h will be $K^v \approx 2.7$ and $K^h \approx 1.5$. Differences in values can be explained by different contributions of σ_{nb} into total NRCS. Hence values of radar contrasts measured in our experiment well agree with model.

Write polarization ratio as

$$P_s = \frac{\sigma^v}{\sigma^h} \cdot \frac{K^h}{K^v}$$

This formula gives model meaning $P_s = 1.4$ which also in agreement with our experimental value.

Analyze of MTF on slick using V polarized radar signal can be found in [Ermakov et al., 2004]

where it was shown that $|M^v(f)|$ in slick is larger than in clean water and phase decreases with decreases of frequency. Our results (Fig. 64) are in agreement with [Ermakov et al., 2004]. Note only that in our experiment data at both V and H polarization were obtained.

The main conclusions can be formulated as

- Radar contrast “film-clean water” is higher at V polarization. This effect can be explained by different contribution of non-Bragg component into total NRCS.
- Polarization ratio decreases in 1.3 times in slick.
- Modulation of radar backscattering by long wind wave is about in 3 times higher at V and 1.5-2 times higher at H polarization in slick than in clean water.

3.3 Dedicated ASAR field experiment in the Black Sea

3.3.1 Introduction and objectives

OSCSAR and National Space Agency of Ukraine supported a field experiment on the MHI oceanographic platform during September 2005. Coordinates of oceanographic tower are 44°23'37" N , 33°59'09" E. ESA provided 5 ASAR ENVISAT high resolution scenes of experiment area from 2 September to 18 September 2005 shown in Table 2. A map of the ASAR scenes location is shown in Fig.65.

Table 2: ASAR ENVISAT scenes used in experiment

#	Date	Time GMT	Polarization
1	02 September 2005	08:06:30.433	V/V V/H
2	02 September 2005	19:25:16.862	V/V V/H
3	05 September 2005	19:30:45.871	V/V V/H
4	15 September 2005	07:57:56.475	V/V V/H
5	18 September 2005	19:22:25.128	H/H H/V

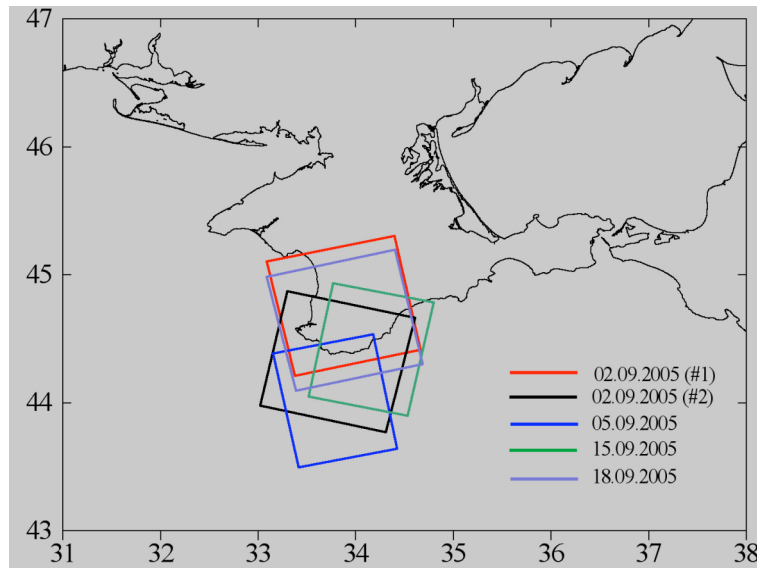


Figure 65. Scheme of ASAR scenes boundaries

The overall goal of experiment was:

- To provide ASAR ENVISAT images with simultaneous sets of in situ atmospheric and sea surface data.

The specific objectives were:

- to investigate experimentally peculiarities of the atmospheric boundary layer and momentum fluxes at the sea surface both clear and covered by natural films;
- to obtain wave spectrum measurements for both long and short waves;
- to study film kinematics and film transport under variety of wind and current conditions.

The experiment had 2 main tasks:

Task 1

- To obtain the estimates of friction velocity and roughness parameter. Special attention will be aimed at low wind and swell conditions
- To obtain dependence of short wave spectrum level on friction velocity.
- To study slick influence on wavebreaking and specular points on the sea surface.

Task 2

- To study spatial-temporal evolution of films.
- To study impact of wind-drift and surface currents into film drift vector.

Technical equipment used in experiment:

- Measurements of mean wind speed and its fluctuation were done simultaneously by cup anemometers with 0.3 m constant length at 5-6 heights from 1.5 to 20 m above the sea level.
- Long surface wave 2D spectra will be measured by wire resistance wave gauge array.
- Video-system provided measurements of wavebreaking characteristics.
- Vegetable oil used to create film slicks.
- Set of drifters used to define current velocity at various depths: 0.25m, 0.5m and 5 m.

- Laser system used to measure statistics of specular points on the sea surface.
- Meteosystem includes air temperature sensor (11m height), water temperature sensor (1.5m depth), wind speed vector sensor (23m height), humidity and pressure sensors.
- Autonomous floating buoy with wave elevation, wind speed, air and water temperatures gauges will be used to carry out measurements close to films.

3.3.2 Meteorological and wave measurements

Meteorological and wave experiment conditions are shown in Table 3. Wind velocities and directions and frequency and spatial wave spectra during ENVISAT missions are illustrated in Fig. 66. All measurements were carried out under steady wind conditions. There is wind velocity U , wind direction φ_w , air temperature t_a , water temperature t_w , significant wave height $H_s = 4 \cdot \sigma_w$, where σ_w - mean square height of wind waves, pick frequencies f_p and directions φ_p of swell and wind waves, inverse wave age in Table 3. Experiments #1, 4, 5 were carried out under weak wind and waves. Swell had dominating contribution into wave field.

Wave spectra shown in Fig. 66 were calculated using 20 minutes wave gauge records. As it following from figures experiment was defined with steady wave conditions. Wave directions were plotted in "inverse" coordinates (direction from) to better compare with wind direction.

Table 3. Meteorological and wave conditions

N	Date / Time	U, φ_w m/s	t_a / t_w (°C)	H_s , m	Swell f_p , Hz φ_p , deg.	Wind waves f_p , Hz φ_p , deg	Inverse wave age (wind wave and swell)
1	02.09.2005 08:06	3.5 / 177°	24.5° / 24.7°	0.29	0.29 Hz 85°	0.7 Hz	1.6 0.65
2	02.09.2005 18:15	5.9 / 19°	24.2° / 25.0°	0.21	0.24, 0.30 Hz 200°, 105°	0.9 Hz	3.4 1.1, 0.9
3	05.09.2005 18:31	8.6 / 14°	21.6° / 23.9°	0.23	0.15 Hz 210°	0.8 Hz	4.4 0.83
4	15.09.2005 07:58	1.3 / 145°	23.7° / 23.8°	0.10	0.31, 0.41 Hz 240°, 160°	-	- 0.26, 0.34
5	18.09.2005 18:22	1.5 / 24°	23.7° / 24.2°	0.17	0.23 Hz 120°	1.6 Hz	1.5 0.22

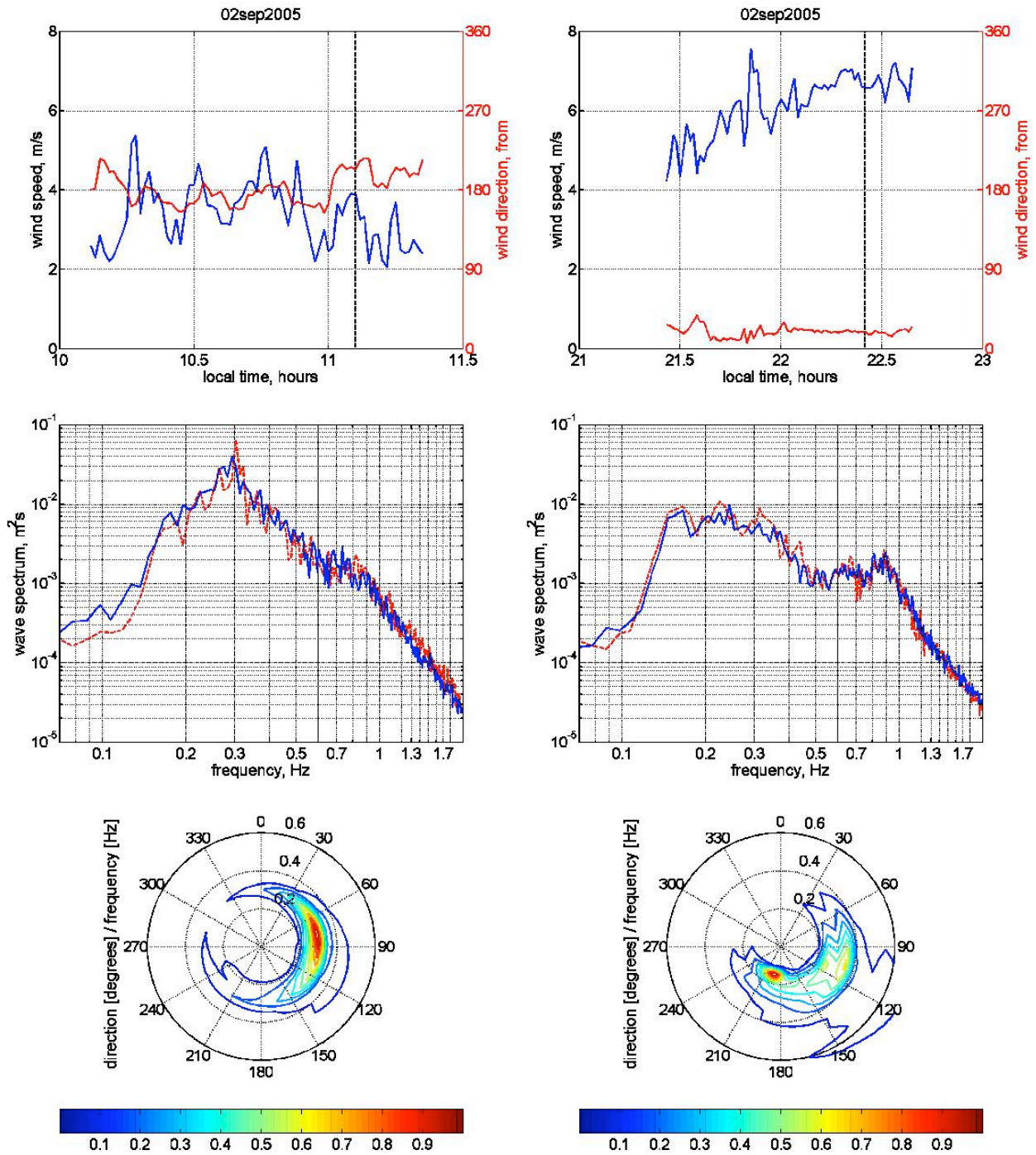


Figure 66 a. Meteorological and wave conditions. Wind velocities and directions (top), frequency wave spectra (in the middle), 2D spectra (bottom) on 02 September 2005 for ASAR scenes #1 (left column) and #2 (right column).

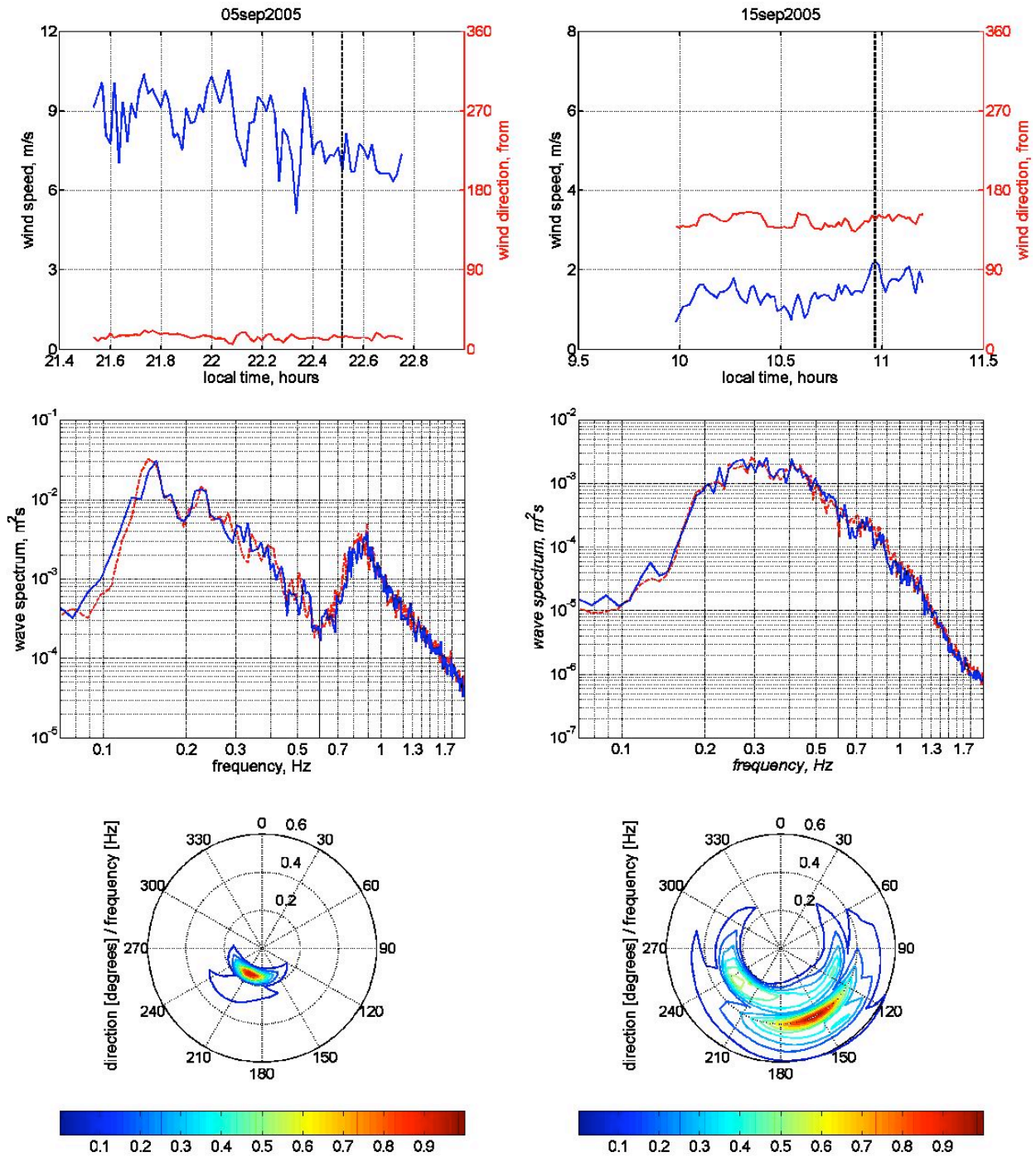


Figure 66 b. Meteorological and wave conditions. Wind velocities and directions (top), frequency wave spectra (in the middle), 2D spectra (bottom) for ASAR scenes #3 from 05 September 2005 (left column) and from 15 September 2005 #4 (right column).

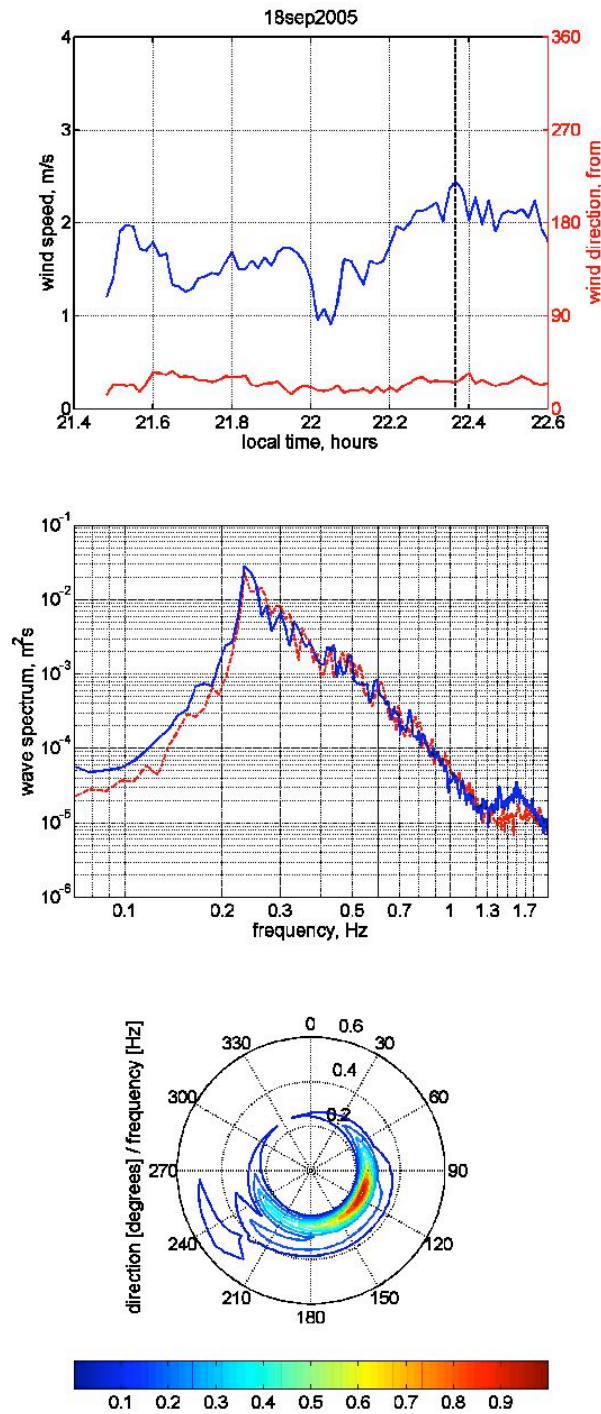


Figure 66 c. Meteorological and wave conditions. Wind velocities and directions (top), frequency wave spectrum (in the middle), 2D spectrum (bottom) on 18 September 2005 for ASAR scenes #5

3.3.3 Measurements of wind fluctuations

The main input data for existing short wave spectra models are atmosphere boundary layer (ABL) characteristics parameterized within similarity theory which is needed to be studied on marine

condition additionally [Yelland, Taylor, 1996]. Recent experimental researches show that it needs to take into account especially energy exchange between wind waves and ABL, dependence roughness parameter from wave age, the influence of swell at weak and moderate conditions, wind horizontal heterogeneity in coastal zones. In order to investigate these effects it needs to provide measurements of fluxes of momentum and heat in wave boundary layer (WBL) which can be estimated using measurements both wind speed profile, air temperature, their fluctuation spectra within inertial range (dissipation method) and simultaneous spatio-temporal characteristics of wind waves at different atmosphere stratification conditions.

Obtaining such experimental data will allow to improve the background short wind wave spectra [Kudryavtsev *et. al.*, 1999] and then to use it in pollution detect tasks.

The development of background short wind wave spectrum is needed to be compared with field investigations of ABL characteristics and first of all of friction velocity and roughness parameter. Toward this end measurements of mean wind speed and its fluctuation done simultaneously by cup anemometers with constant length 0.3 m on 5-6 heights from 1.5 to 20 m above the mean sea level. Obtained data used to calculate both friction velocity, roughness parameter and fluctuation spectra in inertial interval taking into account atmosphere stratification and wave induced fluctuation contribution into wind speed fluctuation.

Example of measured mean wind velocity profile ($H_s = 0.29$ m) is shown in Fig. 67 a. The Monin-Obuchov parameter is

$$L = -\frac{T_v u_*^3}{g \kappa T_v' w} \quad (3)$$

where g - gravitational acceleration, $\kappa = 0.4$ - Karman constant, $T_v = T \cdot (1 + 0.61 \cdot q)$ - potential air temperature at height z , q - specific water vapor. Value of $T_v' w$ was estimated with integral relation. Gradient and profile wind velocity within atmosphere boundary layer was determined as

$$\frac{\partial U}{\partial z} = \frac{u_*}{\kappa z} \phi_M(\xi), \quad \xi = \frac{z}{L} \quad (4)$$

$$U(z) - U_0 = \frac{u_*}{\kappa} \cdot \left[\ln \frac{z}{z_0} - \Psi_M(\xi) \right], \quad \Psi_M(\xi) = \int_{\xi_0}^{\xi} \frac{1 - \phi_M(\xi)}{\xi} \cdot d\xi, \quad (5)$$

where U_0 - surface velocity, $\xi_0 \leq 10^{-5}$ in real conditions. Corrective function $\phi_M(\xi)$ is written as

$$\phi_M(\xi) = 1 + \gamma_1 \cdot \xi, \quad \xi \geq 0, \quad \phi_M(\xi) = (1 - \gamma_2 \cdot \xi)^{-1/4}, \quad \xi \leq 0 \quad (6)$$

where $\gamma_1 = 5 \dots 7$ and $\gamma_2 = 15 \dots 16$ for stable and unstable respectively. Wind profile was approximated with linear-log dependence

$$U(z_i) = a + b \cdot \ln(z_i)$$

Then taking into account (3-6) and $u_* = b \cdot \kappa$ values of L , u_* and velocity profile were calculated. Wind velocity profile shown in Fig. 67a is in good agreement to logarithmic law. Experimental estimation friction velocity $u_* = 0.254$ m/s has mean square deviation 0.013 m/s.

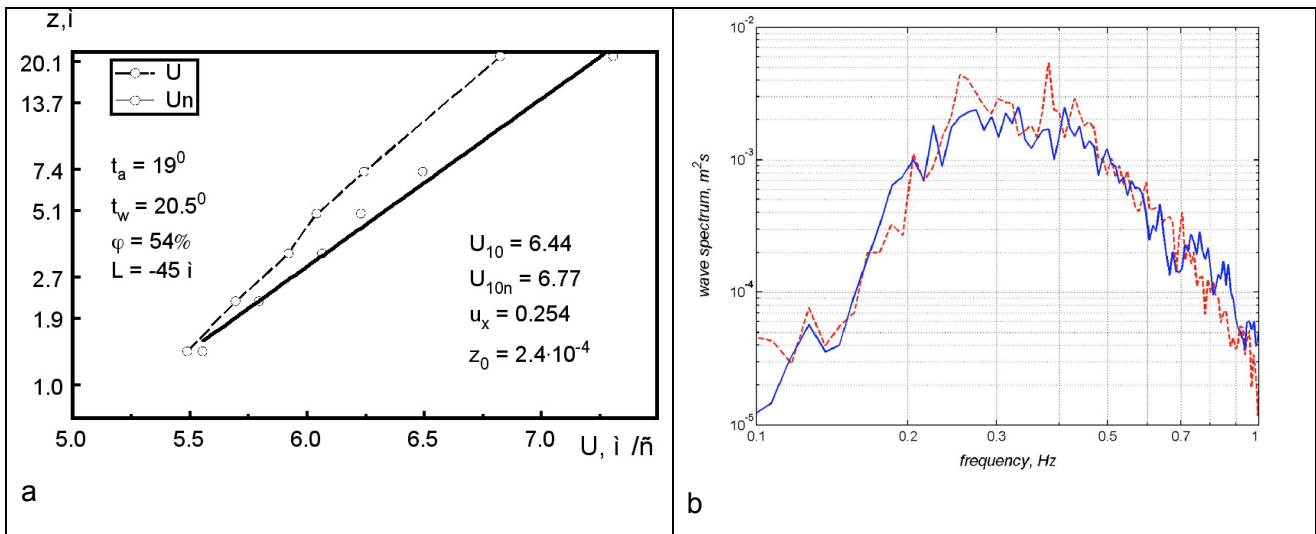


Figure 67 (a) Example of measured mean wind velocity profile; (b) Example of wave spectra obtained with buoy and measured in platform during experiment #4

3.3.4 Autonomous buoy measurements

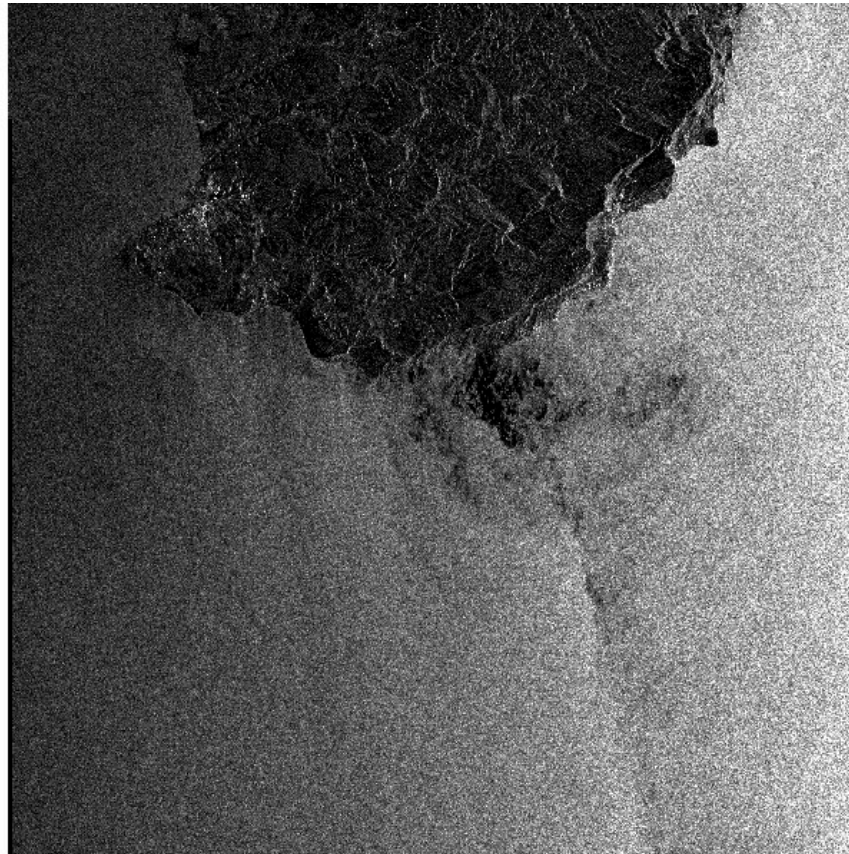
Autonomous buoy was located 2.3 km offshore platform. Set of measured parameters included air temperature at 1.5 m height, water temperature at 1.5 m depth, wave elevations using wave gauge. Example of wave spectra obtained with buoy and measured in platform during experiment #4 are illustrated in Fig. 67b. As it follows from figure both spectra are practically the same but in buoy data two swell systems are distinguished more clear. According buoy data water temperature was 23.8°C (equal to t_w measured in platform) but air temperature was 24.3°C (lower measurements in platform). Autonomous buoy data extends possibilities to analyze ASAR images.

3.3.5 ASAR ENVISAT images

ASAR ENVISAT images are illustrated in Figs 68 (a – e) where QuickLooks and area of experiment are shown. All scenes except from 18 September 2005 are obtained at V/V and V/H polarization. The scene from 18 September was done at H/H and H/V polarization. All ASAR fragments were transformed into geographic projection where axis correspond to East longitude and North latitude. Oceanographic platform is observed in radar images as “bright point” with coordinates 44.391°N , 33.982°E .

It follows from Table 2 that experiment was carried out both under moderate (02 September and 05 September) and weak wind moderate (15 September and 18 September) conditions. Under wind velocities 6-8 m/s radar signal level is practically similar in experiment area (Fig. 68 a – c). Other situation is observed under almost calm conditions. Extensive dark along south coast of Crimea in Fig. 68 d is concerned with wind absence in this region. Numerous thin lengthy dark features are the areas of smoothing sea surface. Similar wind spatial heterogeneity close to coast is shown in Fig. 68 e at H polarized backscattering.

The data set obtained in the experiment will be analysed to improve radar retrieval algorithms.



02-09-2005 ORBIT=8340 08:06:30 Rows= 2501:4500

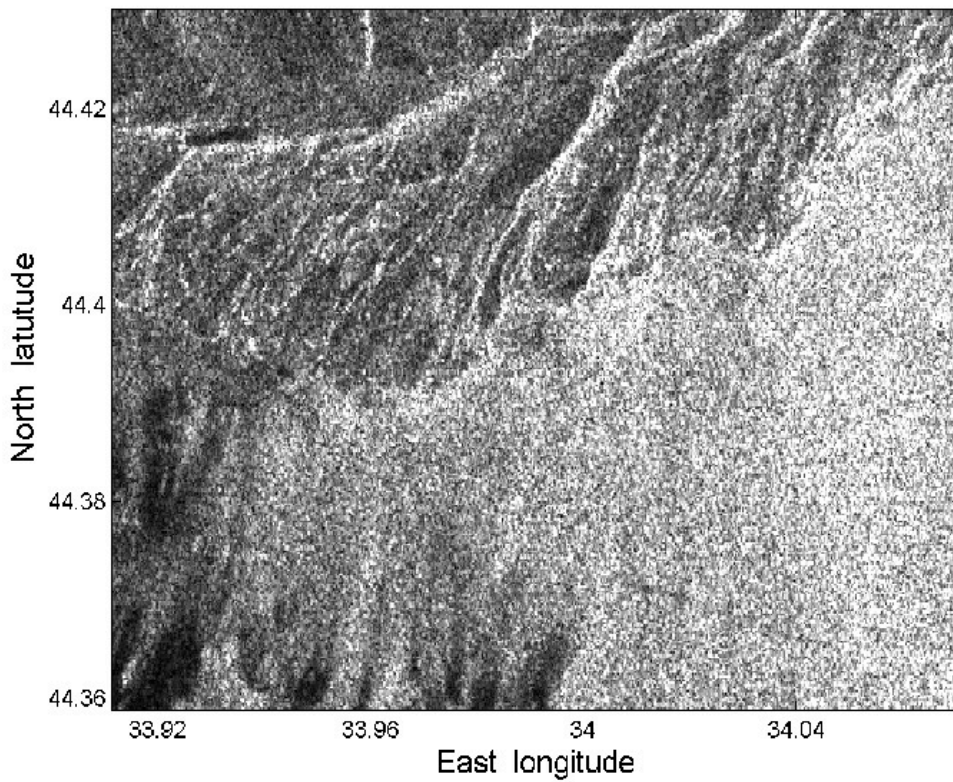
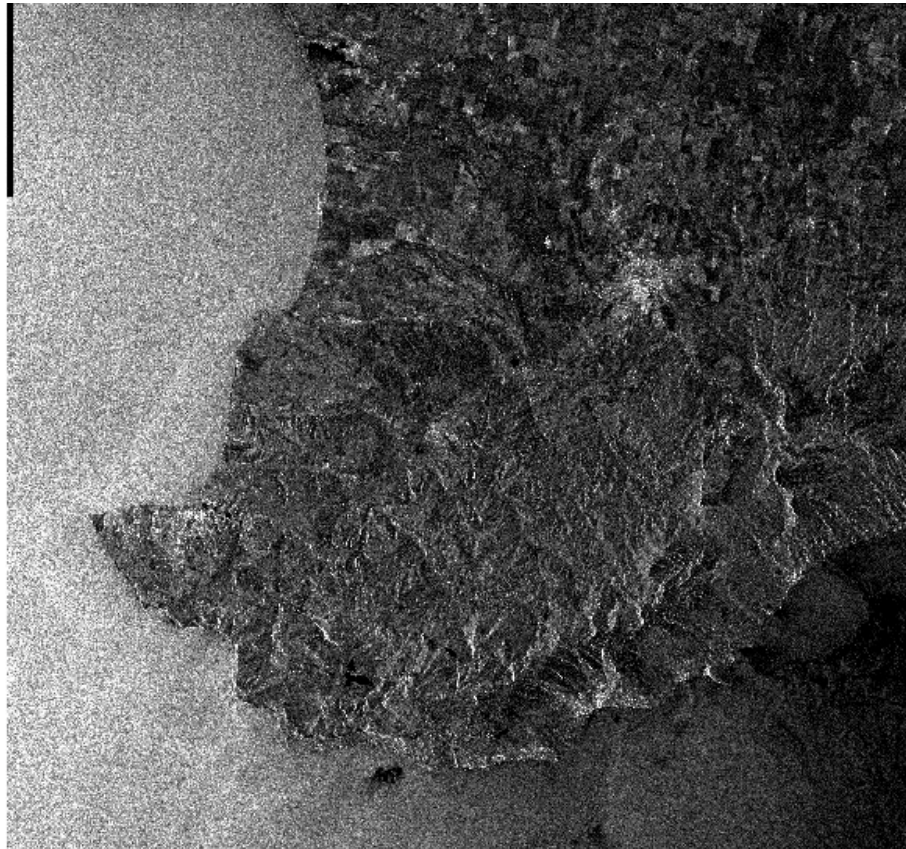


Figure 68 a. ASAR ENVISAT images from 02 September 2005 (08:06:30.433 GMT)



02-09-2005 ORBIT=8347 19:25:16 Rows= 1:2000

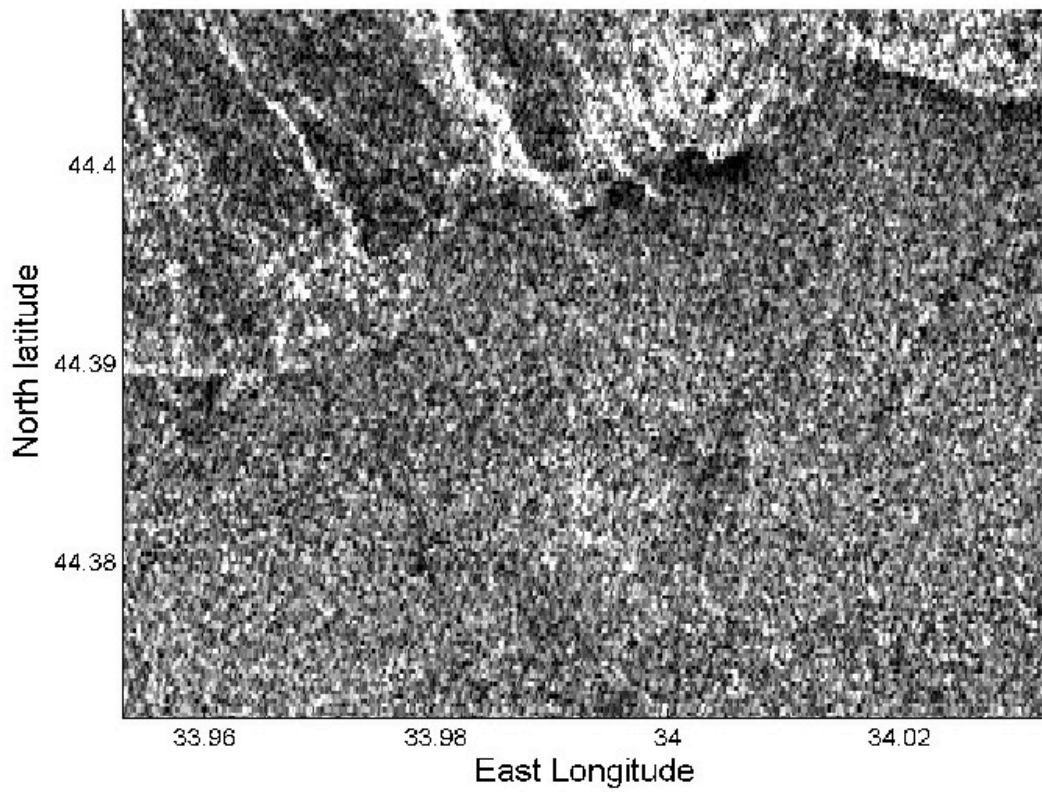
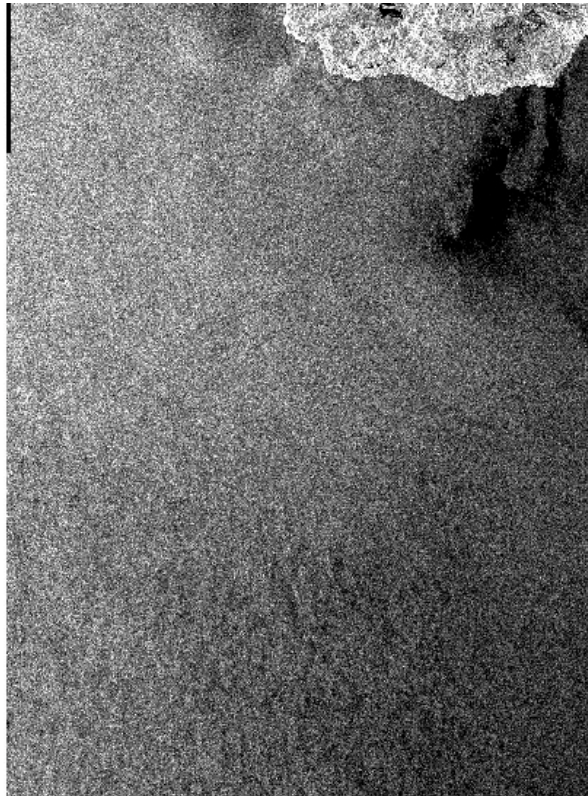


Figure 68 b. ASAR ENVISAT images from 02 September 2005 (19:25:16.862 GMT)



05-09-2005 ORBIT=8390 19:30:45 Rows= 6000:7500

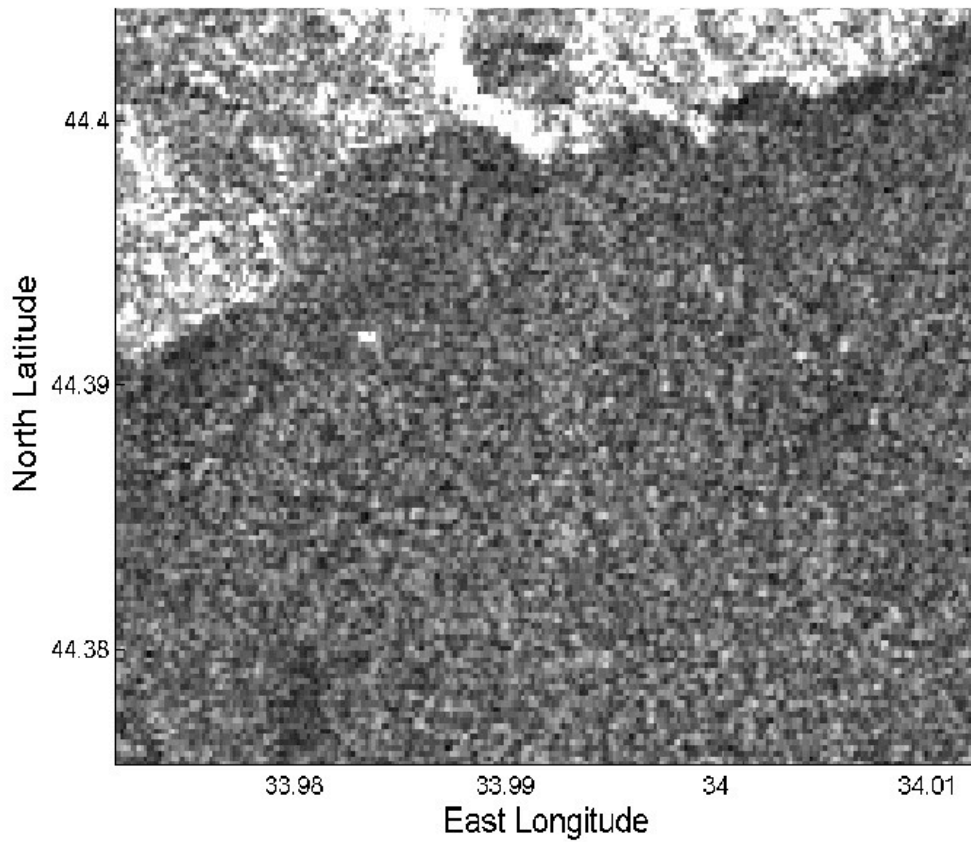
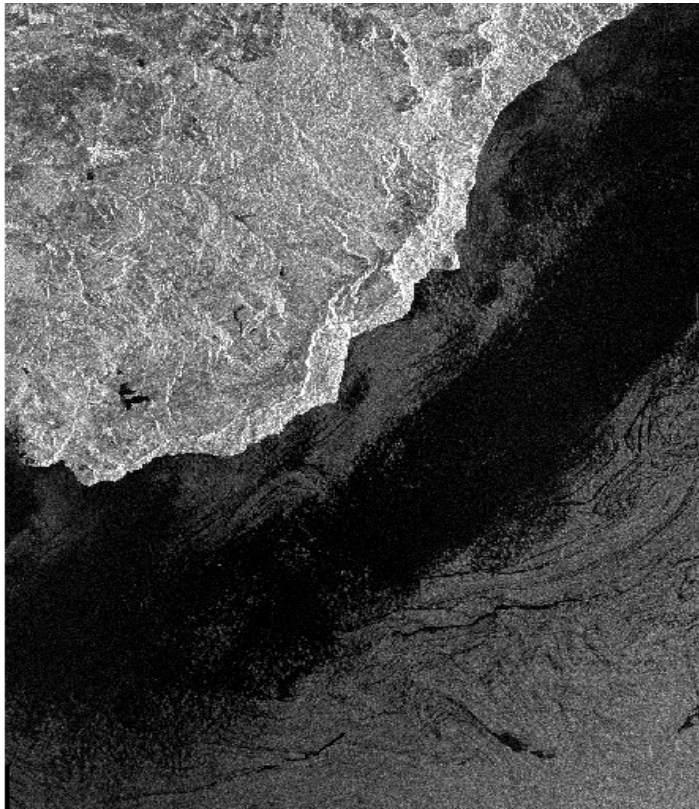


Figure 68 c. ASAR ENVISAT images from 05 September 2005



15-09-2005 ORBIT=8526 07:57:56 Rows= 4001:5500

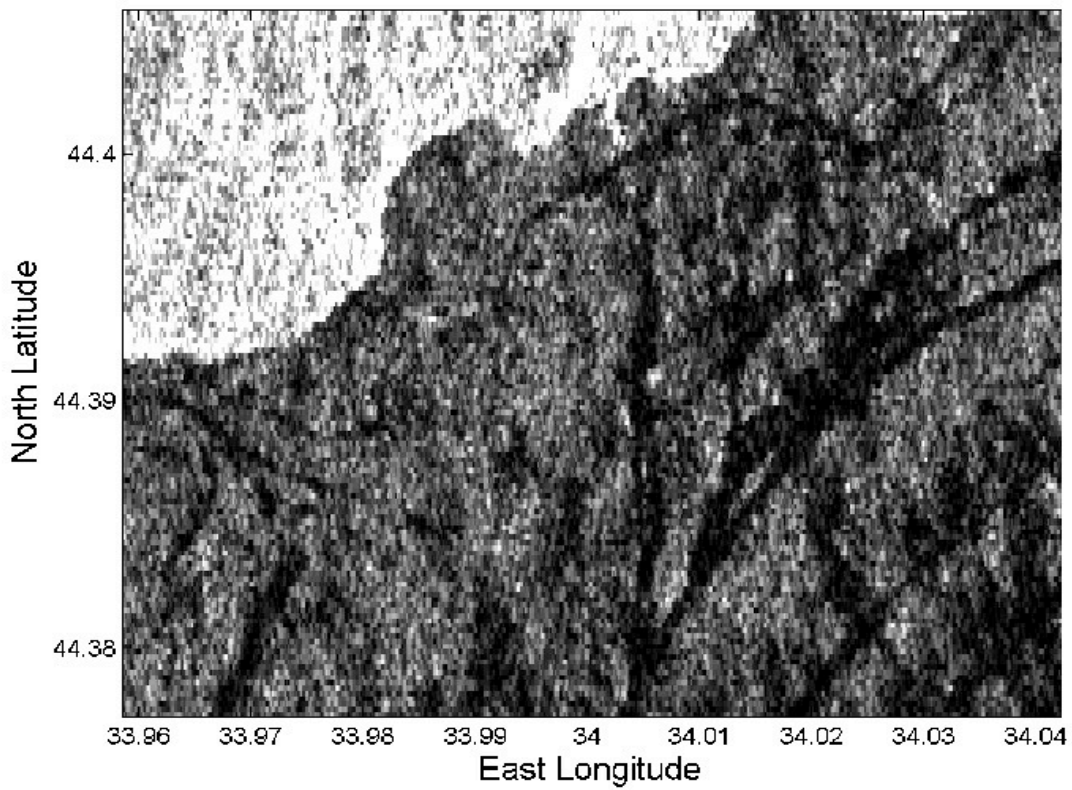


Figure 68 d. ASAR ENVISAT images from 15 September 2005

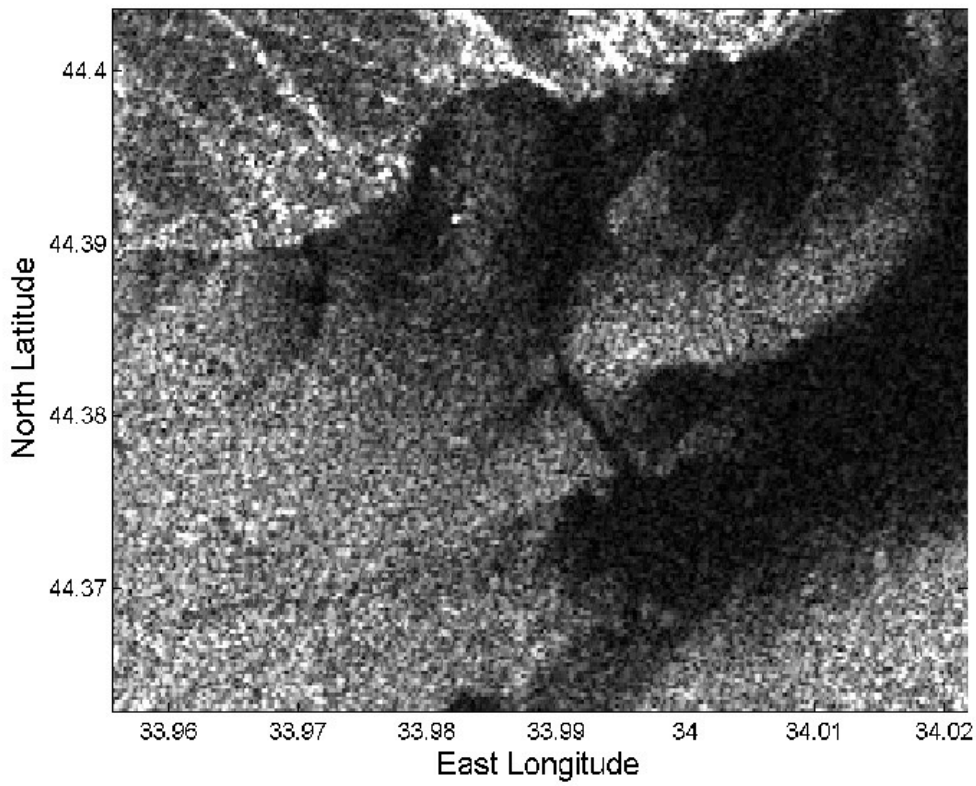
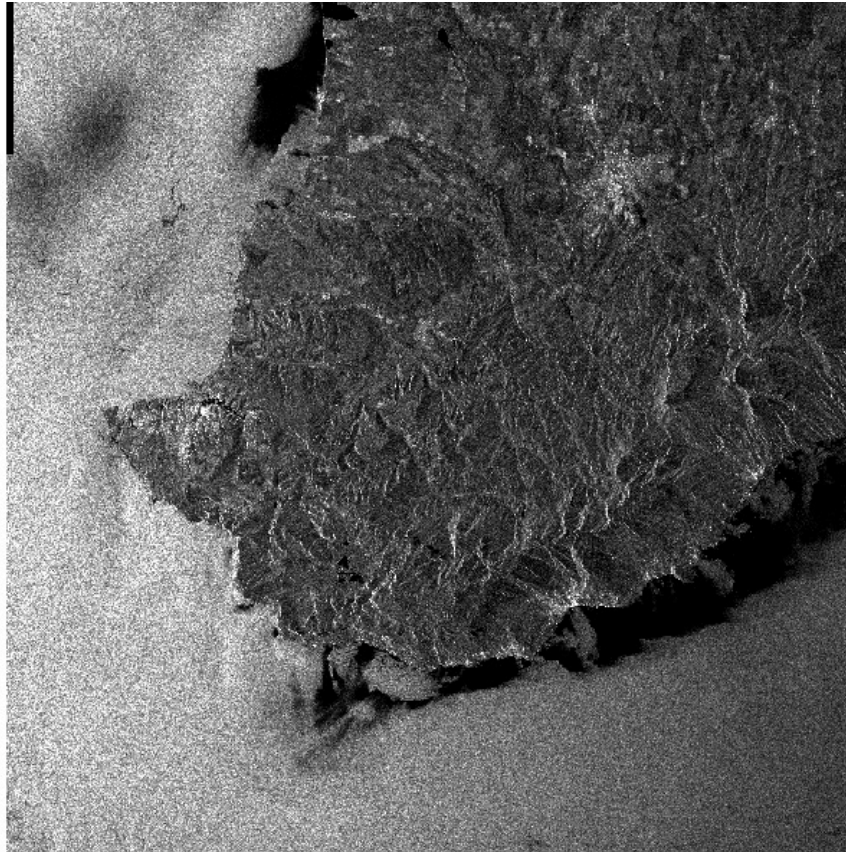


Figure 68 e. ASAR ENVISAT images from 18 September 2005

3.3.6 Preliminary conclusions from the field experiment

Experiment including synchronous ASAR scenes and field measurements of atmosphere and sea surface parameters responsible for forming radar backscattering is the first attempt of collaboration European and Ukraine scientists to provide specialized ASAR monitoring of the Black Sea. The main outcome of the experiment are:

- simultaneous ASAR ENVISAT and field data set is obtained;
- results will be used to develop models of analyse radar images;
- it is gained experience to plan and provide monitoring of the Black Sea in frame of international cooperation
- an integrated data set that will be used for further studies of SAR imaging of the ocean surface

Task 4: Oil drift modeling in cold ice-covered waters

Task leader: Arctic and Antarctic Research Insitute

An oil drift modeling system has been improved and developed for continuous oil spills in the ice-infested seas (OilMARS, v.2). A diagramme of the model system is presented in Fig. 69.

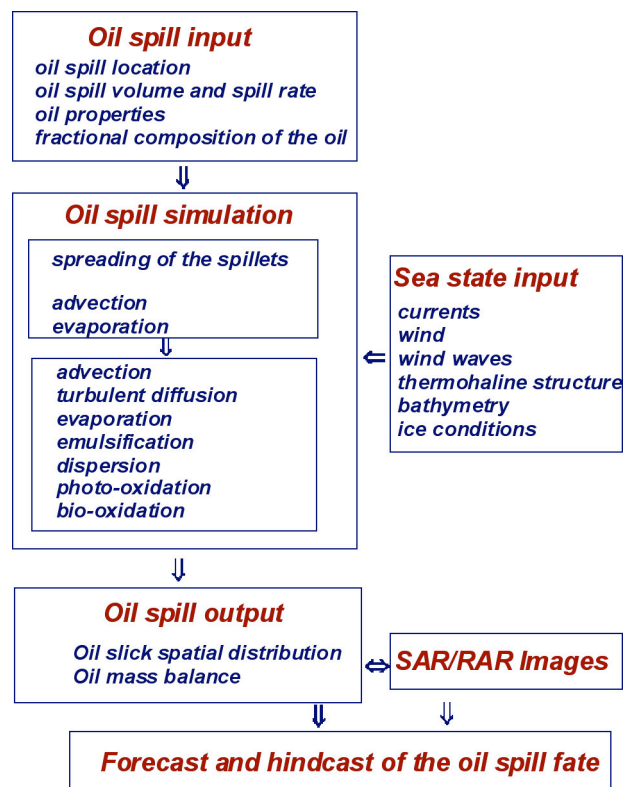


Figure 69. Schematic layout of oil spill model

The oil spill model system is developed and adopted for the Barents and Kara Seas. The model system consists of the modules:

- *3-D dynamic-thermodynamic model of ocean circulation*

This model is developed to simulate synoptic, seasonal and interannual variability of hydrologic characteristics in the Arctic Ocean. It is based on the movement equations, Z coordinate, free surface model and adapted to the Arctic Ocean. The model uses the Hibler ice model (1979). The ice thermodynamics is determined by energy budget at the ice/snow surface (Parkinson and Washington, 1979). The model is run with a spatial resolution 28 km and 75 vertical layers. Calculations are conducted with ERA40 6-hour atmospheric fields. Within the frames of OSCSAR project 3-D dynamic-thermodynamic model of ocean circulation is verified by the measurements and adapted to the Kara Sea.

- Wind wave model

Within the frames of OSCSAR project wind wave model was verified by the measurements in the Barents Sea and adapted to the Kara Sea. Three-year wind wave hindcast is fulfilled in the Barents Sea with the help of the WAM-4, WAVEWATCH-1.18 and AARI-PD2 models. Results are compared with NORDKAPP/ST buoy measurements. It is shown that all models provide comparable results. However, the wave height estimations obtained with the help of the AARI-PD2 models are more accurate spatially for strong storm situation. Moreover, the AARI-PD2 model is 20 times faster than the WAM model and 45 times faster than WAVEWATCH-1.18. It allows concluding that the AARI-PD2 model is optimal for the operational –prognostic purposes as well as for obtaining long-term wave element series for solving climatic problems.

- *Oil spills transport and evolution model OilMARS v.2 (Oil spill Model for the Arctic Seas)*

Within the frames of **OSCSAR** Project the model is developed for continuous oil spills in the ice-infested seas. Model represents the oil spill by a number of spilletts, which are released from the place of accident (tanker or deposit) at some rate. After releasing spilletts drift under influence of the wind, sea circulation, tidal and wave Stokes currents. All these forces are spatial and temporal variable and performed by the water circulation and wave models. Circulation model grid is used for spillet's drift, water temperature and salinity distribution (also spatial and temporal variable).

Oil evolution processes (spreading, horizontal diffusion, evaporation, photo- and biooxidation, emulsification (water-in-oil) and natural dispersion (oil-in-water)) are considered for each spillet using the high-resolution grid. Each spillet has a set of parameters: coordinates, density, viscosity, oil mass remained in the water surface, oil mass lost due to evolution. The model also takes into account the changing of the oil density and viscosity depending on water temperature, evaporation of the light oil fractions and emulsification. The model takes into account the ice conditions (ice concentration and ice drift), which essentially influence on a polluted area and evolution processes.

The performed numerical experiments are performed by varying the following parameters:

- Different locations of the oil spill;
- Different time (season) of the oil spill;
- Different parameters of the oil spill.

Oil modeling properties are corresponded to properties of the oil of the upper layer of the Prirazlomnoe deposit (the Pechora Sea) (Table 4). The location of the modeled oil spills is presented in Fig. 69. Here, **Point 1** corresponds to the Prirazlomnoe Deposit (the Pechora Sea), **Point 2** is located in the Kara Gate (Karskie Vorota) Strait, **Point 3** is located in the vicinity of the Cape Harasavey and Point 4 is located in the Ob-Yenisey coastal zone. The main characteristics of the experiments are presented in Table 5.

Table 4. Input information about the oil properties

Parameters	Value
Initial oil density (kg/m ³)	908.
Initial oil kinematic viscosity (cSt)	78.2
Reference temperature (°C)	20
Molecular weight	228
Asphalt content (%)	5.62
Wax content (%)	0.7
Final volume fraction of water in w/o emulsion	0.7
Number of fraction	4
Boiling temperatures of fractions (°C)	68; 100; 200; 300
Masses of fractions (%)	2.; 11.4; 39.; 52.4

Table 5: Main characteristics of the numerical experiments

No	Spill mass, ton	Period of the spillets release, min	Time of the spill start	Location	Spill rate
1	10,000	10	15 September	Point 1	constant
2	10,000	10	15 September	Point 2	constant
3	10,000	10	15 September	Point 3	constant
4	10,000	10	15 September	Point 4	constant
5	10,000	10	1 October	Point 1	constant
6	10,000	10	1 October	Point 2	constant
7	10,000	10	1 October	Point 3	constant
8	10,000	10	1 October	Point 4	constant
9	10,000	10	15 November	Point 1	constant
10	10,000	10	15 November	Point 2	constant
11	10,000	10	15 November	Point 3	constant
12	10,000	10	15 November	Point 4	constant
13	10,000	10	1 May	Point 1	constant
14	10,000	10	1 May	Point 2	constant
15	10,000	10	1 May	Point 3	constant
16	10,000	10	1 May	Point 4	constant
17	10,000	1	15 September	Point 2	constant
18	10,000	5	15 September	Point 2	constant
19	10,000	20	15 September	Point 2	constant
20	50,000	10	15 September	Point 2	constant
21	15,000	10	15 September	Point 2	constant
22	15,000	10	15 September	Point 2	Linear
23	15,000	10	15 September	Point 2	Steps

The numerical experiments with various modeling input parameters: oil spill location, spill volume and rate, hydrometeorological and ice conditions. Results from some of the experiments are described. Experiments no. 5 – 8 were performed during ice-free conditions in all the four points with spills starting on October, 1 (Tab. 5). Number of spillets was equal to 1,000. Initial fields of the surface water circulation, wind and wind waves height are presented in Fig. 70. The balances of all oil spills are presented in Figure 71. The contribution of different processes in the total oil destruction within 10 days after spills started is presented in Table 6. Simulated trajectories of the modelled spills are presented in Fig. 72.

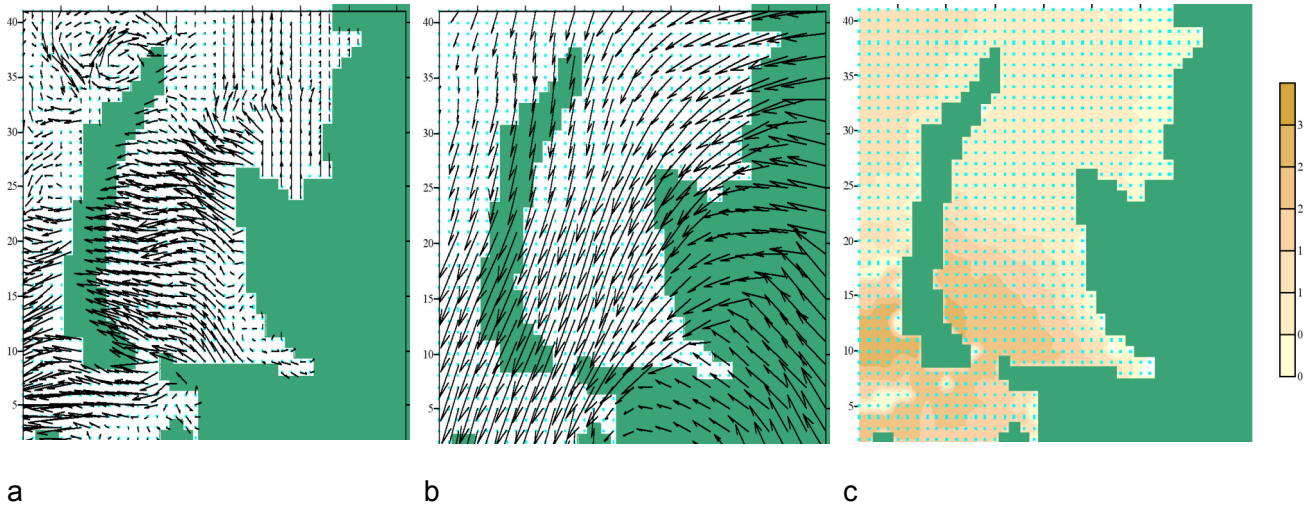


Figure 70. Initial fields at the start of experiments no. 5 – 9 on October 01 for (a) surface currents, (b) surface wind, and (c) surface waves.

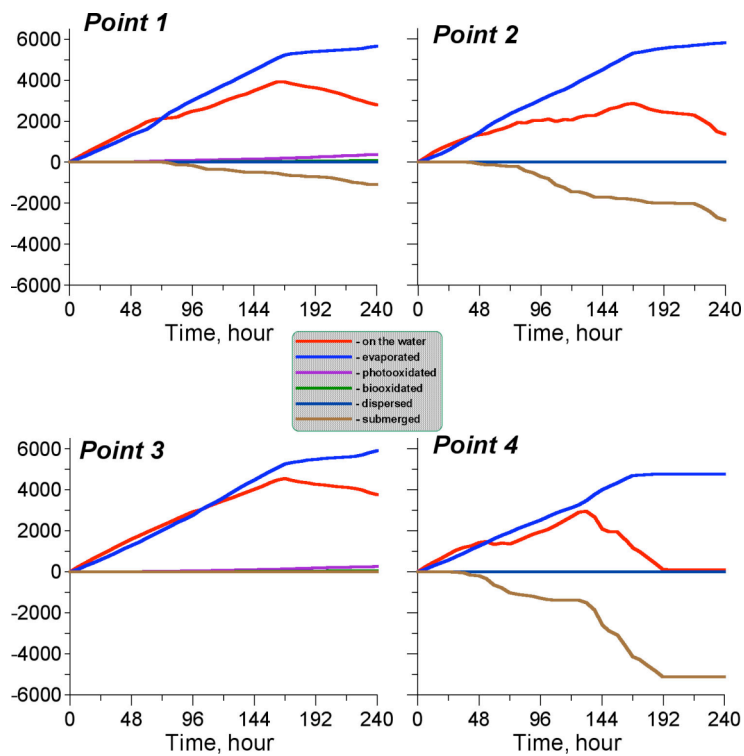


Figure 71. Oil mass balance for experiments 5 – 9

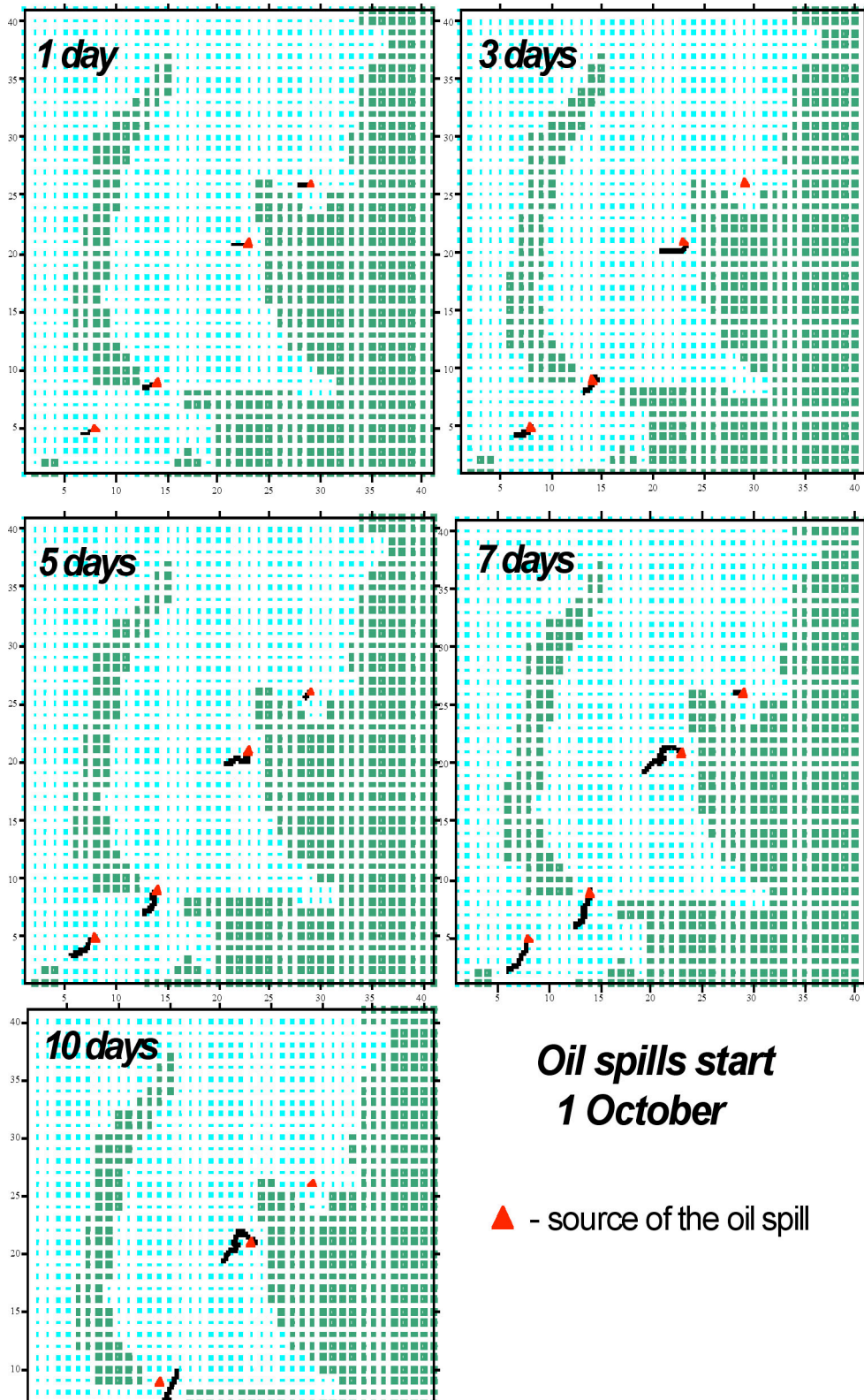


Figure 72. Results of oil drift in experiments 5 - 9

Table 6: Oil mass balance (%) 10 days after spills started on October 01

Oil mass	Point 1	Point 2	Point 3	Point 4	Mean
On water surface	28.0	30.6	37.7	0.0	24.1
Evaporated	56.6	55.3	59.2	47.5	54.6
Photo-oxidized	3.7	1.9	2.6	0.4	2.2
Bio-oxidized	0.8	0.4	0.5	0.1	0.5
Dispersed	0.04	0.01	0.03	0.01	0.02
Submerged	10.9	11.7	0.0	51.9	18.6

Another series of experiments were performed in complete ice cover in May (experiments no.13 – 16) (Tab. 5). Number of spilletts was equal to 1,000. Initial fields of the wind, ice concentration and ice drift are presented in Figures 17-19. Simulated trajectories of the modeling spills and the balances are presented in Figures 20 - 21. The contribution of different processes in the total oil destruction in 10 days after spills started is presented in Table 7. In May, the Kara Sea is entirely covered by fast and drifting ice.

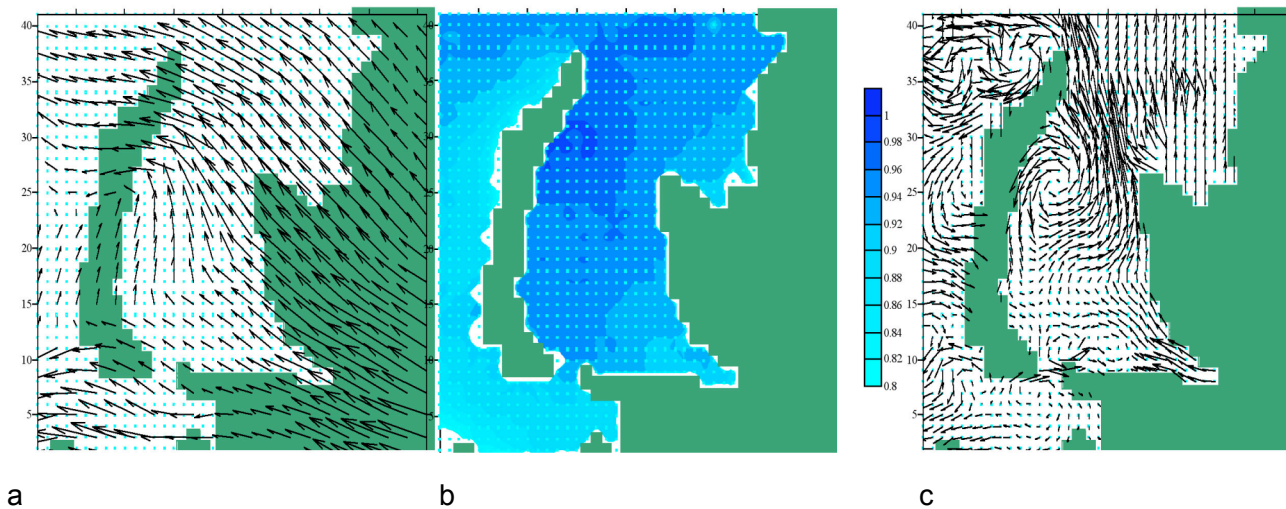


Figure 73. Initial fields at the start of experiments no. 13 - 16 on May 01 for (a) surface winds, (b) ice concentration, and (c) surface currents.

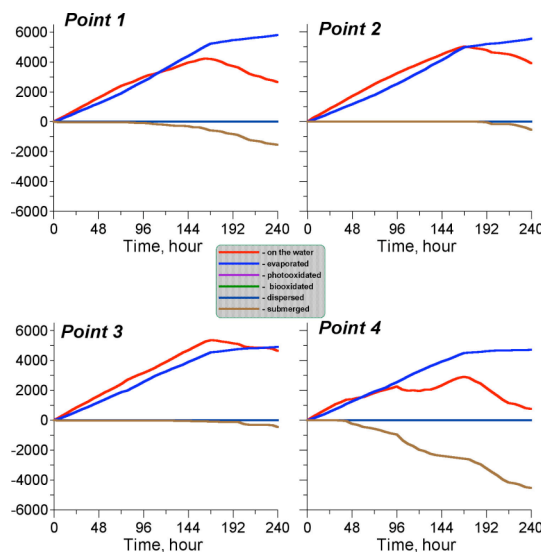


Figure 74. Oil mass balance for experiments 13 – 16

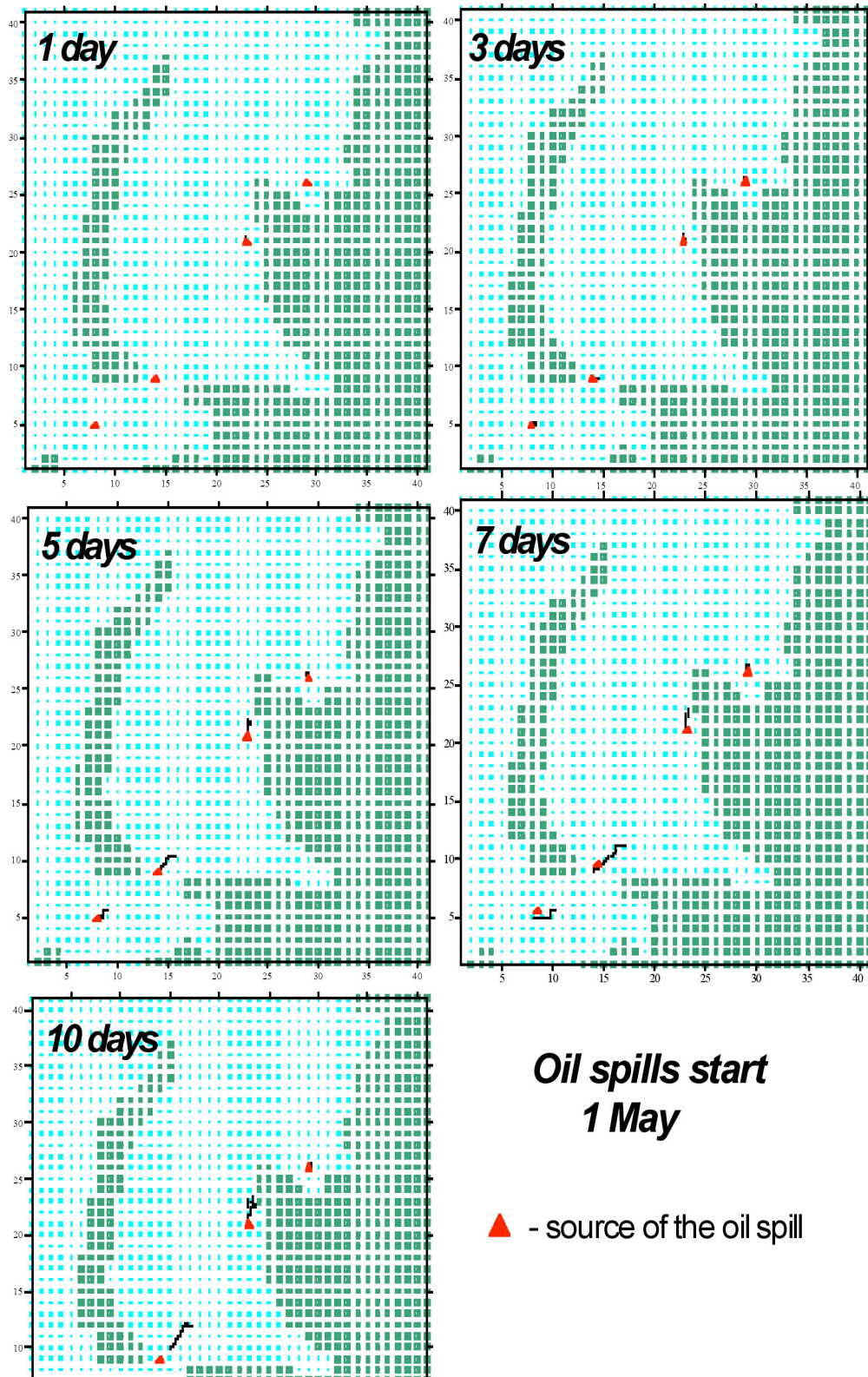


Figure 75. Results of oil drift in experiments 13 - 16

Table 7: Oil mass balance (%) in 10 days after spills started on May 01

Oil mass	Point 1	Point 2	Point 3	Point 4	Mean
On water surface	26.5	39.1	46.6	7.7	30.0
Evaporated	58.0	55.5	49.0	47.1	52.4
Photo-oxidized	0.0	0.0	0.0	0.0	0.0
Bio-oxidized	0.0	0.0	0.0	0.0	0.0
Dispersed	0.0	0.0	0.0	0.0	0.0
Submerged	15.5	5.4	4.4	45.2	17.6

Oil modeling properties are correspondent to the properties of the oil in the upper layer of the Prirazlomnoe Deposit (the Pechora Sea). The location of the modeling oil spills corresponds to Prirazlomnoe Deposit, in the Kara Gate (Karskie Vorota) Strait, in the vicinity of the Cape Harasavey and in the Ob-Yenisey coastal zone.

Spill location is very important for oil spill fate. The distance from the coast determines the probability of approach of the spillets to the shore. The most unfavourable experimental location was near the cape Harsavey. In this case oil stretches along the coast line, oil area decreases and thickness increases. This phenomenon influences on the oil evolution processes. Also, unfavourable spill location is the region in front of estuaries due to the low surface water density. In this case oil quickly become denser than surface water and submerge. Fate of the oil spills and behavior of the spillets significant depend on the atmospheric processes and water circulation. These processes influence on the trajectories of the spillets as well as on the oil evolution processes.

The oil losses due to evaporation, photooxidation and biooxidation are in the good agreement with the observations. Low quantity of dispersed oil may be explained by influence of the high oil viscosity, moderate wind speed, not great heights of wind waves and also by imperfection of used parametrization.

Influence of the ice concentration on the distribution of the spillets and oil mass balance is very significant. Ice cover causes the slowing down of oil evolution processes owing to the decreasing of area of spillets. Furthermore, ice concentration significant influences on the trajectories and velocities of the spillets.

Parameters of oil spills (period of the spillets released, time discretizations, volume and rate of spill) significant influence on the evolution of oil spills. Experiments with variable spill rates are the most interesting. At the similar trajectories caused by water circulation and atmospheric processes there are significant differences in the oil evolution processes and areas of oil spillets. As it is shown by the performed numerical experiments the developed model OilMARS is able to work under various spatial and temporal conditions.

Task 5: Dissemination and promotion

The dissemination and promotion activities have focused on publications, reports, and presentations at conferences. The most significant conference was the ISPRS conference in St. Petersburg 20 – 24 June 2005, where OSCSAR was presented at the BEAR session and a poster was displayed. A list of publications and abstracts for conference presentation is presented below.

Yuzhnoye (DOYu) has in particular focused on promoting use of SAR in oil spill monitoring towards the Ukrainian Space Agency and in planning new Ukrainian satellites for pollution

monitoring. A proposal has been prepared to participate in the Third Open All-Russian Conference “Current problems of Earth remote sensing” based on the report “OSCSAR Project results of GMES Program and preparation of Sich-3m continuous radiolocation sensing spacecraft”.

The Sich-1M SC carrying Side-Looking Radar was launched and images from the satellite were planned to be used in OSCSAR. However, the satellite was not placed correctly in orbit. Therefore only one SLR image was obtained (Fig. 76). The Sich-1M images were processed, however, the level of signals reflected from the Black Sea surface turned out to be at the level of noises, therefore, the indications of films on the sea surface were not identified.

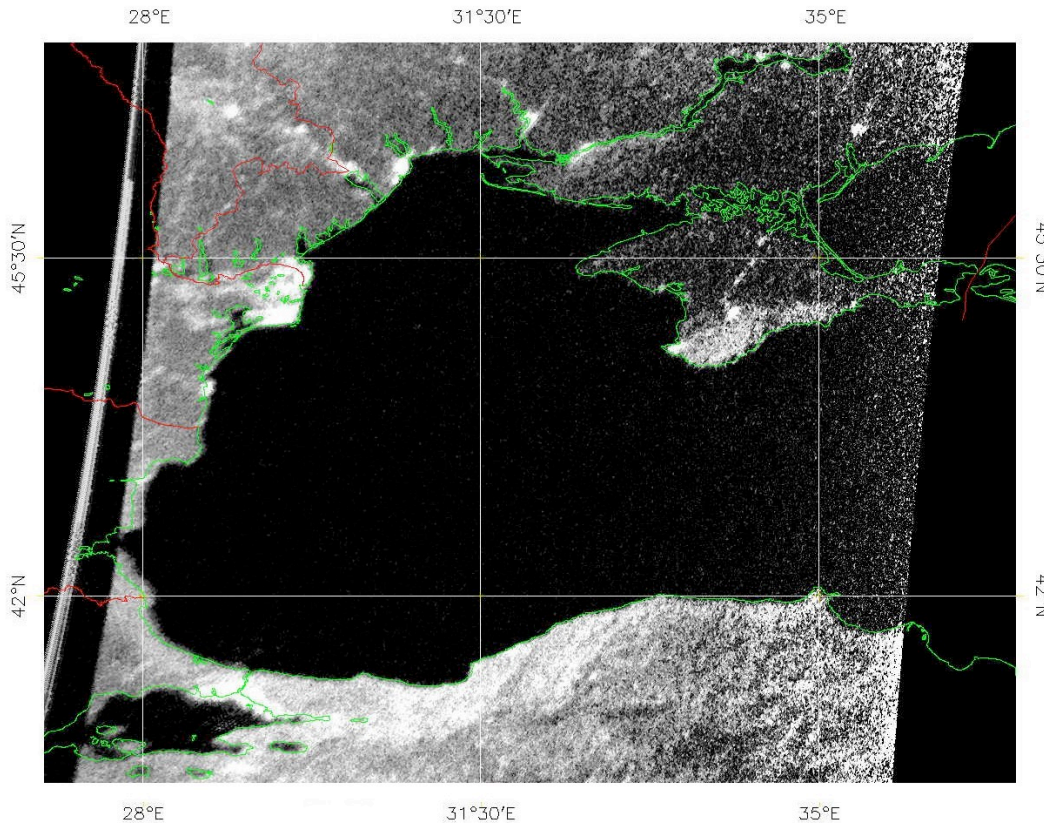


Figure 76: SLR image from Sich-1M covering the Black Sea.

In evolution of work activities performed within the framework of the OSCSAR Project, Yuzhnoye prepared a proposal on inclusion into the Space Program of Ukraine the promising Sich-3-R Earth radiolocation observation spacecraft with synthetic aperture. The technical specifications of Sich-3-R are given in Table 7.

The Sich-3-R application domains are the following:

- Identification of mineral oil products spills on the water surface.
- Online hydro-meteorological monitoring of the Earth including online monitoring of meteorological processes over the sea surface (detection of gale zones, hurricanes, typhoons, evaluation of their strength and movement direction), definition of velocity and direction of driving wind, monitoring of cyclonic activity manifestations on the mainland and monitoring of ice covers.

- Ecological monitoring.
- Definition of integral soil moisture content.
- Control of status of farming lands, forests, inundation zones, and oth.
- Detection of engineering facilities on sea and control over their movement.

Table 7: Essential parameters of Sich-3-R spacecraft (www.yuzhnoye.com):

Swath resolution	2x2 m
Operating wavelength	3 cm
Swath width	20 km
Acquisition sweep	400 km
Synthesis of radiolocation image	Ground processing
Operational mode	Session
Orbit type	Sun-synchronous
Orbit altitude	626 km
Orbit inclination	97.9 deg.
Orientation accuracy	15 ang. min.
Stabilization angular velocity	0.001 deg/s
Average daily capacity	280 W
Launch mass	650 kg
Designed operational life, years	5 years
Planned year of launch	2007

In addition Sich-3-R can receive detailed digital information of the relief and small (millimeters and first centimeters) shifts of the earth surface, to predict the dynamics of those processes on the basis of a radar interferometry method and to apply practically the above method in the geocological and engineering-geological investigations. In this case we will receive direct quantitative values of the intensity of slow shifts of the earth surface which forestall the catastrophic shifts and provide a possibility to focus the attention of geologists on slow volcanogenic processes and earthquakes before the time when they become dangerous. The dynamics of propagation of the flood zones will also be determined.

A state of technogenic objects will be predicted with high resolution, in particular: small displacements of large-sized facilities; slow shifts connected with redistribution of huge masses in the mining areas, in oil and gas production areas and also at the sections of underground transport lines of the subways inside the cities. In general, the operations connected with development and application of the satellite interferometry technology can be used in various branches of the national economy.

The Russian Space Agency has a series of new earth observation satellites mainly operating in the optical bands. NTs OMZ is the head enterprise of Russian Space Agency ground information system. The NTsOMZ gives recommends to use the remote sensing data from new Russian spacecrafts. An overview of the new optical satellites is given in table 8.

In August 2005 the MONITOR-E satellite was launched from the cosmodrome in Plesetsk. The Russian-Belarusian BelKA spacecraft is scheduled for launch in April of this year. The RESURS - DK1 satellite is scheduled for launch in June of this year.

Furthermore, the METEOR-M satellite will be equipped with SAR SEVERYANIN. Its swath width is 800 km in one operational mode. The resolution in this mode is 400 m. This SAR data can be of great significance in global monitoring and in particular to detect oil spills on the sea surface. More info on <http://www.ntsomz.ru>

Table 8. Specifications of the new Russian earth observation satellites

Satellite	MONITOR-E	BeIKA	RESURS-DK1
Launch time	August 2005	April 2006	June 2006
Resolution			
Pan-chromatic mode	8 m	3.2 m	1 m
Narrow spectral band	20 m	12 m	2 – 3 m
Swath width			
Pan-chromatic mode	90 km	< 20 km	4.7 – 28.3 km
Narrow spectral band	160 km		
Spectral bands			
Pan-chromatic band	0.51 – 0.59 μm	0.52 – 0.90 μm	0.58 – 0.80 μm
Narrow spectral bands	0.54-0.59 μm 0.63-0.68 μm 0.79-0.90 μm	0.54-0.60 μm 0.60-0.69 μm 0.69-0.75 μm 0.75-0.86 μm	0.50-0.60 μm 0.60-0.70 μm 0.70-0.80 μm

Training and education activities have been conducted where students from Moscow State University (MSU) branch in Sevastopol participated in the following work:

1. The field experiments on the oceanographic platform to investigate film kinematics were co-ordinated with summer student practical works for chair of atmosphere physics (MSU) and chair of physics and geophysics (Sevastopol branch of MSU). During the experiment 5 student teams (7-15 persons each) took part in different stages of the field studies. MHI team members read a series of lectures about both OSCSAR project tasks and problems with remote sensing monitoring of oil pollution.
2. Using acquired field data to involve students in scientific data analysis. Based on the experiments results one student got bachelor's degree. Two reports were presented at student science conferences. One report is planning to be at international student conference 'Lomonosov-2006' in May 2006 (Moscow). One MSU student is co-author of published paper with reference on OSCSAR project.

List of publications, reports and abstracts where OSCSAR is acknowledged

IAP

S.A. Ermakov, I.A. Sergievskaya, L.A. Guschin, and Yu. B. Shchegolkov, Radar probing of organic and oil films on the sea surface. in "Manifestations of underwater processes on the sea surface" (ed. V.V.Bakhanov), Nizhny Novgorod, IAP RAS, 2006, in press (in Russian)

NIERSC

Papers:

Akimov, D., B. Chapron, J. A. Johannessen, V. Kudryavtsev. On Radar Imaging of Current Features: Model and Comparison with Observations. Submitted to J. Geophys. Res.

Johannessen J.A., V.N. Kudryavtsev, D.B. Akimov, T. Eldevik, N. Winther, and B. Chapron. On radar imaging of current features. Part 2: Mesoscale eddy and current front detection. J. Geophys. Res., Vol. 110, C07017, doi:10.1029/2004JC002802, 2005

Mouche A., D. Hauser, and V. Kudryavtsev, Radar scattering of the ocean surface and sea-roughness properties: a combined analysis from dual-polarizations airborne radar

- observations and models in C-Band, J.Geoph.Res. Oceans, (submitted), 2005
- Kudryavtsev V., V.Dulov, V.Shrira, and V. Malinovsky, On Wind Driven Ocean Current, J. Phys. Oceanogr. (almost ready for submission), 2005
- Sandven S., V. Malinovsky, D.Akimov, and V.Kudryavtsev, Observations of natural and artificial surface slicks on the Black Sea by SAR. (in preparation)

Abstracts:

- Akimov D.B., B. Chapron, J.A. Johannessen V.N. Kudryavtsev. On Radar Imaging of Current Features: Model and Comparison with Observations. Proceedings of the 31st International Symposium on Remote Sensing of Environment, 20-24 June 2005, St. Petersburg, Russia (on CD)
- Johannessen J.A., B. Chapron, D.B. Akimov, N. Winther, T. Eldevik, V.N. Kudryavtsev. On Radar Imaging of Surface Current Features: Mesoscale Eddy and Current Front Detection. Proceedings of the 31st International Symposium on Remote Sensing of Environment, 20-24 June 2005, St. Petersburg, Russia (on CD)
- Kudryavtsev V.N. Marine oil spills control: SAR monitoring and model prediction. Proceedings of the 31st International Symposium on Remote Sensing of Environment, 20-24 June 2005, St. Petersburg, Russia (on CD)

NTsOMZ**Proceedings:**

- Люшвин П.В. Приближение спутниковых карт температуры поверхности воды (ТПВ) к картам ТПВ, построенным по данным контактных наблюдений. Вторая открытая Всероссийская конференция "Современные проблемы дистанционного зондирования Земли из космоса". Сборник научных статей. М.: ИКИ РАН. 2005. Том 2. С 140-144.

Abstracts:

- Феоктистов А.А., Новикова Н.Н., Пахомов Л.А., Люшвин П.В., Захаров А.И., Мартынов С.И., Федичев О.Б., Мирошин А.А. Разработка системы космического мониторинга нефтяных загрязнений морской поверхности. Третья всероссийская открытая конференция. «Современные проблемы дистанционного зондирования Земли из космоса». Москва, ИКИ РАН, 14-17 ноября 2005 г. Сборник тезисов конференции.
- Люшвин П.В., Кухарский А.В. Оценка состояния моря по AVHRR/NOAA. Разработка системы космического мониторинга нефтяных загрязнений морской поверхности. Третья всероссийская открытая конференция. «Современные проблемы дистанционного зондирования Земли из космоса». Москва, ИКИ РАН, 14-17 ноября 2005 г. Сборник тезисов конференции.
- Люшвин П.В., Полонский В.Ф., Коршенко А.Н., Лобов А.Л., Зырянов В.Н., Кухарский А.В., Егоров С.Н. Влияние регулирования стока Волги на гидрологию Северного Каспия. Третья всероссийская открытая конференция. «Современные проблемы дистанционного зондирования Земли из космоса». Москва, ИКИ РАН, 14-17 ноября 2005 г. Сборник тезисов конференции.
- P. Nikitin, S. Egorov, P.Lushvion. Use of Satellite Data in the Monitoring of the Caspian Sea Biota. 31st International Symposium on Remote Sensing of Environment. Proceedings. Saint Peterburg.

MHI**Papers**

- Malinovsky V.V., Dulov V.A., Bolshakov A.N. et al., (2004). Methodical and technical supplying of SIC-1M Real Aperture Radar calibration. "Ecological safety of coastal and shelf zones

and multiple use of shelf resources”, Sevastopol, MHI, v.11, 236 – 251. ISSN 1726-9903 (in Russian)

Malinovsky V.V. (2004). Possibility of wind mapping over the Black sea using SICH-1M Real Aperture Radar, “Ecological safety of coastal and shelf zones and multiple use of shelf resources”, Sevastopol, MHI, v.11, 226 – 235. ISSN 1726-9903, (in Russian)

Malinovsky V.V., Ivanov V.A. Sandven S.,Dulov V.A. (2005). Radar observations of contamination on the sea surface. “Ecological safety of coastal and shelf zones and multiple use of shelf resources”, Sevastopol, MHI, v.13, in press. ISSN 1726-9903, (in Russian)

Malinovsky V.V., Dulov V.A., Korinenko A.E., Bolshakov A.N., Smolov V.E. (2005). A field study of radar backscattering from the sea surface covered with oil film. “Using Technical Systems to Control Environment”, Sevastopol, MHI, in press, ISBN 966-02-3843-6, (in Russian)

Abstracts:

Ivanov V.A., Malinovsky V.V., Sandven S.,Dulov V.A. Radar observations of contamination in the Black Sea, State of art conditions of ecosystems in the Black Sea and Azov Sea, International conference, 2005, Donuzlav, Crimea

AARI

Papers:

Stanovoy, V., Lavrenov, I., Neelov, I., Sandven. S. Oil spill model system OilMARS (Oil spill Model for the Arctic Seas). (in preparation).

Abstracts:

Stanovoy, V., Neelov, I. (2005). Modeling of accidental oil spills in the region of the Northern Sea Route. Geophys. Res. Abs. Vol. 7, 02516. EGU General Assembly, Vienna, 25-29 April, 2005.

Lavrenov I.,Neelov I., Stanovoy V. Oil evolution model in the Arctic Seas. Booklet presentation for conference on remote sensing St.Petersburg, 2005

DOYu

Abstracts:

Agarkov, A.V., V.A. Doulov, A.E. Korinenko, V.V. Malinovskiy, S.A. Matvinenko, A.V. Meleshko. Radiolocation monitoring of pollutions of Black Sea surface. Preliminary results. 4.09.05.. 5th Ukrainian Conference on Space Exploration, 04 Sept. 2005.

Agarkov, A.V., L.A. Gouschin, S.A. Ermakov, E.V. Makarov, S.A. Matvinenko, I.A. Sergievskaya, Yu.B. Schegol'kov. Radiolocation sensing of films on sea surface.. 5th Ukrainian Conference on Space Exploration, 04 Sept. 2005.

Efimov, I.A., A.L. Makarov, S.A. Matvinenko, A.V. Meleshko, V.N. Tsimbal. Use of Sich-1M spacecraft SLR data in OSCSAR Project and promising Sich-3 spacecraft with SAR. 5th Ukrainian Conference on Space Exploration, 04 Sept. 2005.

Agarkov, A.V., I.V. Grigorash, S.A. Matvinenko, Yu.A. Selivanov. Measurements of Earth gravitational field using geophysical microsatellite. 2nd Open All-Russia Conference “Current problems of Earth remote sensing from outer space”, 16. November, 2004.

Agarkov, A.V., I.V. Grigorash, S.A. Matvinenko, A.V. Meleshko. Geophysical microsatellite. 4th Ukrainian conference on promising space exploration trends, 12.09.04.

Grigorash, and S.A. Matvinenko. Application of geophysical microsatellite for studies into seismic activity. VII International youth scientific and practical conference “Man and outer space”, 13.04.05.

Korotich, E.V. and S.A. Matvinenko. Processing of information from ERS spacecraft. VII International youth scientific and practical conference “Man and outer space”, 13.04.05.

Boutenko, E.V. and S.A. Matvinenko. Ground special complex of Sich-1M Space System. VII International youth scientific and practical conference "Man and outer space", 13.04.05.

Task 6: Networking and coordination with other GMES projects

The objective of this task was to establish a network of Russian, Ukrainian and western European service providers, users and agencies with the objective to build up operational monitoring and modeling services which includes Kara Sea, Black Sea, Caspian Sea and other regional seas of Europe. Since NERSC is central partner in several EU and ESA GMES project related to monitoring and forecasting of the marine environment (i.e. DISMAR, MARCOAST, MERSEA IP), the OSCSAR partners have been linked to these projects and results regarding oil spill monitoring have been reviewed. Within the OSCSAR team MHI and Yuzhnoye are working in close cooperation with the Ukrainian Space Agency and NTsOMZ is directly involved in the definition of the earth observation programmes of the Russian Space Agency. In this way there is no better exchange of information between different projects and space agencies within Europe. Both the Russian and Ukrainian Space agencies have now increased focus on developing radar remote sensing systems with better capability to detect oil spills. In spite of ENVISAT's successful delivery of large amounts of SAR data for oil spill detection, there is still significant development work to be completed before operational monitoring is established. A key component is to have better SAR coverage of the sea areas. This requires contribution from several space agencies and a data distribution policy for SAR data that allows full exploitation of the Spaceborne SAR data in monitoring of the marine environment.

During the ISPRS conference in St. Petersburg in June 2005, extensive discussions were done with other space and remote sensing institutions in Russia and Kazakhstan. Also SAR receiving stations in Russia and Kazakhstan were contacted and plans for future projects were defined. The next step will be to establish follow-up projects for OSCSAR.

Acknowledgement

The OSCSAR project has been supported by IAF/ESA under the BEAR programme. In addition, the field experiment in the Black Sea has been supported by the Ukrainian Space Agency. SAR data has been provided by ESA, both for archived ERS data and for new ENVISAT ASAR and MERIS images. NTsOMZ has provided various other satellite data to support the study of surface slicks. Finally, support has been given in form of advice and scientific ideas by B. Chapron, Ifremer.

References

- DaSilva J.C., S.A. Ermakov, I.S. Robinson, D.R.G. Jeans and S.V. Kijashko, Role of surface films in ERS SAR signatures of internal waves on the shelf. 1. Short-period internal waves. *Journal of Geophys. Research.*, vol. 103, C4, 8009-8031, 1998.
- Eldevik, T. and K. B. Dysthe, (2002), Spiral eddies. *J. Phys. Oceanogr.*, 32, 851-869.
- Ermakov, S.A., S.G. Salashin, and A.R.Panchenko, Film slicks on the sea surface and some mechanisms of their formation, *Dyn. Atmos. Oceans*, 16 (3-4), 279-304, 1992.
- Ermakov S.A., Kijashko S.V., and Konnov I.R., 1996 Determining the elasticity parameter of surfactant films from damping measurements of standing gravity-capillary waves. // *Izvestiya, Atmospheric and Oceanic Physics*.
- Gade M., W. Alpers, H. Huhnerfuss and P. Lange, (1998), Wave tank measurements of wave damping and radar cross sections in the presence of monomolecular surface films, *J. Geoph. Res.*, 103, C3
- Gade M., W. Alpers, H. Huhnerfuss, H. Masuko, and T. Kobayashi, (1998). Imaging of biogenic and anthropogenic ocean surface films by the multifrequency/multipolarization SIR-C/X-SAR, *J. Geoph.Res.* 103, C8
- Jenkins A., S. Jakobs, Wave damping by a thin layer of viscous fluid, *Phys. Fluids*, 9(5), 1256-1264, 1997.
- Johannessen J., V. Kudryavtsev, D.Akimov, T. Eldevik, N. Winther, and B. Chapron, (2005), On radar imaging of current features. Part 2: Mesoscale eddy and current front detection, *J.Geoph.Res.*, VOL. 110, C07017, doi:10.1029/2004JC002802
- Kudryavtsev, V., D. Hauser, G. Caudal, and B. Chapron, (2003), A semi-empirical model of the normalized radar cross-section of the sea surface. Part 1: The background model, *J. Geophys. Res.*, 108(C3), 8054, doi:10.1029/2001JC001003
- Kudryavtsev V. and J. Johannessen, (2004), Effect of wave breaking on short wind waves, *Geophys. Res. Letter*, Vol. 31, No.20, L20310 10.1029/2004GL020619
- Kudryavtsev V., D.Akimov, J.A.Johannessen, and B. Chapron, (2005), On radar imaging of current features. Part 1: Model and comparison with observations, *J.Geoph.Res.*, VOL. 110, C07016, doi:10.1029/2004JC002505, Levich, V. G. (1962), *Physiochemical Hydrodynamics*, Prentice-Hall, Englewood Cliff.
- Mouche A., D. Hauser, and V. Kudryavtsev, (2005), Radar scattering of the ocean surface and sea-roughness properties: a combined analysis from dual-polarizations airborne radar observations and models in C-Band, *J.Geoph.Res. Oceans*, (submitted)
- Plant, W. J. (1990), *Surface Waves and Fluxes*, Volume II □ *Remote Sensing*, chap. Bragg scattering of electromagnetic waves from the air/sea interface, pp. 41-108.
- Thompson, D. R. (1988), Calculation of radar backscatter modulations from internal waves, *J. Geophys. Res.*, 93(C10), 12,371-12,380.

Part B: Financial Report

Western countries

Team	Labour cost	Over-head	Travel & subs.	Consumables	Other costs	Total
NERSC	0	0	14000	0	0	14000
Ifremer	1500	0	0	0	0	1500
Total	1500	0	14000	0	0	15500

Russia and Ukraine

NIERSC

Team	Personnel	Month rate	Months	Labour cost	Over-head	Travel & subs.	Cons	Other	Total
NIERSC	V. Kudryavtsev	500	7	3500					
	D. Akimov	300	9	2700					
	L. Zabolotskikh	300	8	2400					
	V. Alexandrov	400	6	2400					
	Sum NIERSC			11000	2000	5500	500	1000	20000

Travels:

1st Progress meeting at NTsOMZ (Moscow) 16-17 February 2005, Bobylev L.P. Kudryavtsev V.N., Akimov D.B.
 Scientific visit to NERSC (Bergen) 29 March – 26 April 2005, Akimov D.B.
 EGU General Assembly 2005 (Vienna) 24-29 April 2005, Kudryavtsev V.N.
 Working visit to MHI (Sevastopol) 28 March - 4 April 2005, Kudryavtsev V.N.

AARI

Team	Personnel	Month rate	Months	Labour cost	Over-head	Travel & subs.	Cons	Other	Total
AARI	Igor Lavrenov	500	9	4500				400	4900
	Vladimir Stanovoy	400	7	2800		200			3000
	Ivan Neelov	400	7	2800					2800
	Nina Iakovleva	100	6	600					600
	Tamara Pasechnik	100	6	600					600
	Vladislav Alexeev	100	6	600					600
		Sum AARI		41	11900		200		400

MHI

Team	Personnel	Month rate	Months	Labor cost	Over head	Travel & subs	Cons	Other	Total
MHI	V. Malinovsky (Team leader)	400	6	2400					
	V. Dulov (senior scientist)	400	6	2400					
	A. Nikiforov (scientist)	150	6	900					
	R. Stanichnaya (scientist)	200	6	1200					
	T. Bayankina (scientist)	200	6	900					
		Sum MHI		30	7800	500	2200		

DOYu

Team	Personnel	Month rate	Months	Labor cost	Over head	Travel & subs	Cons	Other	Total
DOYu	Group manager A. Agarkov	500	7	3500					
	Engineer S. Matvinenko	300	6	1800					
	Technician E. Boutenko	200	6	1200					
	Technician A. Meleshko	200	6	1200					
	Technician L. Svorobina	200	6	1200					
	Technician N. Sheloud'ko	200	6	1200					
	Sum DOYu		37	10100	700	2200			13000

IAP

Team	Personnel	Month rate	nbre month	Labour cost	Over-head	Travel & subs.	Cons	Other	Total
IAP (RU)	S. Ermakov (team leader)	500	9	4500					
	I. Sergievskaya (scientist)	300	7	2100					
	A. Kokorina (scientist)	250	6	1500					
	L. Gushin (scientist)	200	7	1400					
	Sum IAP		29	9500				500	10000

NTsOMZ

Team	Personnel	Month rate	nbre month	Labour cost	Over-head	Travel & subs.	Cons	Other	Total
NTs OMZ	N. Novikova	350	6	2100					
	L. Pakhomov	300	8	2400					
	O. Fedichev	250	6	1500					
	S. Martynov	250	4	1000					
	Sum NTs OMZ			7000	1000	2000			10000